INFORMATION TO USERS

This manuscript has been reproduced from the microfilm master. UMI films the text directly from the original or copy submitted. Thus, some thesis and dissertation copies are in typewriter face, while others may be from any type of computer printer.

The quality of this reproduction is dependent upon the quality of the copy submitted. Broken or indistinct print, colored or poor quality illustrations and photographs, print bleedthrough, substandard margins, and improper alignment can adversely affect reproduction.

In the unlikely event that the author did not send UMI a complete manuscript and there are missing pages, these will be noted. Also, if unauthorized copyright material had to be removed, a note will indicate the deletion.

Oversize materials (e.g., maps, drawings, charts) are reproduced by sectioning the original, beginning at the upper left-hand corner and continuing from left to right in equal sections with small overlaps. Each original is also photographed in one exposure and is included in reduced form at the back of the book.

Photographs included in the original manuscript have been reproduced xerographically in this copy. Higher quality 6" x 9" black and white photographic prints are available for any photographs or illustrations appearing in this copy for an additional charge. Contact UMI directly to order.

UMI

A Bell & Howell Information Company
300 North Zeeb Road, Ann Arbor MI 48106-1346 USA
313/761-4700 800/521-0600

University of Alberta

Optimization of a Noninteractive Algorithm for *In-Vivo* NMR Spectral Analysis

by

Mark Astridge ©

A thesis submitted to the Faculty of Graduate Studies and Research in partial fulfillment of the requirements for the degree of Master of Science

Department of Biomedical Engineering

Edmonton, Alberta

Fall 1997

National Library of Canada
Bibliothèque nationale du Canada

Acquisitions and Bibliographic Services
Acquisitions et services bibliographiques

395 Wellington Street
Ottawa ON K1A 0N4
Canada

395, rue Wellington
Ottawa ON K1A 0N4
Canada

Your file Votre référence

Our file Notre référence

The author has granted a non-exclusive licence allowing the National Library of Canada to reproduce, loan, distribute or sell copies of this thesis in microform, paper or electronic formats.

L'auteur a accordé une licence non exclusive permettant à la Bibliothèque nationale du Canada de reproduire, prêter, distribuer ou vendre des copies de cette thèse sous la forme de microfiche/film, de reproduction sur papier ou sur format électronique.

The author retains ownership of the copyright in this thesis. Neither the thesis nor substantial extracts from it may be printed or otherwise reproduced without the author's permission.

L'auteur conserve la propriété du droit d'auteur qui protège cette thèse. Ni la thèse ni des extraits substantiels de celle-ci ne doivent être imprimés ou autrement reproduits sans son autorisation.

0-612-22566-6

Canada

University of Alberta

Library Release Form

Name of Author: Mark Astridge

Title of Thesis: Optimization of a Noninteractive Algorithm for *In-Vivo* NMR Spectral Analysis

Degree: Master of Science

Year This Degree Granted: 1997

Permission is hereby granted to the University of Alberta Library to reproduce single copies of this thesis and to lend or sell such copies for private, scholarly, or scientific research purposes only.

The author reserves all other publication and other rights in association with the copyright in the thesis, and except as hereinbefore provided, neither the thesis nor any substantial portion thereof may be printed or otherwise reproduced in any material form whatever without the author's prior written permission.

Mark Astridge
3019 33A Ave. S.E.
Calgary, AB
CANADA
T2B 0J9

Dated: SEPT 30 1997

University of Alberta

Faculty of Graduate Studies and Research

The undersigned certify that they have read, and recommend to the Faculty of Graduate Studies and Research for acceptance, a thesis entitled Optimization of a Noninteractive Algorithm for *In-Vivo* NMR Spectral Analysis submitted by Mark Astridge in partial fulfillment of the requirements for the degree of Master of Science.

Dr. R. E. Snyder

Dr. Z. J. Koles

Dr. D. G. Hughes

Dr. J. Lind

Date Approved: 30 Sept 1997

This thesis is dedicated to my parents and to all who love snow.

ABSTRACT

An algorithm is developed for the analysis of free induction decays generated by nuclear magnetic resonance (NMR) spectroscopy experiments that does not require user input. Procedures for the selection of optimal setup parameters necessary for time domain analysis using linear prediction with singular value decomposition (LPSVD) is developed empirically based upon simulation of a two-line spectrum. Also developed are procedures for the identification and rejection of noise related lines which can be returned by the LPSVD algorithm. The procedures are integrated into a single algorithm which requires no input from the user to analyze NMR spectra and whose output is used to seed a maximum likelihood estimation procedure that returns results having zero bias and variances equal to the Cramer-Rao bounds. Testing was performed on simulated two-line spectra, simulated six-line ^{31}P spectra, and ^{31}P data taken from human calf muscle.

Acknowledgements

I would like to thank Ion Buicliu for letting me muck up the department computers, all of my fellow graduate students and the department staff for their support, and Rick Snyder for everything, especially his seemingly limitless patience. A big thank you to all my friends in Edmonton (now spread around the world) who helped make my stay such an enjoyable experience.

Special mention goes to Bill Gates and the Microsoft team for the intense pain and suffering their products inflicted on me in the creation of this thesis. Long live UNIX.

Table of Contents

1.0 Introduction — *1*

2.0 Magnetic Resonance Spectroscopy — *8*

2.1 Basic Magnetic Resonance Spectroscopy — **8**
- 2.1.1 Spin of a Nucleus — 8
- 2.1.2 Behaviour in Static Magnetic and RF Fields — 9
- 2.1.3 Relaxation — 13
- 2.1.4 Chemical Shift — 17
  - 2.1.4.1 Chemical Shielding — 17
  - 2.1.4.2 J-Coupling — 19
  - 2.1.4.3 Paramagnetic Shift Agents — 20
- 2.1.5 Detection of the NMR Signal — 20

2.2 Theoretical Form of the FID — **22**

2.3 Time Domain Analysis of the FID — **23**
- 2.3.1 Nonlinear Maximum Likelihood Estimation (NMLE) — 23
- 2.3.2 Linear Prediction with Singular Value Decomposition — 24

3.0 Automation of the LPANAL Algorithm — *28*

3.1 Specification of the Number of Data Points (N) — **28**

3.2 Specification of the Model Order (L) — **30**

3.3 Specification of the Cutoff Value — **31**
- 3.3.1 Manual Regularization — 32
- 3.3.2 Discrete Regularization — 33
- 3.3.3 Continuous Regularization — 34

3.4 Identification of Spurious Noise Related Lines — **36**
- 3.4.1 Even/Odd Subsets — 36
- 3.4.2 Real/Imaginary Subsets — 39
- 3.4.3 Multiple Acquisitions — 39

4.0 Results and Discussion — *43*

4.1 Specification of Cutoff or Regularization — **47**
- 4.1.1 Failure Rate with Noise for Manual Regularization — 48
- 4.1.2 Failure Rate with Noise for Discrete Regularization — 52
- 4.1.3 Failure Rate with Noise for Continuous Regularization — 52

4.2 Specification of Model Order (L) — **56**
- 4.2.1 Accuracy and Precision with Model Order — 57
- 4.2.2 Failure Rate with L — 59

4.3 Specification of Number of Data Points (N) — **60**
- 4.3.1 Dependency of the Analysis Time on N — 60
- 4.3.2 Accuracy and Precision with N — 63
- 4.3.3 Failure Rate with N — 66
- 4.3.4 Failure Rate with Maximum Line Frequency, Amplitude, and Phase — 67
- 4.3.5 Failure Rate with Decay and Line Separation — 70
- 4.3.6 Accuracy and Precision with Decay and Line Separation — 73

4.4 Noise Line Identification — **78**

4.5 A Totally Automated Algorithm 90
4.6 Simulated Muscle Phosphorus Spectra 95
4.7 Actual Muscle Phosphorous Spectra 102
5.0 Conclusions *105*
Appendix A The Cramer-Rao Lower Bound *109*
References *111*

List of Tables

Table 3.1 Noise estimates calculated from a 1024 point simulated FID $A_1 = 200$, $\phi_1 = 0$, $\alpha_1 = 0.031$ $f_1 = -0.12$, $A_2 = 100$, $\phi_2 = 0$, $\alpha_2 = 0.062$, and $f_2 = -0.16$, using the two methods of section 3.3.3. _____ **35**

Table 4.1 The parameters of the reference spectrum used to generate the simulations in sections 4.1 through 4.5. _____ **46**

Table 4.2 The parameters of the reference FID used to generate the simulations in section 4.6. _____ **96**

Table 4.3 Line identification failure for each of the six lines contained in the simulations generated from table 4.2 at a noise level of $\sigma = 10$. _____ **98**

List of Figures

Figure 2.1 Net effect of both parallel and antiparallel spins on the total magnetic moment vector in the presence of a magnetic field $\vec{B}_0$. 11

Figure 2.2 Direction of the magnetic moment vector in a rotating frame after a pulse of correct magnitude and duration is applied to tip it by a) 90° and b) 180°. 13

Figure 2.3 Effect of longitudinal relaxation on the magnitude of the magnetic moment vector in the z direction after 90° and 180° pulses. 14

Figure 2.4 Dephasing of the transverse magnetization due to precessional frequency variations. 15

Figure 2.5 Transverse relaxation effect on the received signal. 16

Figure 2.6 Differences in the precessional frequencies of some phosphorous containing chemicals present in muscle showing the shift due to chemical shielding for the different molecules and the splitting of ATP due to J-coupling. 19

Figure 2.7 The quadrature signals observed after demodulation for the non-phase shifted channel (x) and the 90° phase shifted channel (y). 21

Figure 3.1 Plot of pole locations for ten realizations with $A_1 = 200$, $\phi_1 = 0$, $\alpha_1 = 0.1$ $f_1 = -0.12$, $A_2 = 100$, $\phi_2 = 0$, $\alpha_2 = 0.1$, and $f_2 = -0.16$, at three different noise levels with N = 50, L = 25, and a cutoff of 2. 31

Figure 3.2 Effect of noise on the magnitude of the singular values and the identification of the cutoff value with $A_1 = 200$, $\phi_1 = 0$, $\alpha_1 = 0.1$ $f_1 = -0.12$, $A_2 = 100$, $\phi_2 = 0$, $\alpha_2 = 0.1$, and $f_2 = -0.16$, at three different noise levels with N = 50, and L = 25. 33

Figure 3.3 Even-odd subset flowchart showing analysis results for each subset and the comparison test using the CR bound calculated from the full dataset results. 38

Figure 3.4 Real-imaginary subset flowchart showing analysis results for each subset and the comparison test using the CR bound calculated from the full dataset results. 40

Figure 3.5 Multiple acquisition subset flowchart showing analysis results for each subset and the comparison test using the CR bound calculated from the full acquisition results. 42

Figure 4.0.1a The real part of a simulated FID generated from the parameters of Table 4.1 for various noise levels. 46

Figure 4.0.1b The real part of the frequency domain spectrum generated from the FID's in Figure 4.0.1a. 47

Figure 4.1.1a The accuracy and precision of parameter A_1 as a function of the cutoff and the noise, analyzed using LPSVD only. 49

Figure 4.1.1b The accuracy and precision of parameter A_1 as a function of the cutoff and the noise, analyzed using LPSVD only. 49

Figure 4.1.1c The accuracy and precision of parameter A_1 as a function of the cutoff and the noise, analyzed using LPSVD only. 50

Figure 4.1.1d The failure rate as a function of the cutoff and noise, analyzed using LPSVD. 50

Figure 4.1.1e The failure rate as a function of the cutoff and noise, analyzed using LPSVD. 51

Figure 4.1.1f The failure rate as a function of the cutoff and noise, analyzed using LPSVD. 51

Figure 4.1.2 Failure rate as a function of the noise for discrete regularization for different dataset lengths (N 52

Figure 4.1.3 Failure rate as a function of the noise for continuous regularization for different dataset lengths (N). 53

Figure 4.1.4 Failure rate as a function of the noise comparing manual, discrete, and continuous regularization for a dataset length (N) of 50. 54

Figure 4.1.5a A histogram showing the total number of results containing the specified number of lines for manual regularization with a cutoff of 2. 54

Figure 4.1.5b A histogram showing the total number of results containing the specified number of lines for manual regularization with a cutoff of 10. 55

Figure 4.1.5c A histogram showing the total number of results containing the specified number of lines for manual regularization with a cutoff of 20. 55

Figure 4.1.5d A histogram showing the total number of results containing the specified number of lines for discrete regularization. 56

Figure 4.1.5e A histogram showing the total number of results containing the specified number of lines for continuous regularization. 56

Figure 4.2.1a The accuracy and precision of parameter A_1 as a function of the ratio L/N and the number of data points (N) analyzed using LPSVD only. 57

Figure 4.2.1b The accuracy and precision of parameter A_2 as a function of the ratio L/N and the number of data points (N) analyzed using LPSVD only. 58

Figure 4.2.1c The accuracy and precision of parameter f_1 as a function of the ratio L/N and the number of data points (N) analyzed using LPSVD only. 58

Figure 4.2.1d The accuracy and precision of parameter f_2 as a function of the ratio L/N and the number of data points (N) analyzed using LPSVD only. 59

Figure 4.2.2 Failure rate as a function of the relative model order (L/N) analyzed for two different dataset lengths (N) using LPSVD. 60

Figure 4.3.1a The mean analysis time required to process a two line spectrum using LPSVD with a cutoff of 2, LPSVD with continuous regularization (LPSVDCR), and NMLE, for noise levels of $\sigma = 5$ and 50. 62

Figure 4.3.1b The mean analysis time required to process a two line spectrum using LPSVD for different cutoffs, LPSVD with continuous regularization (LPSVDCR), and NMLE, for a noise level of $\sigma = 5$. 63

Figure 4.3.2a The accuracy and precision of parameter A_1 as a function of the number of data points (N) analyzed using LPSVD only for various noise levels. 64

Figure 4.3.2b The accuracy and precision of parameter A_2 as a function of the number of data points (N) analyzed using LPSVD only for various noise levels. 65

Figure 4.3.2c The accuracy and precision of parameter f_1 as a function of the number of data points (N) analyzed using LPSVD only for various noise levels. 65

Figure 4.3.2d The accuracy and precision of parameter f_2 as a function of the number of data points (N) analyzed using LPSVD only for various noise levels. 66

Figure 4.3.3 Failure rate as a function of the number of data points (N) analyzed for several different noise levels using LPSVD. 67

Figure 4.3.4a Failure rate of the LPSVD analysis procedure as a function of the number of data points (N) used and the highest line frequency for a two line spectrum. 68

Figure 4.3.4b Failure rate of the LPSVD analysis procedure as a function of the number of data points (N) used and the amplitude of the second line for a two line spectrum. 69

Figure 4.3.4c Failure rate of the LPSVD analysis procedure as a function of the number of data points (N) used and the phase of the second line for a two line spectrum. ____ 69

Figure 4.3.5a Failure rate of the LPSVD procedure as a function of the number of data points (N) for three different decay rates and a constant line separation $\Delta f = 0.04$. ____ 72

Figure 4.3.5b Failure rate of the LPSVD procedure as a function of the number of data points (N) for four different line separations and a constant line decay rate of $\alpha_1 = 0.075$. ____ 72

Figure 4.3.5c A comparison of the optimal values of N approximated through equation [3.1.1] (calc.) and by determination of the minimum failure rate through simulation (meas.) for various decay rates and line separations. ____ 73

Figure 4.3.6a The accuracy and precision of parameter A_1 as a function of the number of data points (N) and decay rate (α_1), analyzed using LPSVD only. ____ 74

Figure 4.3.6b The accuracy and precision of parameter A_2 as a function of the number of data points (N) and decay rate (α_1), analyzed using LPSVD only. ____ 74

Figure 4.3.6c The accuracy and precision of parameter f_1 as a function of the number of data points (N) and decay rate (α_1), analyzed using LPSVD only. ____ 75

Figure 4.3.6d The accuracy and precision of parameter f_2 as a function of the number of data points (N) and decay rate (α_1), analyzed using LPSVD only. ____ 75

Figure 4.3.6e The accuracy and precision of parameter A_1 as a function of the number of data points (N) and line separation (Δf), analyzed using LPSVD only. ____ 76

Figure 4.3.6f The accuracy and precision of parameter A_2 as a function of the number of data points (N) and line separation (Δf), analyzed using LPSVD only. ____ 76

Figure 4.3.6g The accuracy and precision of parameter f_1 as a function of the number of data points (N) and line separation (Δf), analyzed using LPSVD only. ____ 77

Figure 4.3.6h The accuracy and precision of parameter f_2 as a function of the number of data points (N) and line separation (Δf), analyzed using LPSVD only.. ____ 77

Figure 4.4.1a The cause of failure as a function of the noise for real/imaginary subsectioning for a dataset length (N) of 50. ____ 79

Figure 4.4.1b The cause of failure as a function of the noise for even/odd subsectioning for a dataset length (N) of 50. ____ 80

Figure 4.4.1c The cause of failure as a function of the noise for multiple acquisition subsectioning for a dataset length (N) of 50. 80

Figure 4.4.2a The cause of failure as a function of the noise for multiple acquisition subsectioning for a decay rate of $\alpha_2 = 0.10$ and a line separation of $\Delta f = 0.06$. 81

Figure 4.4.2b The cause of failure as a function of the noise before subsectioning for a decay rate of $\alpha_2 = 0.10$ and a line separation of $\Delta f = 0.06$. 82

Figure 4.4.2c The cause of failure as a function of the noise for multiple acquisition subsectioning for a decay rate of $\alpha_2 = 0.10$ and a line separation of $\Delta f = 0.03$. 82

Figure 4.4.2d The cause of failure as a function of the noise before subsectioning for a decay rate of $\alpha_2 = 0.10$ and a line separation of $\Delta f = 0.03$. 83

Figure 4.4.2e The cause of failure as a function of the noise for multiple acquisition subsectioning for a decay rate of $\alpha_2 = 0.05$ and a line separation of $\Delta f = 0.06$. 83

Figure 4.4.2f The cause of failure as a function of the noise before subsectioning for a decay rate of $\alpha_2 = 0.05$ and a line separation of $\Delta f = 0.06$. 84

Figure 4.4.2g The cause of failure as a function of the noise for multiple acquisition subsectioning for a decay rate of $\alpha_2 = 0.05$ and a line separation of $\Delta f = 0.03$. 84

Figure 4.4.2h The cause of failure as a function of the noise before subsectioning for a decay rate of $\alpha_2 = 0.05$ and a line separation of $\Delta f = 0.03$. 85

Figure 4.4.3a The cause of failure as a function of the noise for even/odd subsectioning for a decay rate of $\alpha_2 = 0.10$ and a line separation of $\Delta f = 0.06$. 86

Figure 4.4.3b The cause of failure as a function of the noise before subsectioning for a decay rate of $\alpha_2 = 0.10$ and a line separation of $\Delta f = 0.06$. 87

Figure 4.4.3c The cause of failure as a function of the noise for even/odd subsectioning for a decay rate of $\alpha_2 = 0.10$ and a line separation of $\Delta f = 0.03$. 87

Figure 4.4.3d The cause of failure as a function of the noise before subsectioning for a decay rate of $\alpha_2 = 0.10$ and a line separation of $\Delta f = 0.03$. 87

Figure 4.4.3e The cause of failure as a function of the noise for even/odd subsectioning for a decay rate of $\alpha_2 = 0.05$ and a line separation of $\Delta f = 0.06$. 88

Figure 4.4.3f The cause of failure as a function of the noise before subsectioning for a decay rate of $\alpha_2 = 0.05$ and a line separation of $\Delta f = 0.06$. 88

Figure 4.4.3g The cause of failure as a function of the noise for even/odd subsectioning for a decay rate of $\alpha_2 = 0.05$ and a line separation of $\Delta f = 0.03$. 89

Figure 4.4.3h The cause of failure as a function of the noise before subsectioning for a decay rate of $\alpha_2 = 0.05$ and a line separation of $\Delta f = 0.03$. 89

Figure 4.5.1a The cause of failure as a function of the noise for the totally automated algorithm for a decay rate of $\alpha_2 = 0.10$ and a line separation of $\Delta f = 0.06$. 92

Figure 4.5.1b The cause of failure as a function of the noise for normal LPSVD for a decay rate of $\alpha_2 = 0.10$ and a line separation of $\Delta f = 0.06$. 92

Figure 4.5.1c The cause of failure as a function of the noise for the totally automated algorithm for a decay rate of $\alpha_2 = 0.10$ and a line separation of $\Delta f = 0.03$. 93

Figure 4.5.1d The cause of failure as a function of the noise for normal LPSVD for a decay rate of $\alpha_2 = 0.10$ and a line separation of $\Delta f = 0.03$. 93

Figure 4.5.1e The cause of failure as a function of the noise for the totally automated algorithm for a decay rate of $\alpha_2 = 0.05$ and a line separation of $\Delta f = 0.06$. 94

Figure 4.5.1f The cause of failure as a function of the noise for normal LPSVD for a decay rate of $\alpha_2 = 0.05$ and a line separation of $\Delta f = 0.06$. 94

Figure 4.5.1g The cause of failure as a function of the noise for the totally automated algorithm for a decay rate of $\alpha_2 = 0.05$ and a line separation of $\Delta f = 0.03$. 95

Figure 4.5.1h The cause of failure as a function of the noise for normal LPSVD for a decay rate of $\alpha_2 = 0.05$ and a line separation of $\Delta f = 0.03$. 95

Figure 4.6.1 The frequency domain equivalent of the simulated FID generated from table 4.2 with noise levels of $\sigma = 5$ and 10 for a P_i/PCr ratio of 0.15. 97

Figure 4.6.2a The accuracy and precision of the amplitude of the ATP-β peak as a function of the P_i/PCr ratio analyzed using the totally automated algorithm of section 4.5. 99

Figure 4.6.2b The accuracy and precision of the amplitude of the ATP-α peak as a function of the P_i/PCr ratio analyzed using the totally automated algorithm of section 4.5. 99

Figure 4.6.2c The accuracy and precision of the amplitude of the ATP-γ peak as a function of the P_i/PCr ratio analyzed using the totally automated algorithm of section 4.5. 100

Figure 4.6.2d The accuracy and precision of the amplitude of the PCr peak as a function of the P_i/PCr ratio analyzed using the totally automated algorithm of section 4.5. ___ **100**

Figure 4.6.2e The accuracy and precision of the amplitude of the PDE peak as a function of the P_i/PCr ratio analyzed using the totally automated algorithm of section 4.5. ___ **101**

Figure 4.6.2f The accuracy and precision of the amplitude of the P_i peak as a function of the P_i/PCr ratio analyzed using the totally automated algorithm of section 4.5. _____ **101**

Figure 4.6.3 The accuracy and precision of the amplitude of the measured P_i/PCr ratio as a function of the true P_i/PCr ratio analyzed using the totally automated algorithm of section 4.5._____ **102**

Figure 4.7.1 An example of a real ^{31}P FID acquired from human calf muscle in the NMR experiment FI052795 and its frequency domain equivalent showing the major phosphorous lines._____ **103**

Figure 4.7.2 The P_i/PCr ratio calculated from the analysis of 93 acquisitions from the experiment FI052795 identifying the different regions of the experimental protocol, rest (RX), work (WX),and recovery (ZX) and the change over time of the ratio._____ **104**

Figure 4.7.3 The pH calculated from the analysis of 93 acquisitions from the experiment FI052795 identifying the different regions of the experimental protocol, rest (RX), work (WX), and recovery (ZX) and the change over time of the pH. _____ **104**

List of Symbols and Abbreviations

α_i	Normalized decay rate of the ith sinusoid in the time domain signal
α_{min}	Smallest decay rate in modelled signal
$\mathbf{a}$	Prediction vector for LPSVD
a_i	Relative amplitude of the signal from population i before sampling
A_i	Amplitude of the ith sinusoid in the time domain signal
AR	Autoregressive
ATP	Adenosine triphosphate
$\mathbf{b}$	Complex amplitude vector
$\bar{B}_0$	Static magnetic field vector
B_0	Static magnetic field magnitude
$\bar{B}_1$	Rotating magnetic field
B_1	Rotating magnetic field magnitude
$\bar{B}_{eff}$	Effective applied magnetic field
χ^2	Goodness of fit estimator
CR	Cramer Rao
δ_i	Frequency shift of nucleus population i
Δt	Time domain sampling interval
ΔE	Energy difference between states
Δf	Chemical shift
Δf_{min}	Smallest frequency difference
DFT	Discrete Fourier transformation
ε_i	Singular value
E_m	Energy of a nucleus at state m
f	Normalized frequency
FID	Free induction decay
γ	Gyromagnetic ratio of a nucleus
h	Planck's constant
$\mathbf{h}$	Solution vector in linear prediction
I	Spin value of a nucleus
k	Number of exponentially decaying sinusoids in the signal
k	Boltzmann's constant
K	Singular value cutoff value
λ	Singular value regularization parameter
L	Model order
LPSVD	Linear prediction with singular value decomposition
LPSVD(CR)	LPSVD using continuous regularization
μ	Magnitude of the magnetic moment of a nucleus
$\bar{\mu}$	Magnetic moment of a nucleus
$\bar{M}$	Total magnetic moment vector
MLE	Maximum likelihood estimation
MRS	Magnetic resonance spectroscopy

N	Number of datapoints sampled
N_m	Number of spins at state m
NMLE	Nonlinear maximum likelihood estimation
NMR	Nuclear magnetic resonance
ppm	Parts per million
ϕ_i	Phase angle of the ith sinusoid
P	Probability
PCr	Phosphocreatine
PDE	Phosphodiesters
P_i	Inorganic phosphates
RF	Radio frequency
σ	Standard deviation of the noise
σ	Linear shielding constant
σ^2	Variance
Σ	Diagonal matrix of singular values
Σ_R^{-1}	Inverse of the singular value matrix truncated or regularized
s	Received signal before sampling
s_i	Complex frequency
SNR	Signal to noise ratio
SVD	Singular value decomposition
T	Absolute temperature
T_1	Longitudinal relaxation time
T_2	Transverse relaxation time
T_2^*	Overall transverse relaxation time
$\mathbf{U}$	Column orthogonal matrix of eigenvectors of $\mathbf{XX}^H$
VOI	Volume of interest
$\mathbf{V}$	Column orthogonal matrix of eigenvectors of $\mathbf{X}^H\mathbf{X}$
ω_i	Normalized angular frequency of the ith sinusoid
ω_0	Larmour frequency of a nucleus
w	Noise in the signal
x	Modelled time domain signal
$\mathbf{x}$	Modelled time domain signal vector
$\mathbf{X}$	Linear prediction matrix
y	Estimate of the time domain signal
z_i	Roots of the linear prediction polynomial equation
$\mathbf{Z}$	Unity vectors of magnitude one for each root

1.0 Introduction

Magnetic resonance spectroscopy (MRS) is a powerful technique for the noninvasive analysis of the chemical composition and environment of tissues. Relative concentrations can easily be obtained of many biologically important molecules based on nuclei visible through MRS such as ^{1}H, ^{31}P, and ^{13}C. In some cases pH and even temperature can be measured. With this information the state of a metabolic process can be determined or diseases diagnosed.

In its simplest form a nuclear magnetic resonance (NMR) machine consists of a high field magnet which produces a constant, homogeneous, magnetic field in a region large enough to encompass the sample or volume of interest, a radio frequency antenna for irradiating and receiving signal from the sample, and electronics designed to demodulate the received signal and digitize it for analysis. Typically the frequency of irradiation is in the 10's to 100's of MHz. The received signal, called a free induction decay (FID), is ideally composed of a sum of k exponentially decaying sinusoids with differing amplitudes, phases, decay rates, and frequencies, each related to a metabolite or a particular chemical environment of a metabolite. After demodulation and sampling the signal may be modelled as:

$$x(n) = \sum_{i=1}^{k} A_i e^{(-\alpha_i + j\omega_i)n\Delta t + j\phi_i}, \quad 0 \le n \le N-1 \qquad [1.1]$$

where $x(n)$ is the nth sample of the signal, A_i is the amplitude of the ith sinusoid, α_i is the decay rate of the ith sinusoid, ω_i is the angular frequency of the ith sinusoid, ϕ_i is the phase of the ith sinusoid, Δt is the sampling interval, and N is the total number of samples acquired. Additionally, noise is present in the received signal and is generally assumed to

be white, having a zero-mean Gaussian distribution with no correlation between the real and imaginary parts. Normally, due to the low sensitivity of NMR, the experiment is repeated a number of times and averaged until an acceptable signal to noise ratio (SNR) is achieved.

Once acquired, the signal must be analyzed to retrieve the desired information, namely, the parameters which characterize each sinusoid. Ideally, the analysis technique should have several important characteristics. 1) It should identify all relevant spectral components (sinusoids) without falsely identifying noise related components. Due to the low SNR inherent in *in-vivo* signals this characteristic becomes difficult to achieve. 2) It should quantify the component parameters with zero bias and variances equal to their optimal values, the Cramer-Rao lower bounds of each parameter which are the minimum theoretical variances in the presence of zero mean, Gaussian distributed noise. 3) Repeated analysis should return exactly the same results, thus the technique should not require any judgment by the operator. 4) The technique should allow for prior knowledge of the results to be included in the analysis to allow for improvements in the precision. 5) The analysis execution time should not be prohibitively long based on the nature of the experiment and the desired confidence in the results.

Currently there are no techniques which have all of the above characteristics, each technique having corresponding strengths and weaknesses. Generally, the techniques fall into two categories: those that operate in the frequency domain and those that operate in the time domain (signal domain). Most current analytical procedures that operate in the frequency domain are based on discrete Fourier transformation (DFT). Traditionally, DFT is performed on the raw data after a noise reduction step, usually multiplication with a windowing function. Then, after phase correction to enhance visualization of the spectrum, Lorentzian lines are fitted to the modified spectrum. Except in the simplest of

cases this requires an experienced operator to setup and run the analysis. The quality of the results is dependent on the operator's expertise. Other frequency domain techniques use prior knowledge of each line in the spectrum to directly fit Lorentzian lines generated using prior knowledge (parameters A, ϕ, α, and ω, for each line). It should be noted that the definition of a Lorentzian line assumes an infinite data sequence which will lead to nonzero bias in the results. For a truncated sequence we must compute the Fourier transform of the truncated model function and then fit that to the Fourier transform of the data. All frequency domain procedures suffer when rapidly decaying metabolites appear in the signal, corrupting the first few data points in the time domain. A rapidly decaying metabolite will generate a broad baseline underneath the frequency domain spectrum. Frequency domain techniques generally rely on measuring the area under a Lorentzian line which will lead to a bias in the area measurement.

Time domain methods can be subdivided into those which are interactive and require initial guesses for the model parameters, and those which are noninteractive and generate their own estimates. The major techniques which require initial guesses are usually based on maximum likelihood estimation (MLE) [1, 2]. Using the initial guesses as a starting point, they attempt to minimize a "closeness of fit" estimator based on the difference between the FID regenerated from the model parameters and the original data by modifying the parameters. Obviously, this requires detailed prior knowledge about the signal. The major techniques which do not require initial guesses are based on autoregressive (AR) modelling, also known as backward linear prediction [5, 6, 7]. In backward linear prediction, each data point in the FID is defined to be a weighted sum of the following data points. The weighting coefficients can then be used to determine the frequency and decay parameters of the model function. The amplitude and phase parameters are then determined using a simple least squares procedure. Ideally, the number of exponentially decaying sinusoids in the signal is determined automatically and

the linear prediction procedure will require no input from the operator. There is, however, signal dependent information required by the procedure which affects the performance of the analysis.

A disadvantage of linear prediction methods, as opposed to maximum likelihood methods, is that the resulting parameter estimates are biased and have variances larger than the Cramer-Rao lower bounds, while maximum likelihood methods return results which have zero bias and variances equal to the Cramer-Rao lower bounds [3]. On the other hand, maximum likelihood methods have a need for good starting values to operate effectively. Clearly, a procedure which has the advantages of both linear prediction methods and maximum likelihood methods would be highly desirable for the analysis of NMR data.

A time domain processing procedure which does not require initial estimates for the model parameters and gives the optimal accuracy and precision in NMR spectroscopy was developed by Ho [3, 12]. The MLE procedure, which results in optimal bias and precision but requires initial estimates of the parameters, is preceded by linear prediction with singular value decomposition (LPSVD) which generates the estimates. The resulting algorithm has the advantages of optimal bias and precision, and removes the dependence on the operator's knowledge of the signal components. However, signal dependent parameters are still required by the procedure for proper analysis. Specifically, LPSVD requires preselection of the number of acquired data points to be used in the analysis (N), the model order (L), and a cutoff number for the SVD procedure [5, 6] needed to reduce the effect of noise on the estimates. Incorrect selection of these values can lead to either missing lines in the returned estimates or additional noise related lines. Once passed to the MLE algorithm these starting values may lead to nonoptimal bias and precision in the final results. Clearly, proper selection of N, L, and the cutoff number, plus reduction of

the number of noise related lines in the LPSVD generated estimates, is crucial to the success of the MLE procedure. Essentially, the quality of the MLE results is dependent on the quality of the starting values.

The main goal of this thesis is to improve the algorithm of Ho by automatically setting values for N, L, and the cutoff number, while not degrading the accuracy and precision of the results. Additionally, a reduction in the probability of missing lines or including extraneous lines in the results is desired. To achieve this goal, procedures for determining N, L, the cutoff number, and identifying extraneous lines were implemented and tested, the results of which will be presented here.

Linear prediction methods are sensitive to the number of data points used. Inclusion of data beyond an optimal N or truncation of the data before reaching an optimal N can lead to a larger error in the resulting parameters and an increased probability of missing lines or including noise lines. An estimate of the optimal number of data points to use for analysis can be obtained by determining the main exponential decay of the signal and the minimum frequency separation of the sinusoids in the signal.

Integral to linear prediction is the determination of the weighting coefficients in the AR model. The number of weighting coefficients used is defined as the model order. Under zero noise conditions the model order must be equal to the number of parameters to be solved for [7]. In the case of the FID there is one complex parameter per component to be solved for directly: the complex frequency. The real part is the decay rate and the imaginary is the angular frequency (amplitude and phase are determined from a least squares procedure). Thus, for a noiseless FID the model order is $L = k$, where k is the number of exponentially decaying components in the FID. Unfortunately, when the signal contains noise this equation no longer holds and the model order must be increased well

beyond k. Practically, L is set to be anywhere from 0.25N to 0.75N. Experimentally it has been shown that in this range the error in the parameter estimates from linear prediction is relatively insensitive to L [12]. Alternatively, a procedure called Final Prediction Error [13] can be used to determine the best model order for each data set and determine the model order which gives the minimum variance to the error between the original data and the modelled data.

Under the higher noise conditions which exist in most *in-vivo* NMR signals the linear prediction procedure may attempt to fit the noise with damped sinusoids as well. Two closely related procedures designed to reduce noise in the signal are based on modification of the singular values returned from the singular value decomposition of the linear prediction matrix. One of the procedures, called "discrete regularization", reduces noise by truncating the singular values at a threshold value [6]. All values below the threshold are discarded and the weighting coefficients are then found. The number of noise related damped sinusoids in the results is reduced substantially. A problem can occur if the threshold is incorrectly specified. If the threshold is too high, signal components will be missed; if the threshold is too low noise lines will be included. The threshold can be determined from a comparison between the singular values and the noise estimate of the FID and then used to set the truncation value. A method which ensures that the maximum amount of signal is retained with the minimum amount of noise, called "continuous regularization" [10], has the same effect on the results but has the advantage of a continuously variable threshold which can be easily determined from the signal.

Although selection of the number of data points N, model order L, and regularization threshold do much to reduce extraneous components in the results, noise related components may still appear. Unless the person doing the analysis is experienced and knows the components to be expected, these noise related components could be

interpreted as signal leading to incorrect conclusions. As well, noise components will affect the bias and variance of the overall results as these components are included in the maximum likelihood procedure. To identify the noise related components in the results an algorithm has been developed based on subsets of the original data. The FID is split into two different sets and each analyzed separately. The results are compared with the results from an analysis of the full FID. A component is identified as signal if it exists in all three sets of results and is within a predefined equivalence region of the full result in the subset results. Otherwise, it is considered to be noise and is removed from the final results. The equivalence region is specified by estimates of the parameter variances. This method of identifying noise related components is based on the idea that each subset of the data contains the same realization of the signal while having differing noise realizations. An analysis of each subset should give similar results for the signal components while the noise results will be random.

All methods of analysis in use today require some initial specification of analysis parameters and/or some operator intervention. Even though linear prediction requires no starting values for analysis, it does require several parameters to be specified to give the best results. The goal of this thesis is to determine and automate the selection of these parameters based on the data presented for analysis such that no user intervention and expertise is required.

2.0 Magnetic Resonance Spectroscopy

In this chapter we will use a simple classical description of NMR to describe the processes which are used to generate the NMR signal. Beginning with a description of the spin of a nucleus we will move though a discussion of its behaviour in both static and rotating magnetic fields. Next, the processes that allow meaningful NMR measurements to be made: relaxation, chemical shift and shielding, J-coupling, as well as paramagnetic shift agents, will be described. Finally, the system used for detecting the signal for processing is explained and background theory for a time domain method used as a basis in Chapter 3 for the analysis and quantitation of the signal is supplied.

All magnetic resonance phenomena are based on a property of nuclei called spin. Associated with the spin is a magnetic moment which, when the nuclei are in a static magnetic field, results in the nuclei existing in discrete energy states. Application of radio frequency (RF) energy at an appropriate frequency can induce transitions between these states. When the RF energy is removed the nuclei will return to equilibrium, losing energy to the surroundings at the same frequency as the initial stimulus. Measurement and quantitation of the energy released as the nuclei return to equilibrium allows information about their state to be determined.

2.1 Basic Magnetic Resonance Spectroscopy

2.1.1 Spin of a Nucleus

Spin is the property of atomic nuclei that allows magnetic resonance measurements to be made. The value of the spin depends upon the number of neutrons

and protons in the nucleus. Only those nuclei possessing an odd number of protons and/or an odd number of neutrons will be NMR visible. Directly related to the spin is the nuclear magnetic moment which can be modelled as a magnetic dipole with its axis along the axis of spin. Nuclei with a spin of $I \geq \frac{1}{2}$ will have a net angular momentum resulting in a net magnetic moment not equal to zero. The equation relating the spin and magnetic moment is

$$\mu = \frac{\gamma h I}{2\pi}, \qquad [2.1.1]$$

where μ = the magnetic moment of the nucleus, γ = the gyromagnetic ratio of the nucleus (different for every nuclear species), h = Planck's constant, and I = the spin value of the nucleus.

Common nuclei used in *in-vivo* NMR spectroscopy are ^{1}H, ^{13}C, and ^{31}P. All have a spin of I = 1/2. In this description of NMR, only the case where I = 1/2 will be considered.

2.1.2 Behaviour in Static Magnetic and RF Fields

Quantum mechanically, in a static magnetic field the magnetic moment of the nuclei can assume discrete orientations only with respect to the field. A nucleus with a spin of I = 1/2 will have two possible orientations, one parallel to the field and one anti-parallel. In a static field $\vec{B}_0$, these two orientations have energies equal to

$$E_m = -\vec{\mu} \cdot \vec{B}_0 = -\gamma m \frac{hB_0}{2\pi}, \qquad m = \tfrac{1}{2}, -\tfrac{1}{2} \qquad [2.1.2]$$

and the energy difference is proportional to the strength of the static field and is

$$\Delta E = E_{-\frac{1}{2}} - E_{\frac{1}{2}} = \gamma \frac{hB_0}{2\pi}. \qquad [2.1.3]$$

Describing the interaction of a magnetic moment with an applied magnetic field in a classical sense, the rate of change of the angular momentum ($h\bar{I} / 2\pi$) is related to the torque on a magnetic moment in the static field by

$$\frac{d}{dt}\left[\frac{h\bar{I}}{2\pi}\right]\bar{\mu} \times \bar{B}_0,$$

leading to

$$\frac{d\bar{\mu}}{dt} = \bar{\mu} \times \gamma\bar{B}_0. \qquad [2.1.4]$$

Equation 2.1.4 shows that in a static magnetic field a magnetic moment will precess about the field at an angular frequency of $\omega_0=\gamma B_0$, known as the Larmour frequency. Although nuclei exist in both states, there is a larger population of spins parallel to the field than antiparallel according to the distribution

$$\frac{N_{\frac{1}{2}}}{N_{-\frac{1}{2}}} = e^{\frac{\Delta E}{kT}}, \qquad [2.1.5]$$

where k is Boltzmann's constant and T is the absolute temperature. The net effect is a total magnetic moment vector, $\bar{M}$, in the direction of the applied static field

$$\bar{M} = \sum_i \bar{\mu}_i,$$

where $\bar{\mu}_i$ is the magnetic moment vector of each individual nucleus. Figure 2.1 shows the net effect of the individual magnetic moments on the total magnetic moment in the presence of a static magnetic field of strength B_0.

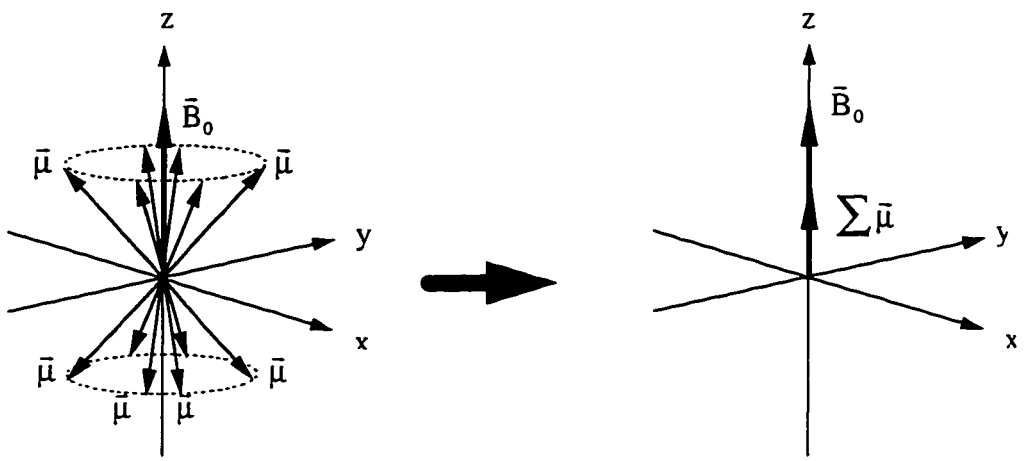

Figure 2.1
Net effect of both parallel and antiparallel spins on the total magnetic moment vector in the presence of a magnetic field $\bar{B}_0$.

Application of a rotating magnetic field to the system in the form of an RF field such that $\bar{B} = \bar{B}_0 + \bar{B}_1(t)$, where $\bar{B}_1(t) = (B_1 \cos(\omega t), B_1 \sin(\omega t), 0)$ and $\bar{B}_0 = (0,0,B_0)$, will influence the motion of the magnetic moments. The equations for each component of $\bar{M}$ are

$$\frac{dM_x}{dt} = \gamma(M_y B_0 - M_z B_1 \sin(\omega t)),$$

$$\frac{dM_y}{dt} = \gamma(M_z B_1 \cos(\omega t) - M_x B_0),$$

and $$\frac{dM_z}{dt} = \gamma(M_x B_1 \sin(\omega t) - M_y B_1 \cos(\omega t)). \qquad [2.1.6]$$

Defining a rotating frame of reference with the static field in the z direction and an $x_\rho y_\rho$ plane rotating at the frequency of the RF field, ω, such that both $\bar{B}_0$ and $\bar{B}_1(t)$ are static leads to the simplified equations of motion

$$\frac{dM_x}{dt} = (\gamma B_0 + \omega)M_y,$$

$$\frac{dM_y}{dt} = -(\gamma B_0 + \omega)M_x + \gamma B_1 M_z,$$

and $$\frac{dM_z}{dt} = -\gamma B_1 M_y, \qquad [2.1.7]$$

or combining into a single equation

$$\frac{d\bar{M}_\rho}{dt} = \gamma M \times \bar{B}_{eff},$$

where $\bar{B}_{eff} = (B_1, 0, \frac{\omega}{\gamma} + B_0)$. [2.1.8]

Equation [2.1.8] shows that when ω is negative ($B_1(t)$ rotates in a negative direction) and is equal to γB_0, $\bar{B}_{eff} = (B_1, 0, 0)$. $\bar{M}$ will then rotate in the zy_ρ plane at a frequency of $\omega_1 = \gamma B_1$. Various tip angles can be defined and are based on the time the RF field is applied and its magnitude. For example, a 90° pulse (y_ρ axis) requires the field to be applied for a time $t = \pi / 2\gamma B_1$ while a 180° pulse (-z axis) requires $t = \pi / \gamma B_1$. While these two angles are the most useful in terms of spectroscopy, other tip angles are also in use. Figure 2.2 shows the direction of the net magnetic moment vector $\bar{M}_0$ for the two cases described.

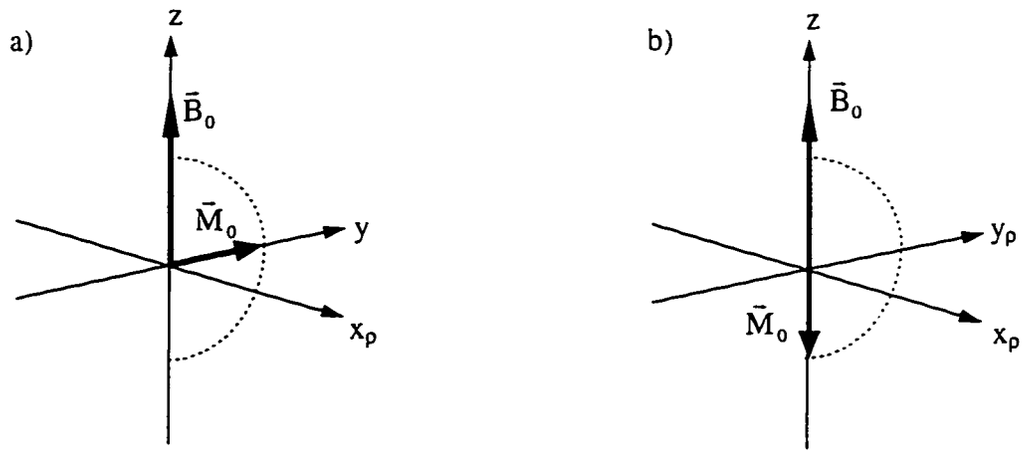

Figure 2.2
Direction of the magnetic moment vector in a rotating frame after a pulse of correct magnitude and duration is applied to tip it by a) 90° and b) 180°.

2.1.3 Relaxation

At the end of an RF pulse the population of spins in each state is perturbed from their thermal equilibrium values, and the component of $\vec{M}$ in the z direction, M_Z, can take on different values, i.e., for a 90° pulse $M_z = 0$, thus $N_{\frac{1}{2}} / N_{-\frac{1}{2}} = 1$, and for a 180° pulse $M_z = |M|$, thus, $N_{\frac{1}{2}} / N_{-\frac{1}{2}} = e^{-\frac{\Delta E}{kT}}$. When the RF field is removed and $\vec{B}_{eff} = (0,0,B_0)$, the recovery of M_Z towards its equilibrium value is governed by the first order rate equation

$$\frac{dM_z(t)}{dt} = \frac{1}{T_1}\left[M_0 - M_z(t)\right], \qquad [2.1.9]$$

where T_1 is called the longitudinal relaxation time. In longitudinal relaxation M_z returns to its thermal equilibrium value with a time constant of T_1. Thus, following a 90° pulse $M_z = M_0(1-e^{-t/T_1})$, and following a 180° pulse $M_z = M_0(1-2e^{-t/T_1})$, where M_z is

the net magnetization parallel to B_0 and M_0 is the net magnetization at thermal equilibrium.

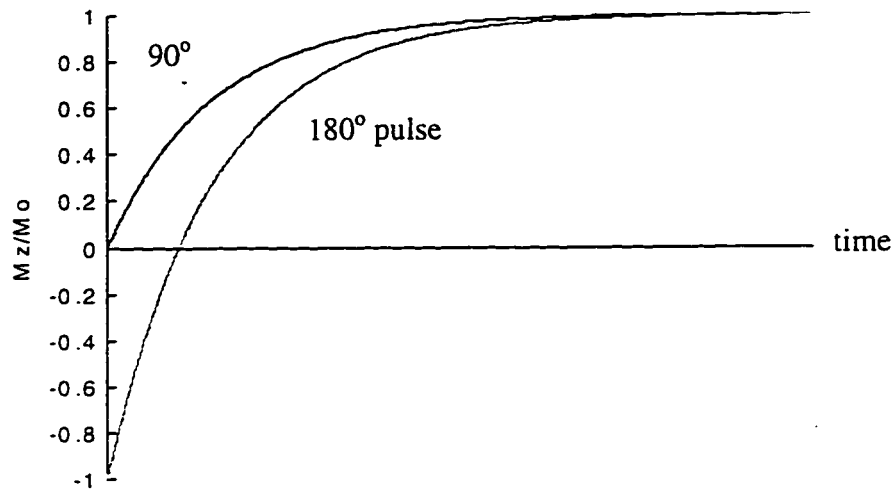

Figure 2.3
Effect of longitudinal relaxation on the magnitude of the magnetic moment vector in the z direction after 90° and 180° pulses.

In a perfect system where all the spins are identical and do not interact, $\vec{B}_0$ is perfectly homogeneous and the RF pulse is exactly at the Larmour frequency, the transverse magnetization will precess around the z axis until longitudinal relaxation overcomes the magnetization. However, in real systems the static magnetic field applied to a large number of spins is never uniform and is always affected by the fields generated by other dipoles and electron fields. Thus, the magnetic field, $\vec{B}_0$, experienced by each nucleus will be slightly different leading to different precessional frequencies. It should be noted that the magnetic field variations are time dependent due to random motion of the nuclei. After the RF field is removed there will be an irreversible dephasing of the transverse magnetic field, M_{xy}, governed by the rate equation

$$\frac{dM_{xy}}{dt} = \frac{-M_{xy}}{T_2} \qquad [2.1.10]$$

with the transverse relaxation decay time denoted by T_2.

A second cause of transverse relaxation is related to the inhomogeneity of $\bar{B}_0$ giving rise to non-time dependent variations in the magnetic field experienced by the nuclei, leading to additional dephasing of the transverse magnetization. Because the spins are now precessing at different rates, the result is a spreading of the transverse magnetization over time. Unlike the dephasing generated by neighbouring nuclei, this additional dephasing is reversible as can be demonstrated by first tipping the magnetization into the xy plane with a 90° pulse and then, after the magnetization has dephased, applying a 180° refocusing pulse which will reverse the transverse magnetization along the y_ρ axis in the rotating frame, causing the magnetization to rephase. Figure 2.4 shows a simplified example of the refocusing of a small number of spins.

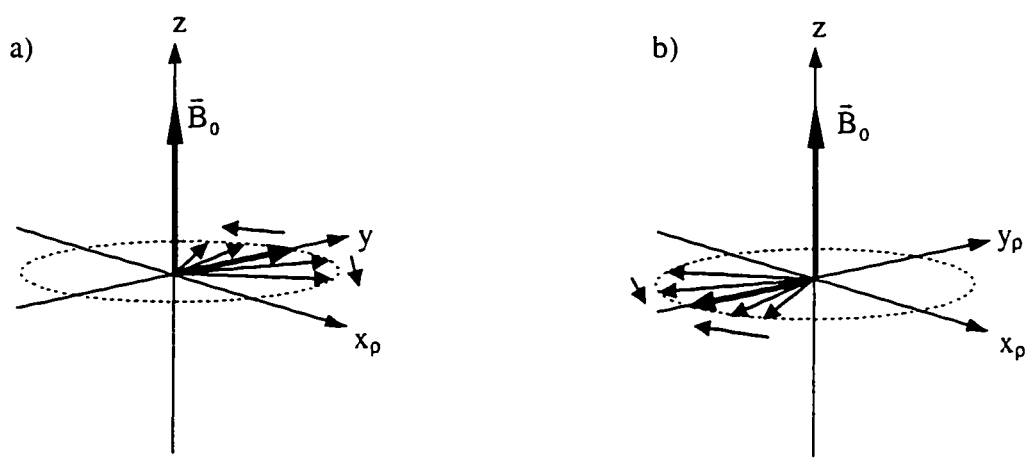

Figure 2.4
Dephasing of the transverse magnetization due to precessional frequency variations. a) initial dephasing. b) rephasing after refocussing pulse.

The overall effect of the two types of transverse relaxation is a shorter transverse decay time, denoted by T_2^*, and an exponential decay in the received FID which, for a

system with only a single line, is equivalent to the decay rate α. Solving equation [2.1.10] gives the envelope of the components of the transverse magnetization M_{xy}. Figure 2.5 shows how the two types of relaxation affect the received FID. For the irreversible transverse relaxation the envelope is

$$M_{xy}(t) = M_{xy}(0)e^{-t/T_2} \qquad [2.1.11]$$

and the overall transverse relaxation envelope is

$$M_{xy}(t) = M_{xy}(0)e^{-t/T_2^*}. \qquad [2.1.12]$$

Including the effects of relaxation in equation [2.1.4] gives the Bloch equation

$$\frac{d\vec{M}}{dt} = \gamma\vec{M} \times \vec{B} - \frac{(M_x\vec{i} + M_y\vec{j})}{T_2} + \frac{(M_z - M_0)}{T_1}\vec{k}, \qquad [2.1.13]$$

where $\vec{B} = \vec{B}_0 + \vec{B}_1(t)$ and $\vec{i}$, $\vec{j}$, and $\vec{k}$ are unit vectors along the x, y, and z axes.

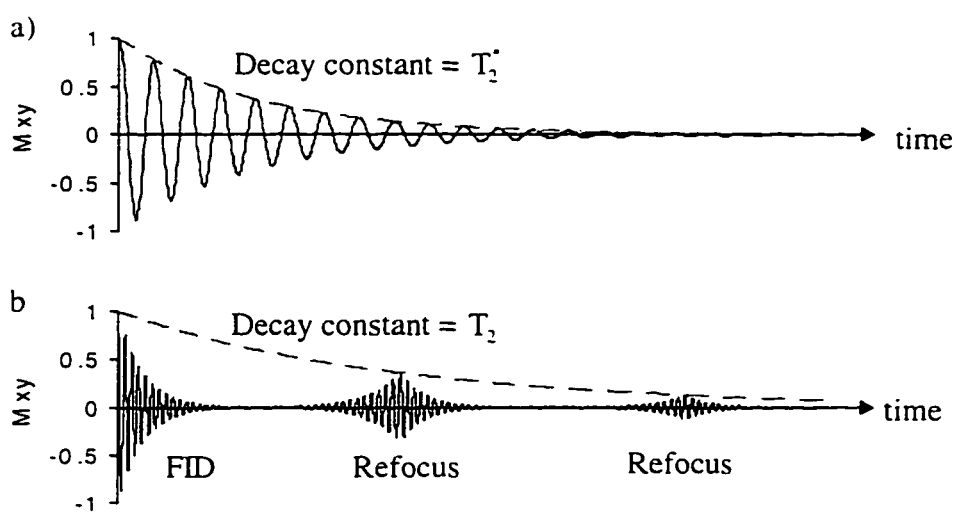

Figure 2.5
Transverse relaxation effect on the received signal. a) effect of T_2^* on a single FID, b) effect of T_2 on the magitude of refocussed magnetizations.

2.1.4 Chemical Shift

The resonance frequency of a nucleus is directly proportional to the magnetic field it experiences. In terms of molecules with more complex chemical structures the field experienced by the nuclei of interest will be modified by the field generated by the electrons. Thus, the same nucleus in different molecules or different chemical environments may have a slightly different resonant frequency. This frequency shift forms the basis of spectroscopy and gives information about the chemical composition and environment of the sample.

There are three major effects which contribute to chemical shift in biomedical processes: chemical shielding, J coupling, and paramagnetic shift agents.

2.1.4.1 Chemical Shielding

The magnetic field experienced by an individual nucleus can be modified by the electronic currents in the atomic orbitals which create an additional local magnetic field which is proportional to the main field $\vec{B}_0$. The resulting field is

$$\vec{B}_0 = \vec{B}_0(1-\sigma), \qquad [2.1.14]$$

where σ is known as the linear shielding constant. As chemical shift caused by shielding is dependent on B_0, it is reported in dimensionless units of parts per million (ppm):

$$\text{ppm} = \frac{\Delta f \cdot 10^6}{f_{ref}}, \qquad [2.1.15]$$

where f_{ref} is the reference frequency and Δf is the difference between the frequency of interest and the reference frequency.

Since σ is dependent on the electronic environment, the same nucleus in different environments can have different resonant frequencies. An important example is in muscle metabolism where ^{31}P is measured. The different environments for the phosphorous nucleus are phosphocreatine (PCr), phosphodiesters (PDE), inorganic phosphate (P_i = NaH_2PO_4), and the α, β, and γ phosphates of adenosine triphosphate (ATP). All have differing chemical shifts due to the different chemical structure of the molecules. Measuring the amplitudes of the resonances received allows the state of muscle to be determined. The resonant frequencies with example relative amplitudes are shown in figure 2.6.

Additionally, the pH of the sample affects the electronic environment of P_i, changing its measured chemical shift. A simple method of determining the pH of a sample is by measuring the frequency difference between the Pi and PCr resonances and using the equation

$$pH = 6.77 + \log\left[\frac{\Delta ppm - 3.29}{5.68 - \Delta ppm}\right], \qquad [2.1.16]$$

where Δppm is the frequency difference in ppm between the Pi and PCr resonances.

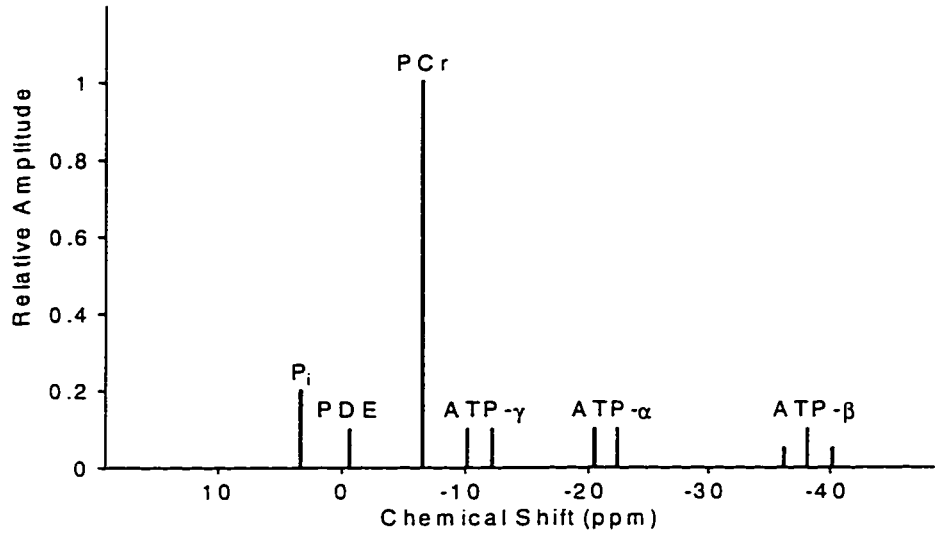

Figure 2.6

Differences in the precessional frequencies of some phosphorous containing chemicals present in muscle showing the shift due to chemical shielding for the different molecules and the splitting of ATP due to J-coupling. Amplitudes are for example only and change depending on the state of the muscle.

2.1.4.2 J-Coupling

J-coupling relies on the interaction between two nuclei possessing nonzero magnetic moments in the same molecule which communicate through the electron cloud. Information about the spin states of a nucleus is transmitted through the electronic bonds. The coupling constant J is independent of B_0 and has units of Hz.

An excellent example of J-coupling is seen in the α, β, and γ phosphates of ATP as illustrated in figure 2.6. The α and γ phosphates are split into doublets because they sense the two spin states of the β phosphate. They do not sense each others spin states as the coupling only extends over two or three bonds. The β phosphate is split into a triplet as it senses the states of both the α and γ phosphates (both parallel and antiparallel, and

the two combinations of antiparallel and parallel with double the probability of the other two).

2.1.4.3 Paramagnetic Shift Agents

The local magnetic field can be perturbed by neighbouring ions with unfilled shells, i.e., the 3d iron series or the 4f rare earth series. Nuclei of the paramagnetic ions are usually not observable themselves, but if they reside on the same molecule as the nucleus of interest they can modify its resonant frequency.

It should be noted that nuclei of slightly different resonant frequencies can be excited by a single RF pulse if the pulse is of the correct duration. A discontinuous RF signal can be designed to irradiate the sample over a range of frequencies due to its nonzero bandwidth.

2.1.5 Detection of the NMR Signal

At the moment the RF field is switched off after a 90° pulse we have transverse magnetization precessing about $\bar{B}_0$ at the resonance frequencies of the nuclei. A receiving coil placed with its axis in the transverse plane will have a voltage induced across it due to the changing magnetic field. The voltage is proportional to the magnitude of the transverse magnetization at the same precessional frequencies.

Electronically the signal is first amplified then demodulated with respect to two signals, one being the same as the RF pulse frequency, the other the RF pulse frequency phase shifted by 90°, to give a quadrature signal. Quadrature detection has the advantage of an improved SNR, a centred reference frequency, half the required bandwidth, and no

folding of the spectrum compared with a single detector. Figure 2.7 shows the signals received by the two channels for a single resonance when it is above and below the reference frequency to demonstrate how quadrature detection allows separation of positive and negative frequencies. A low pass filter then removes all high frequency components generated by the demodulation, leaving signals which are easily sampled by analog to digital converters. The sampling frequency of the converters must be higher than twice the highest frequency component in the signal (Nyquist theorem) or aliasing will result. Generally, the sampling frequency is made much higher than the Nyquist rate, with four times the cutoff frequency of the lowpass filter not being an unusual setting. Figure 2.7 shows the relationship between the quadrature components of the sampled signal for both positive and negative frequencies relative to the reference frequency.

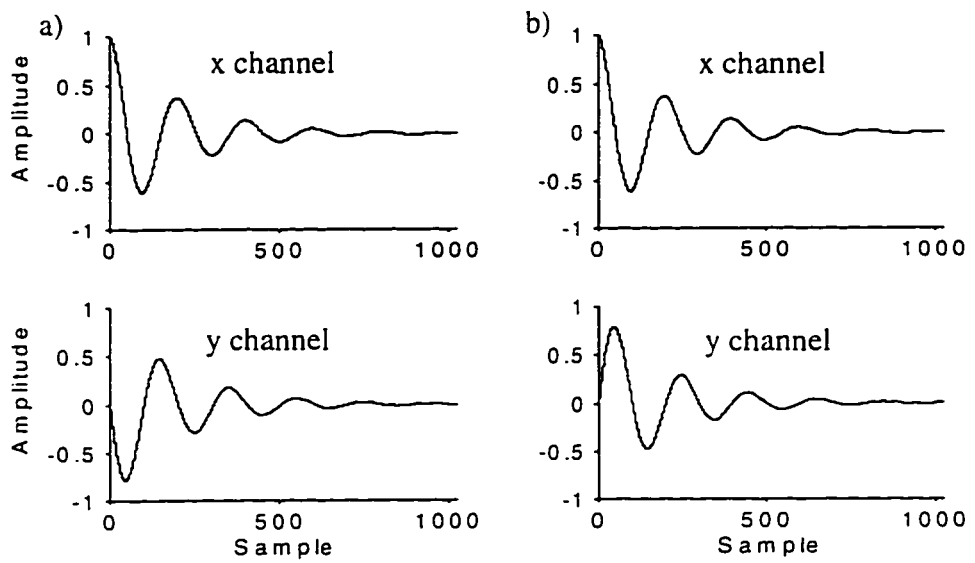

Figure 2.7

The quadrature signals observed after demodulation for the non-phase shifted channel (x) and the 90° phase shifted channel (y). a) signals when the frequency of the signal is below the reference (negative frequency), and b) above the reference (positive frequency).

2.2 Theoretical Form of the FID

Before demodulation and sampling the received NMR signal can be described as being proportional to the precessional magnetizations of the nuclei attenuated by the dephasing of the transverse magnetization:

$$s(t) = \sum_{i=1}^{k} a_i \cos[(\omega_0 + \delta_i)t]e^{-t/T_i} + w(t), \qquad [2.1.17]$$

where δ_i is the total frequency shift of the nuclei distributions corresponding to the ith population of molecules, T_i refers to the T_2^* decay constant of each population, a_i is the relative amplitude of the signal from each population, and w(t) is the noise present.

Quadrature detection multiplies the signal by both $\cos(\omega_0 t)$ and $-\sin(\omega_0 t)$ to give

$$\begin{aligned} x_0(t) &= \sum_i a_i \cos[(\omega_0 + \delta_i)t]\cos(\omega_0 t)e^{-t/T_i} + w(t) \\ &= \sum_i a_i \tfrac{1}{2}[\cos(\delta_i t) + \cos(2\omega_0 t)\cos(\delta_i t) - \sin(2\omega_0 t)\sin(\delta_i t)]e^{-t/T_i} + w(t), \\ x_{90}(t) &= \sum_i a_i \cos[(\omega_0 + \delta_i)t]\sin(\omega_0 t)e^{-t/T_i} + w(t) \\ &= \sum_i a_i \tfrac{1}{2}[\sin(\delta_i t) - \cos(2\omega_0 t)\sin(\delta_i t) - \sin(2\omega_0 t)\cos(\delta_i t)]e^{-t/T_i} + w(t). \end{aligned}$$

Using low pass filtering to remove the high frequency terms and amplification leads to

$$x(t) = \sum_i A_i e^{j\phi_i} e^{j\delta_i t} e^{-t/T_i} + w(t), \qquad [2.1.18]$$

where $x(t) = x_0(t) + jx_{90}(t)$ and A_i is a_i after amplification. The sampled version is

$$x(n\Delta T) = \sum_i A_i e^{j\phi_i} e^{j\Delta\delta_i n\Delta T} e^{-\frac{n\Delta T}{T_i}} + w(n\Delta T), \qquad [2.1.19]$$

where $t = n\Delta T$. Normalized to the sampling interval,

$$x(n) \equiv x(n\Delta T) = \sum_i A_i e^{(-\alpha_i + j\omega_i)n + j\phi_i} + w(n), \qquad [2.1.20]$$

where $\omega_i = \delta_i \Delta T$ and $\alpha_i = \Delta T / T_i$.

Noise in the received signal can come from innumerable sources including background RF, regions of the sample outside the volume of interest (VOI), thermal noise from the VOI, the receiver electronics, etc. Generally, the noise is assumed to be random, white, and Gaussian distributed. A simple analysis of the noise from experiments with and without samples has confirmed this.

2.3 Time Domain Analysis of the FID

2.3.1 Nonlinear Maximum Likelihood Estimation (NMLE)

Given a function which is an estimate of the FID, $y(n) = f(n; A_1, \phi_1, \alpha_1, \omega_1, \ldots A_k, \phi_k, \alpha_k, \omega_k)$, we want to find the best parameter set which allows the function $y(n)$ to fit the measured data according to a closeness of fit estimator. It is assumed that each data point has a measurement error that is independent of the parameters A_i, ϕ_i, α_i, and ω_i, is random with a Gaussian distribution around its true value, and that the variance ($\sigma^2(n)$) of each distribution is known for each point. The probability (P) of the dataset occurring within a fixed range Δy for each point is then the product of the probabilities at each point.

$$P = \prod_{n=1}^{N} e^{-\frac{1}{2}\left(\frac{x(n)-y(n)}{\sigma(n)}\right)^2} \Delta y, \qquad [2.3.1]$$

where x(n) is the measured value of data point n and y(n) is the model function value at the corresponding n. Maximizing [2.3.1] is equivalent to minimizing its negative logarithm which is

$$-\ln(P) = \sum_{n=1}^{N} \frac{[x(n) - y(n)]^2}{2\sigma^2(n)} - N \log \Delta y . \qquad [2.3.2]$$

Since N and Δy are constant, and $\sigma(n)$ is assumed to be constant for all n, the maximum likelihood estimate can be calculated from

$$\chi^2 = \frac{1}{\sigma^2} \sum_{n=1}^{N} \left(x(n) - y(n)\right)^2 , \qquad [2.3.3]$$

and we can use χ^2 for a goodness of fit estimator.

Using an iterative approach for minimization of a non-linear function, for example, the Levenberg-Marquardt method [22], will minimize equations [2.3.2] and [2.3.3] and give estimates for the parameters A_i, ϕ_i, α_i, and ω_i with the largest probability P for the given dataset. However, due to the possibility of the minimizing procedure finding a local minima, good starting values for the iterative algorithm are required. Such values can be determined using the automatic algorithm described in this thesis which is based upon LPSVD.

2.3.2 Linear Prediction with Singular Value Decomposition

Linear prediction with singular value decomposition (LPSVD) involves fitting the model to the data using a linear least-squares procedure based on singular value decomposition (SVD). The method is a derivative of Prony's method [23] for exponentially decaying signals.

Prony's method determines the parameters of exponential signals contained in noiseless signal samples. For a sampled data sequence assumed to consist of k complex damped exponential signals,

$$x(n) = \sum_{i=1}^{k} A_i e^{s_i n}, \qquad n = 0,1....,N-1 \qquad [2.3.5]$$

we wish to determine the complex unknowns A_i and s_i from the N samples. Since there are 2k complex unknowns, at least 2k samples are needed to determine them. The difficulty stems from the fact that the A_i's and s_i's enter bilinearly in equation [2.3.5]. Prony observed that the terms could be decoupled and then determined by solving two sets of linear simultaneous equations and one polynomial root extraction.

Unfortunately, when the signal is corrupted by noise, Prony's method will break down and the resulting linear equations will have no solution. In this case a least-squares approach is necessary. Since more than 2k samples are generally available, we can overdetermine the simultaneous equations and, using a least squares algorithm, generate estimates for the parameters A_i and s_i. It has been found, however, that the performance of a least-squares Prony's method is poor, even at high SNR's. To improve this Kumaresan and Tufts [6] proposed a noniterative method based on singular value decomposition (SVD) which filters the noisy data and significantly improves the estimates of A_i and s_i. The algorithm proceeds as follows. Using backward linear prediction (AR modelling) each data point in the FID can be expressed as a linear combination of the L (L is known as the model order) following data points:

$$
\begin{aligned}
-x_0^* &= a_1 x_1^* + a_2 x_2^* + \ldots a_L x_L^* \\
-x_1^* &= a_1 x_2^* + a_2 x_3^* + \ldots a_L x_{L+1}^* \\
-x_2^* &= a_1 x_3^* + a_3 x_4^* + \ldots a_L x_{L+2}^* \\
&\vdots \\
-x_{N-L-1}^* &= a_1 x_{N-L}^* + a_2 x_{N-L+1}^* + \ldots a_L x_{N-1}^*,
\end{aligned}
$$

where L<N-1. In matrix form

$$\mathbf{h} = \mathbf{X}\mathbf{a}, \qquad [2.3.6]$$

where $\mathbf{h} = -\begin{bmatrix} x_0^* \\ x_1^* \\ \vdots \\ x_{N-L-1}^* \end{bmatrix}$, $\mathbf{X} = \begin{bmatrix} x_1^* & x_2^* & \cdots & x_L^* \\ x_2^* & x_3^* & \cdots & x_{L+1}^* \\ & \vdots & & \\ x_{N-L}^* & x_{N-L+1}^* & \cdots & x_{N-1}^* \end{bmatrix}$, $\mathbf{a} = \begin{bmatrix} a_1 \\ a_2 \\ \vdots \\ a_L \end{bmatrix}$.

The prediction vector **a** is solved for using a linear least-squares procedure based on SVD. **X** is first decomposed using SVD into $\mathbf{X} = \mathbf{U}\Sigma\mathbf{V}^H$, where **U** is the column orthogonal matrix of eigenvectors of $\mathbf{X}\mathbf{X}^H$, **V** is the column orthogonal matrix of eigenvectors of $\mathbf{X}^H\mathbf{X}$, Σ is the diagonal matrix of singular values, and H stands for complex conjugate transposition. Then, the polynomial coefficient vector **a** is obtained using the regularized inverse equation

$$\mathbf{a} = \mathbf{V}\Sigma_R^{-1}\mathbf{U}^H\mathbf{h}, \qquad [2.3.7]$$

where Σ_R^{-1} is the inverse of the singular value matrix either truncated or regularized as a noise reduction step (see sec. 3.3).

Vector **a** is used to form the polynomial equation

$$0 = 1 + \sum_{i=1}^{\min(L,N-L)} a_i z^{-i}, \qquad [2.3.8]$$

whose k roots, when reflected inside the unit circle ($|z_i| \le 1$), are used as estimates for the zeros $z_i = e^{-\alpha_i + j\omega_i}$. Roots outside the unit circle are assumed to be noise and discarded. Given the estimates for α_i and ω_i, estimates for A_i and ϕ_i can be obtained through a linear least squares solution to

$$\mathbf{Zb} = \mathbf{x}, \qquad [2.3.9]$$

where $Z_{nm} = e^{(-\alpha_m + j\omega_m)n}$, $0 \le n \le N-1$, $1 \le m \le k$,

$$\mathbf{b} = \begin{bmatrix} A_1 e^{j\phi_1} \\ A_2 e^{j\phi_2} \\ \vdots \\ A_k e^{j\phi_k} \end{bmatrix}, \text{ and } \mathbf{x} = \begin{bmatrix} x_1 \\ x_2 \\ \vdots \\ x_N \end{bmatrix}.$$

The resulting parameters from the equation $y(n) = \sum_{i=1}^{k} A_i e^{j\phi_i} e^{(-\alpha_i + j\omega_i)n}, 0 \le n \le N-1$, can be used as starting values for the NMLE algorithm or further processed as in sec 3.4.

3.0 Automation of the LPANAL Algorithm

While the LPSVD algorithm is used to give initial estimates of the line parameters to the NMLE procedure, setup information still exists which must be supplied to the LPSVD procedure before the estimates are generated. The quality of the estimates is dependent upon the choice of three parameters; the number of data points analyzed (N), the model order (L) which, along with N, sets the rank of the linear prediction (LP) matrix, and the cutoff (K) or regularization (λ) value used to improve the condition of the LP matrix through SVD. Here we describe the effect of each parameter and possible methods for determining suitable values for them.

3.1 Specification of the Number of Data Points (N)

Generally, the acquisition of an FID is terminated when the signal is assumed to have decayed to a small fraction of its original magnitude ($5T_2^*$ for example) and only noise is being acquired. Depending on the choice of sampling rate chosen based on the expected spectral width of the signal, this can lead to a large sample size, with 1024 to 2048 samples not being unusual. As the LPSVD algorithm has a process order of N^3, analysis of the entire data set becomes time consuming. In conflict with the time constraint is the increase in precision of the results with increasing N. It has been shown in [3], however, that the gain in accuracy and precision with increases in N becomes negligible once a threshold value has been reached.

It can be shown (see section 4.1.5) using a Monte Carlo simulation that the LPSVD algorithm has an optimal sample size for a specific signal where the probability of identifying all signal components is highest. Increasing N past this point may lead to higher accuracy and precision in the parameter estimates if the threshold described above

has not been reached, but leads to a decrease in the probability of identifying all the components to be supplied to the NMLE algorithm. In recent papers by Diop et al. [16, 17] it has been suggested that the optimal sample size to fit the data in the least-squared sense using their enhancement procedure (EP) based LPSVD procedure is

$$N \equiv \frac{3T_2^*}{T_s},$$

where T_S is the sampling interval and T_2^* the largest relaxation time. Converting to normalized components and including the sign of the decay constant α we have

$$N \equiv \frac{3}{\alpha_{min}}.$$

Using this sample size with the EPLPSVD procedure gives an optimal fit equivalent to that of the NMLE algorithm for the same N in a single step. Not addressed, however, is its effect on the probability of missing a true line in the results (the failure rate) when using the procedure. We propose that the optimum data length for the LPSVD procedure for the lowest failure rate is dependent on signal decay and also on the smallest line separation in the signal. To produce the optimal fits of EPLPSVD, the NMLE procedure is applied to the results of the LPSVD procedure using as many data points as needed for the accuracy and precision desired. From experiment we have determined that for a simple two-line case the optimum data length for the LPSVD procedure can be approximated from the equation

$$N \equiv \frac{1}{2}\left[\frac{2}{\Delta f_{min}} + \frac{3}{\alpha_{min}}\right], \qquad [3.1.1]$$

where Δf_{min} is the minimum normalized frequency separation expected between the lines and α_{min} is the smallest normalized decay constant (longest decay) of the lines.

As the actual frequencies and decay constants of the signal components are not available until analysis is completed, and as this information is desired before analysis to set N, a priori knowledge of the signal based on spectral width, knowledge of the component frequencies and decays must be used to determine the optimal N. Assuming that equation [3.1.1] holds for a multi-line case, a priori knowledge of component frequencies and decay constants will give the minimum component separation (Δf_{min}) and minimum decay (α_{min}). Ideally, an iterative procedure which determines these two parameters directly from the signal can be applied.

3.2 Specification of the Model Order (L)

The model order sets the rank of the linear prediction matrix (with N) and determines the order of the polynomial whose roots are the signal poles. Under zero noise conditions the minimum model order which will lead to the correct number and location of the roots is k, where k is the number of exponentially decaying components in the signal. With increasing noise the model order must be increased to improve the estimates of the root locations and reduce the effect of extraneous roots. An example of the effect noise has on the root locations for a constant model order is shown in figure 3.1. With the increased noise in figure 3.1b the variation in the root locations begins to be visible. With even higher noise levels as in figure 3.1c some of the roots are calculated incorrectly. The model order is routinely set to be between 1/4 and 3/4 N [6]. Model order determining algorithms such as the Akike Information Criterion [13], designed to give the lowest order necessary to achieve a desired residual between the signal and its reconstruction leading to the lowest order polynomial possible, are not applicable in this situation. The goal is to find the polynomial with the true roots in the best positions [6]; extraneous roots can be identified and removed later (see section 3.4).

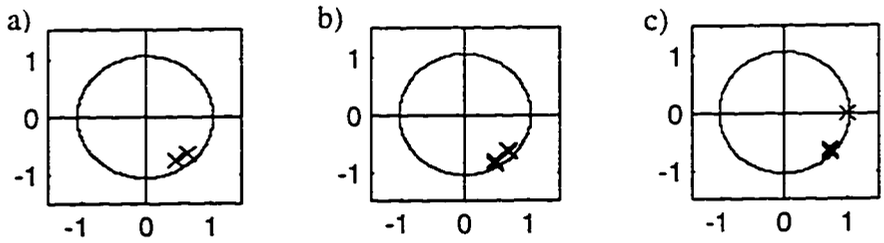

Figure 3.1

Plot of pole locations for ten realizations with $A_1 = 200$, $\phi_1 = 0$, $\alpha_1 = 0.1$ $f_1 = -0.12$, $A_2 = 100$, $\phi_2 = 0$, $\alpha_2 = 0.1$, and $f_2 = -0.16$, at three different noise levels with N = 50, L = 25, and a cutoff of 2. a) $\sigma = 0$, b) $\sigma = 30$, and c) $\sigma = 60$.

The dimensions of the LP matrix are formed from the model order L and the number of data points N and has a rank of min(L, N-L) which leads to a polynomial of the same length and a maximum number of roots of min(L, N-L). The maximum length of the polynomial occurs when L=N/2 and gives the minimum error in the positions of the calculated roots [6]. For short data sequences the number of identifiable roots must be maximized to prevent a loss of true roots. To maximize the number of roots found the size of the polynomial must therefore be maximized [9]. For L in the range $1/3N < L < 3/4N$ it has been shown [12] that the bias and variance are insensitive to model order. Proper selection of the model order will allow better starting values to be passed to the NMLE procedure which will then generate results with zero bias and optimal precision.

3.3 Specification of the Cutoff Value

One of the advantages of using SVD to solve the linear prediction equations is that it allows the application of a cutoff or regularization value to reduce the effect of noise on the results. In a noiseless signal the number of nonzero singular values is equal to the number of decaying exponentials in the signal. For low noise all singular values are nonzero, but the distinction between those belonging to "true" signal and noise is clear by

magnitude. Referring to figure 3.2, with higher noise no clear distinction can be made between the two as the noise blurs all singular values, leaving no singular vectors containing only noise or only signal. Even having a priori knowledge of the number of components in the FID does not automatically give the best cutoff value. To ensure that most of the signal is contained in the singular values kept the cutoff value must be higher than the number of known components, but must be low enough to keep a minimum amount of noise.

Three methods of defining cutoff will be discussed here: manual, discrete, and continuous regularization.

3.3.1 Manual Regularization

This is the original method of noise reduction proposed by Kumaresan and Tufts [6]. After performing singular value decomposition, perusal of the resulting singular values for the steepest descent gives an indication of which singular values correspond to singular vectors containing mostly signal and those containing mostly noise. The point of where there is an abrupt change in the slope of a plot of the singular values is called the cutoff value (K). When solving for the linear prediction coefficients using pseudo-inversion, the inverses of the singular values, $1/\varepsilon_i$, after the cutoff value are set to zero to reduce their ill conditioning effects and effectively reduce the noise. In higher noise conditions the difference between signal and noise related singular values is blurred and choosing a cutoff is difficult or even impossible for a signal with an unknown number of decaying exponentials in it. This is demonstrated in figure 3.2 where a two component signal with and without noise is analyzed and the singular values plotted. Clearly the noise causes difficulty in the selection of the cutoff value. Thus, an algorithm to

determine the best cutoff without user interaction is desirable. Sections 3.3.2 and 3.3.3 propose two possible methods of determining cutoff.

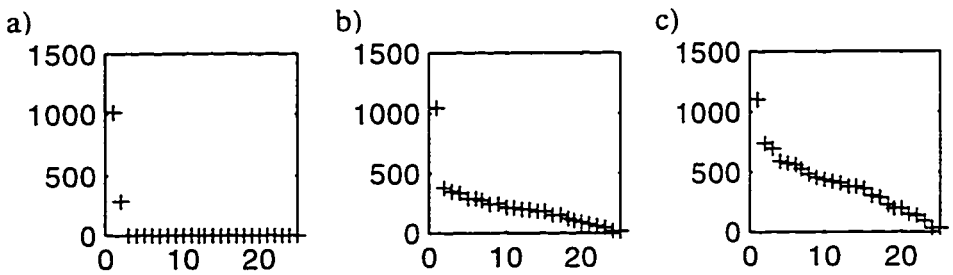

Figure 3.2

Effect of noise on the magnitude of the singular values and the identification of the cutoff value with $A_1 = 200$, $\phi_1 = 0$, $\alpha_1 = 0.1$ $f_1 = -0.12$, $A_2 = 100$, $\phi_2 = 0$, $\alpha_2 = 0.1$, and $f_2 = -0.16$, at three different noise levels with $N = 50$, and $L = 25$. a) $\sigma = 0$, b) $\sigma = 30$, and c) $\sigma = 60$.

3.3.2 Discrete Regularization

Discrete regularization was developed specifically for this thesis as an alternative to manual regularization. Instead of visually or arbitrarily selecting a cutoff value, an algorithm iteratively selects it by regenerating the FID using the truncated singular value matrix and subtracting it from the original FID. Iteratively the cutoff value is selected when the variance of the residual is smaller than or equal to the estimated variance of the noise (see section 3.3.3). The final truncated solution is then used to generate the linear prediction polynomial.

A shortcoming of manual and discrete regularization can by seen by looking at figure 3.2. Even after selection of a cutoff number and truncating the singular value

matrix, the "true" singular values are still corrupted by noise. Comparing the value of the first two singular values between figures 3.2a, 3.2b, and 3.2c clearly shows the noise increasing the magnitude of the first two "true" singular values. Continuous regularization alleviates much of this by adjusting all singular values to account for the effect of noise.

3.3.3 Continuous Regularization

Continuous regularization [10] differs from both manual and discrete regularization in that instead of setting $1/\varepsilon_i$ below the cutoff value to zero, a continuously variable regularization parameter (λ) is used to modify all singulars values, i.e.,

$$[\Sigma_R^{-1}]_{ii} = \frac{\varepsilon_i}{\varepsilon_i^2 + \lambda}, \; 1 \le i \le \min(L, N-L). \qquad [3.1.2]$$

Increasing λ is comparable to successive truncation of the singular values in manual and discrete regularization. When $\lambda = 0$ the method is equivalent to the original Prony method with no cutoff. λ is iteratively found by determining where the variance of the residual between the reconstruction and the original signal equals the noise variance.

Since continuous regularization is not limited to discrete levels of the regularization parameter, finer control over the signal fit is available. Generally, continuous regularization leads to inclusion of most of the signal plus some of the noise. Spurious noise related lines are usually generated which need to be identified and removed (see section 3.4). It has been found that continuous regularization performs better than discrete regularization in terms of missed lines [10]. Discrete regularization tends to miss true lines with amplitudes comparable to the noise due to the noise corruption of all singular values.

One of the requirements of both automatic techniques is determination of the noise variance of the signal. Two possible methods are:

1) Taking the tail of the acquired FID and calculating the noise variance from this portion. The assumption here is that the FID has decayed to a point where only noise is being acquired.

2) Analyzing the signal using a large cutoff value and LPSVD, then regenerating the sequence from the parameter estimates. This noise free regeneration is subtracted from the original to obtain a resulting signal which is assumed to contain only the noise plus a very small residual signal components due to the parameter errors. The noise variance can be calculated directly from the result.

It has been found through simulation that both methods estimate the noise level accurately. Table 3.1 shows the noise estimates calculated using both methods on a two line spectrum. Here we will use method 2 to automatically calculate the noise variance for regularization as it does not require knowledge of the characteristics of the original FID.

Actual Noise	0	5	10	20	30	40	50
Method 1	0.0000	5.0369	10.0442	19.7231	29.8652	40.0302	50.1890
Method 2	0.9490	4.9987	9.9917	19.9560	30.1103	40.7021	50.2482

Table 3.1

Noise estimates calculated from a 1024 point simulated FID $A_1 = 200$, $\phi_1 = 0$, $\alpha_1 = 0.031$ $f_1 = -0.12$, $A_2 = 100$, $\phi_2 = 0$, $\alpha_2 = 0.062$, and $f_2 = -0.16$, using the two methods of section 3.3.3. Ten noise realizations were generated for each noise level. Method 1 estimated the noise level from points 512 to 1024 of the FID. Method 2 calculated a noiseless FID using LPSVD with N = 128, L = 64, and a cutoff value of 32 and subtracted this from the original.

3.4 Identification of Spurious Noise Related Lines

When using LPSVD to generate parameter estimates, spurious noise related lines may appear in the results due to attempts to guarantee inclusion of all significant signal lines. Regularization, while reducing the effect of noise on the results, generally still leads to a larger number of lines in the results than there are true lines [15]. Since it is difficult in most cases to prevent noise related lines from being generated by LPSVD without missing true lines, a method of identifying noise lines based on their characteristics needs to be developed. A general method of identifying noise related lines relies on the assumption that between subsets of the data analyzed in a similar manner the parameters found for signal related peaks will be relatively stationary while those of the noise will vary. A simple test for equivalence between the parameter estimates for each subset using estimates of the parameter errors allows identification of equivalent lines in the subsets.

Three methods of subsectioning the FID will be discussed here: even/odd, real/imaginary, and multiple acquisitions.

3.4.1 Even/Odd Subsets

A single FID is separated into its even and odd numbered data points. The intermediate points of each set are then interpolated, thus maintaining the resulting decay rates and frequencies of the original set for the subsequent analysis.

Interpolation is achieved by mirroring each data subset around the y-axis, then applying discrete Fourier transformation (DFT) based interpolation. The interpolation of the even data points for the odd subset and the odd data points for the even subset occurs by padding the even or odd subsets with zeros between the actual data points. A DFT is

performed to convert to the frequency domain and the spectral image is set to zero. An inverse DFT is performed to convert the signal back to the time domain where the padded values now are smooth interpolations of the surrounding data points. Mirroring gives a better estimate for the first few interpolated points of the subsets as the DFT assumes a repeating sequence.

LPSVD is performed using best estimates for the number of data points (section 3.1), the model order (section 3.2), and using continuous regularization (section 3.3.3) on the original FID, the interpolated even subset, and the interpolated odd subset. Using the results from the original FID and an estimate of the noise found using an appropriate method, parameter errors are generated using a multiple of the Cramer-Rao bounds and the results of each analysis are compared. True lines are identified as those existing within the error estimates for the three parameters A, α, and ω in all three sets of results.

A side effect of subsectioning the FID into even and odd data sets is that the spectral width of the signal is cut in half. If signal exists outside of the range $-0.25<f<0.25$ (normalized frequency), aliasing will occur. It is possible to use the aliased signals to test for equivalence outside the region of $-0.25<f<0.25$ by folding the full dataset results into the region of $-0.25<f<0.25$, but complications will arise when the folded spectral frequencies overlap and cannot be separated. A second side effect is that due to the interpolation of the first point of the even subset, errors in phase are generated in the results. Consequently, the first data point of all subsets is dropped and phase is not used in the test of line equivalence. Figure 3.3 illustrates the even/odd subsectioning algorithm.

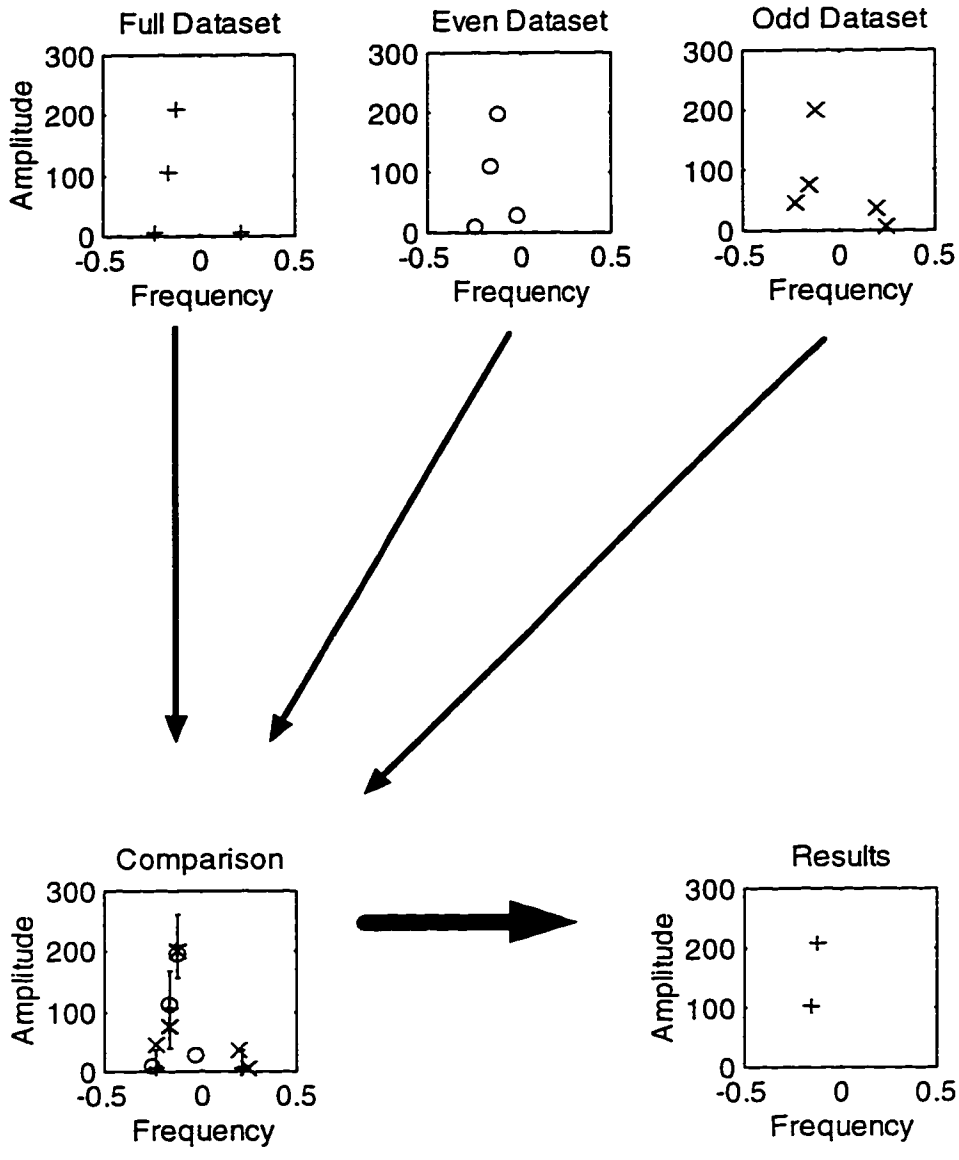

Figure 3.3

Even-odd subset flowchart showing analysis results for each subset and the comparison test using the CR bound calculated from the full dataset results. Not shown in the comparison is the test of decay rate equivalence.

3.4.2 Real/Imaginary Subsets

A single complex valued FID is separated into its real and imaginary components. LPSVD is performed on three different data sets, the original, the real only set, and the

imaginary only set. As in the even/odd analysis a parameter error estimate is generated from the results of the original data set and the results of all three compared to find the true lines with the exception that the amplitude parameter is not used in the equivalence test as the amplitudes in both domains can be different.

A side effect of the subsectioning using only the real or imaginary portions of the signal is that all sign information for the frequency of each component is lost. All lines in the results will be mirrored on both sides of $f = 0$. As well, in cases where two lines exist at the same absolute frequency but having reversed signs the lines will not exist in either the real part or the imaginary part of the FID and thus will not be identified. Figure 3.4 illustrates the real/imaginary subsectioning algorithm.

3.4.3 Multiple Acquisitions

Normally when acquiring spectroscopic data an average of many acquisitions from the same sample volume is made to generate an FID with the desired SNR. Since all acquisitions will have a different noise realization they can be separated into many groups, an average of all even numbered acquisitions, an average of all odd numbered acquisitions, and an average of all acquisitions or other combinations such as the first half of the acquisitions and the last half of the acquisitions. However, due to the possibility of the sample changing over the period of the experiment, even/odd acquisition separation is probably the best as changes in the sample will be reflected equally in all groupings.

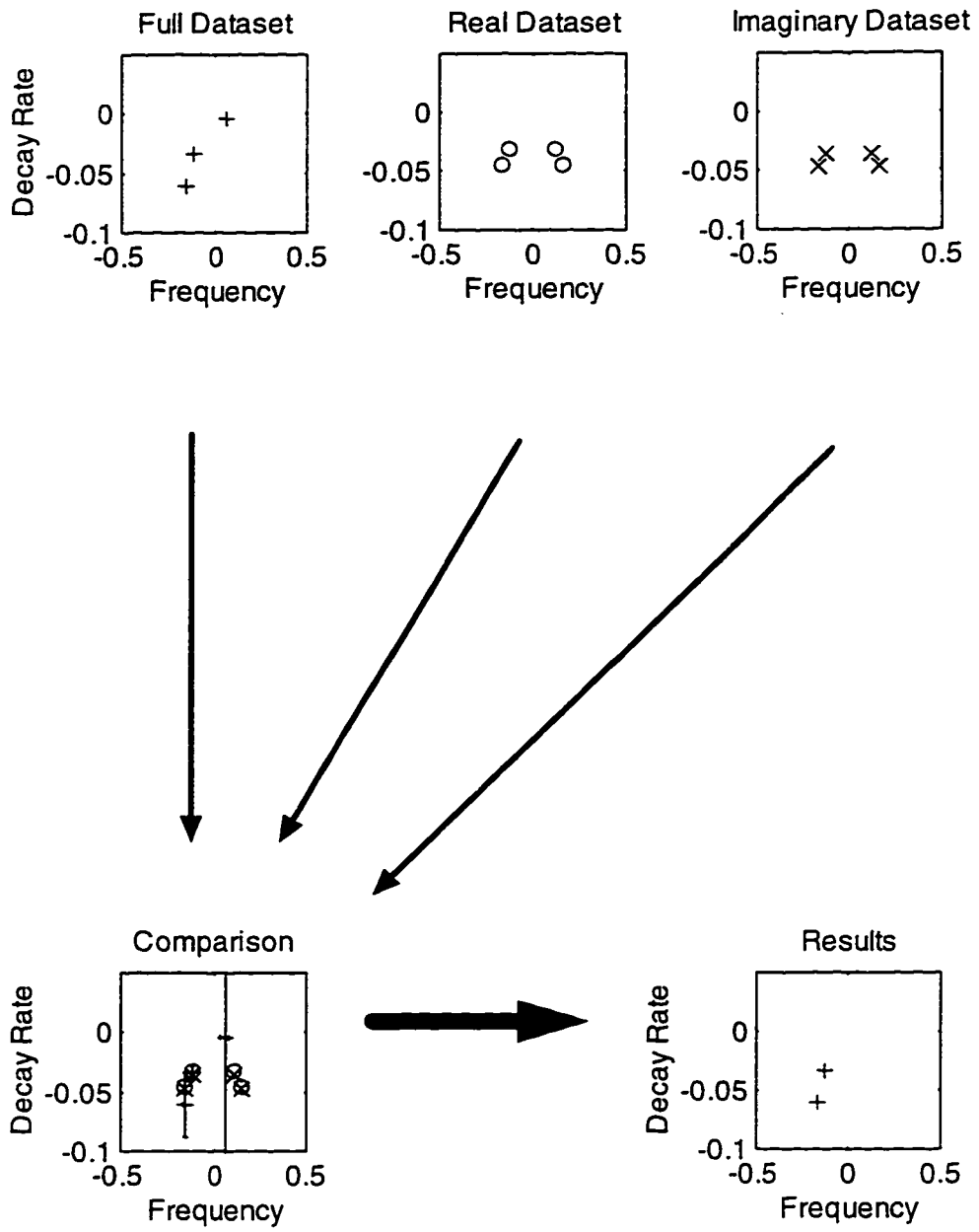

Figure 3.4
Real-imaginary subset flowchart showing analysis results for each subset and the comparison test using the CR bound calculated from the full dataset results. Illustrated in this example is the large error calculated for the decay rates.

Again, similar to even/odd and real/imaginary subsets, the results of LPSVD analysis of the three sets are compared using a parameter error estimate generated from the parameters of the complete average.

Unlike even/odd and real/imaginary subsectioning, there are no problems with aliasing and reduction of bandwidth. A $\frac{1}{\sqrt{2}}$ reduction in the SNR of the even and odd acquisition data sets will occur. Changes in the sample over the period of the acquisition averaging will be reflected in all data sets equally due to the interleaving of the averaging. Figure 3.5 illustrates the acquisition subset algorithm.

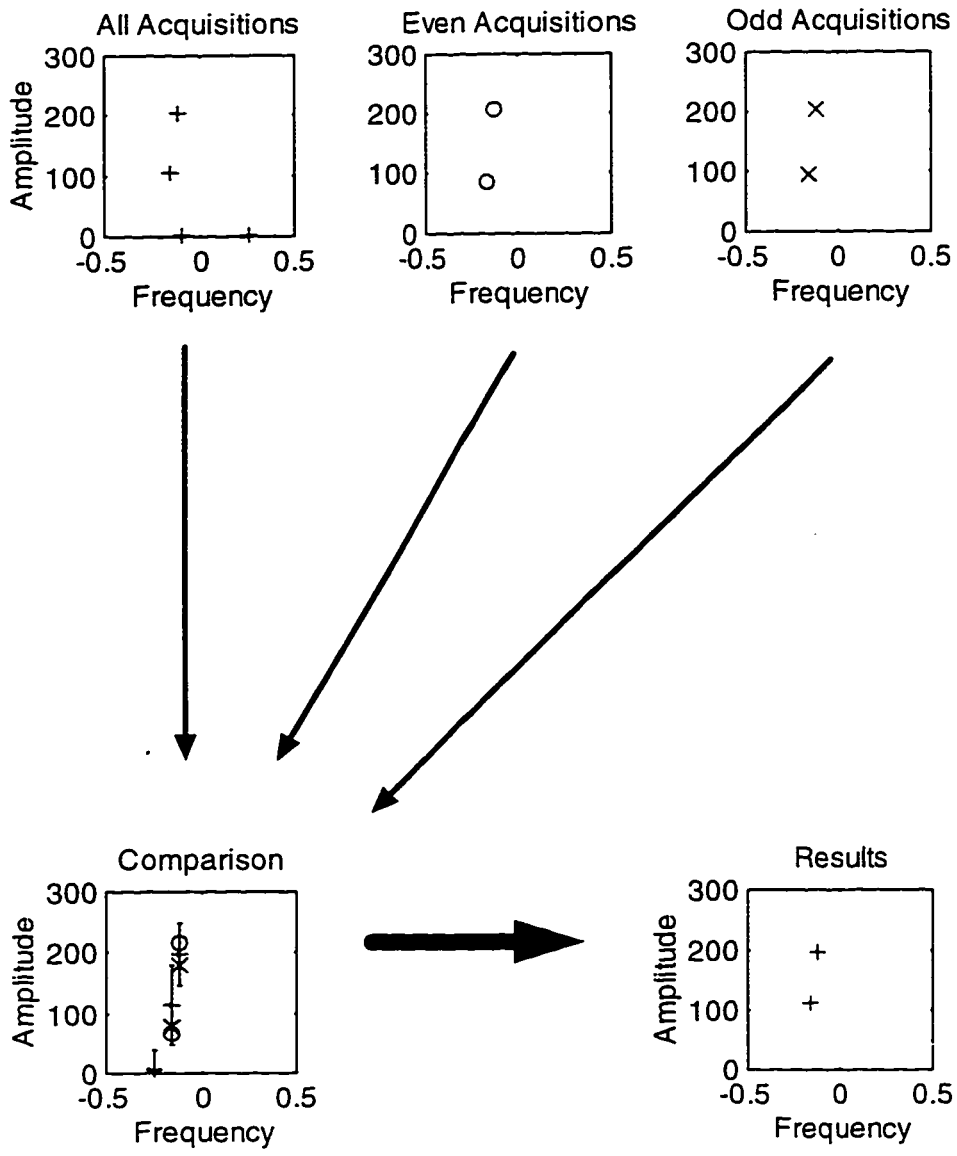

Figure 3.5

Multiple acquisition subset flowchart showing analysis results for each subset and the comparison test using the CR bound calculated from the full acquisition results. Not shown in the comparison is the test of decay rate equivalence.

4.0 Results and Discussion

In this chapter we show the effect of each input parameter (cutoff/regularization, L, N) on the performance of the analysis. Performance criteria for the effect of each parameter are the failure rate of the analysis procedure, the accuracy and precision of the results, and, for the parameter N only, analysis time to show its independence on noise and dependence on N. Having a low failure rate of the LPSVD procedure is necessary to pass the proper starting values to the NMLE procedure as it will only fit as many lines as are passed to it. Although the final accuracy and precision of the analysis results are determined by the NMLE procedure which is performed after LPSVD, having small errors in the intermediate results passed to the NMLE procedure is still important for its optimal performance. For this reason the effect of the input parameters on the accuracy and precision of the LPSVD results is discussed rather than those of the final NMLE procedure. We will also introduce procedures for determining optimal values for the input parameters and a noise line identification algorithm which will then be integrated to generate a totally automated procedure for analysis.

In section 4.1 we will contrast three methods of selecting the cutoff/regularization parameter in terms of failure rate and accuracy and precision. Two of the methods, discrete regularization and continuous regularization, are totally automated procedures. The third, manual regularization, is the original noise reduction technique proposed by Kumaresan and Tufts [5] and is included as a baseline for

comparison. We will show that the method of choice is continuous regularization as proposed for use in NMR by Kölbel and Schäfer [10].

In this section and in sections 4.2, 4.3, and 4.6 a failure is defined to be the absence of one of the two simulated lines and was determined to occur when there was no line in the results with all of its parameters within 4 times the standard deviations of the known signal parameters used to generate the simulation. The standard deviations for each parameter were generated from the square root of the CR bounds calculated from the simulation parameters, N, and noise. Later, in sections 4.4 and 4.5 the definition of failure will be more stringent and will also include those results which contain extraneous lines.

In Section 4.2 we will find the optimal value (generally specified as a fraction of N) for the lowest failure rate of the model order (L). In terms of accuracy and precision the optimal L has been defined previously to be 0.48 to 0.72 [12]. We will extend this definition to failure rate and show that the optimal L for the lowest failure rate falls in the range of that for optimal accuracy and precision.

In section 4.3 we will demonstrate that there is an optimal value of N which gives the lowest failure rate of the analysis procedure. We will show that in contrast to reference [17] where the optimal number of data points for the Enhancement Procedure (EP) which precedes LPSVD is completely dependent on the line having the largest relaxation time (smallest magnitude of α) and an arbitrary N for the LPSVD procedure.

the optimal number of data points used for analysis using LPSVD preceding NMLE is dependent not only on the signal decay, but is dependent on the resonance line spacing.

In section 4.4 the three different procedures developed in section 3.4 for identifying and removing the spurious noise related lines from the results will be demonstrated, contrasting the success rates of each procedure. We will show that real/imaginary subsectioning performs poorly relative to the other two techniques and that even/odd subsectioning and subsectioning by acquisition perform similarly.

Section 4.5 will show the results of a totally automated procedure incorporating the optimal selection of input parameters N, L, and regularization, and noise line removal processing in terms of failure, contrasted with LPSVD using a predetermined cutoff value and N.

Section 4.6 expands the simulated two line spectra of the preceding sections into a simulation of a typical muscle phosphorus spectrum containing 6 lines. The automated processing of section 4.5 will be applied to simulations varying noise and Pi/PCr ratios.

Finally, in section 4.7 the processing technique (4.5) will be applied to actual data acquired from human muscle.

All simulations in sections 4.1 through 4.5 are based on a two line spectrum with relative amplitudes, decay rates, and frequencies which are representative of those found

in *in-vivo* spectroscopy. The basic parameters selected are shown in Table 4.1. Throughout these sections these parameters will be referenced and specific values modified to generate the simulation data. Figure 4.0.1a shows the real part of the simulated FID generated from the parameters in Table 4.1 with noise levels of $\sigma = 0$, 20, and 50. Figure 4.0.1b shows the real part of the frequency domain form. Note that the direction of the positive x-axis is reversed in the frequency domain to be consistent with the conventions of NMR spectroscopy.

	Amplitude (A)	Phase Angle (ϕ)	Decay Rate (α)	Frequency (f)
Line 1	200	0	0.031	-0.12
Line 2	100	0	0.062	-0.16

Table 4.1

The parameters of the reference spectrum used to generate the simulations in sections 4.1 through 4.5.

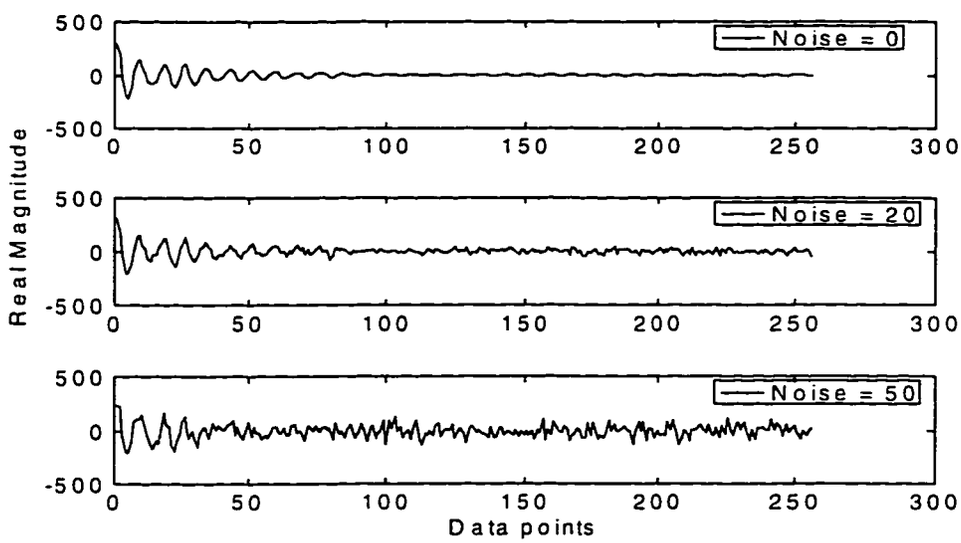

Figure 4.0.1a

The real part of a simulated FID generated from the parameters of Table 4.1 for various noise levels.

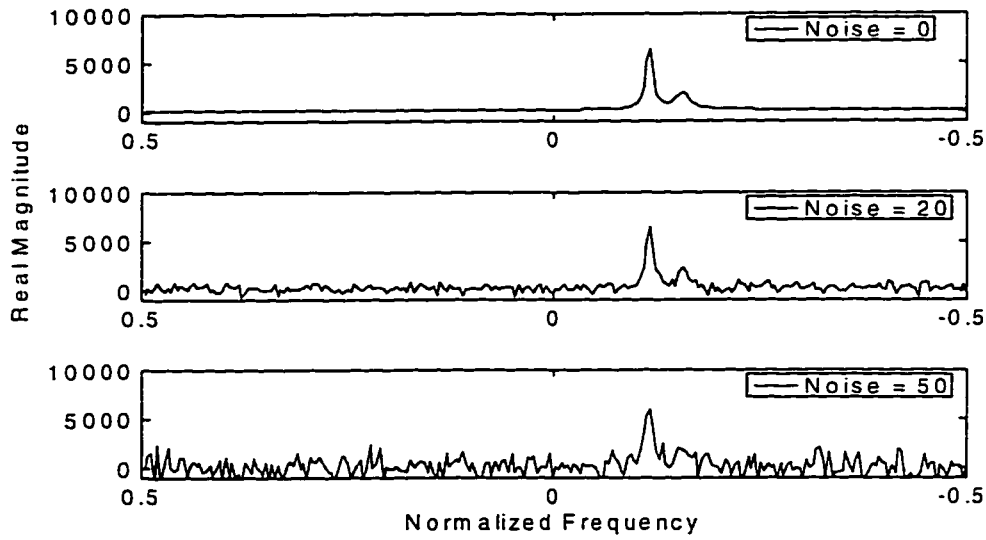

Figure 4.0.1b
The real part of the frequency domain spectrum generated from the FID's in Figure 4.0.1a.

4.1 Specification of Cutoff or Regularization

Here 3 methods for determining the cutoff value or regularization parameter are evaluated.

1. Manual regularization where the cutoff for SVD is arbitrarily set based on prior knowledge of the signal.

2. Discrete regularization where an algorithm determines the cutoff value based on the signal and its estimated noise variance.

3. Continuous regularization where a parameter λ is used to adjust all the singular values based on a noise estimate from the signal.

In all cases 100 realizations of noise were generated for each simulation of N, noise σ, and cutoff for the data. The parameters of table 4.1 were used to generate the simulated data.

4.1.1 Failure Rate with Noise for Manual Regularization

To demonstrate the effect the cutoff has on the parameters, the bias and variance of A_1 is plotted in figures 4.1.1a, 4.1.1b, and 4.1.1c for N = 50, 100, and 150, respectively, for cutoffs of 2, 10, and 20 for different noise levels. A lower cutoff seems to lead to a larger bias in the parameter, especially for N = 50.

Figures 4.1.1d, 4.1.1e, and 4.1.1f show the failure rate versus noise for manual regularization at N = 50, 100 and 150. Cutoffs of 2, 10, and 20 were used to show the effect cutoff has on the failure rate. N = 50 is considered to be an optimal value of N for the data set simulated (see section 4.3.3). A factor contributing to the decrease in the failure rate as the cutoff is increased is that the number of lines returned from the analysis increases along with the CR bounds making the probability of matching the original simulation parameters higher. Although it is more important that true lines do not get missed than it is that extra lines are returned by the LPSVD procedure, increasing the cutoff value to lower the failure rate is not necessarily the best method for doing this. Extra lines passed to the NMLE procedure will also appear in the final results and will affect the final accuracy and precision of the results. For this reason procedures which determine an optimal cutoff which does not miss the true lines and minimizes the number of extra lines generated are desired. Sections 4.1.2 and 4.1.3 will demonstrate two such methods.

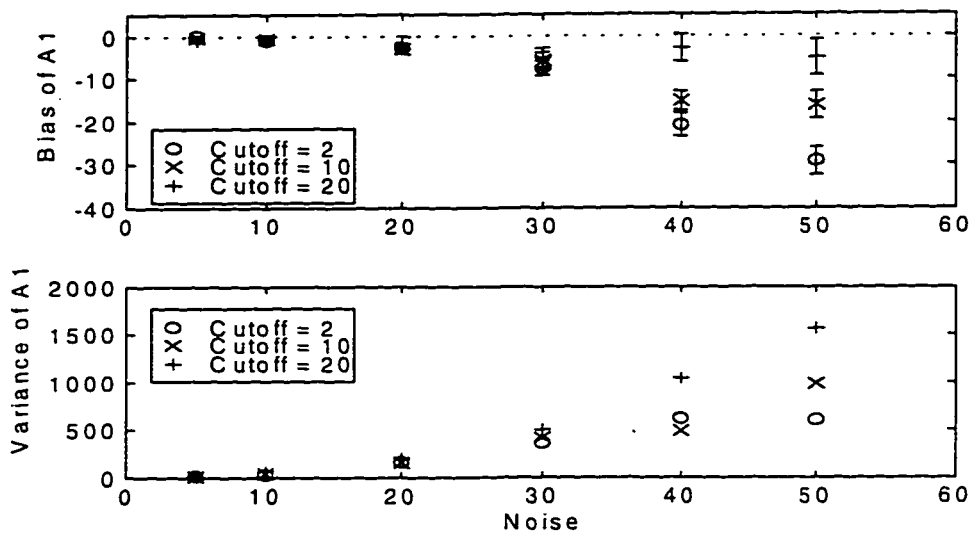

Figure 4.1.1a

The accuracy and precision of parameter A_1 as a function of the cutoff and the noise, analyzed using LPSVD only. Fifty data points were used and 100 simulations were analyzed for each cutoff and noise level.

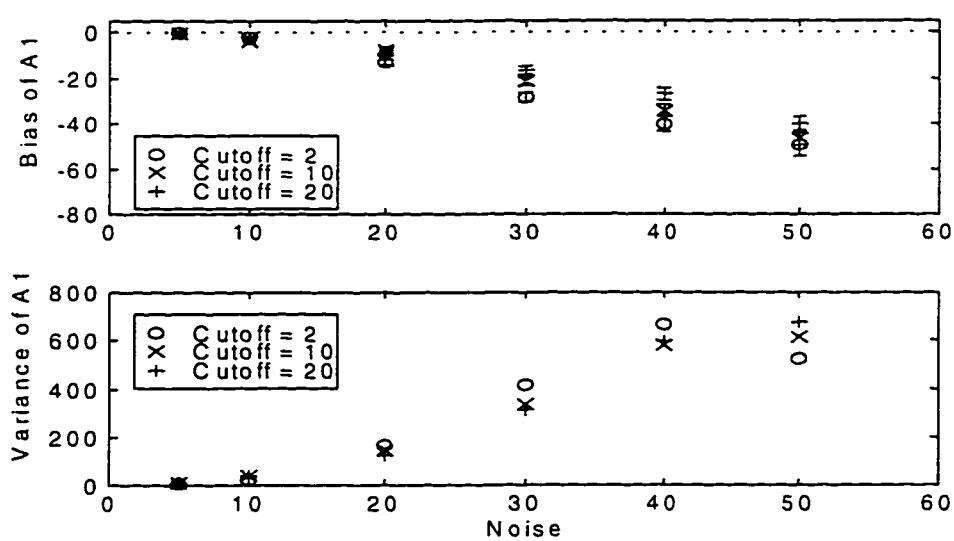

Figure 4.1.1b

The accuracy and precision of parameter A_1 as a function of the cutoff and the noise, analyzed using LPSVD only. One-hundred data points were used and 100 simulations were analyzed for each cutoff and noise level.

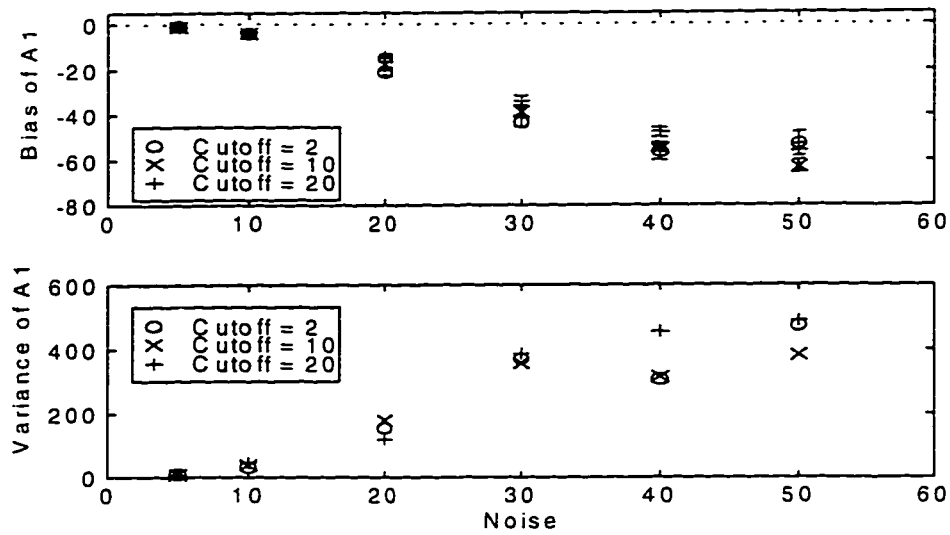

Figure 4.1.1c

The accuracy and precision of parameter A_1 as a function of the cutoff and the noise, analyzed using LPSVD only. One-hundred and fifty data points were used and 100 simulations were analyzed for each cutoff and noise level.

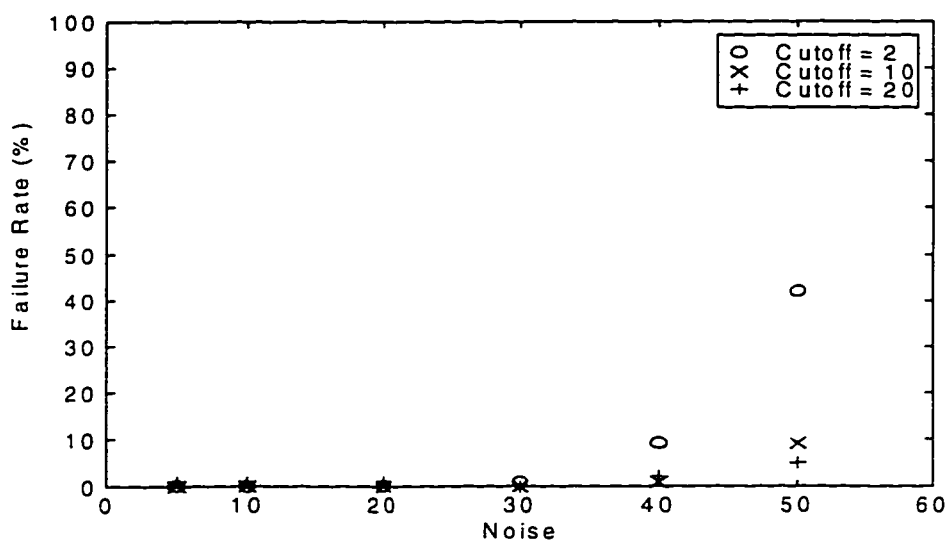

Figure 4.1.1d

The failure rate as a function of the cutoff and noise, analyzed using LPSVD. Fifty data points were used and 100 simulations were analyzed for each cutoff and noise level.

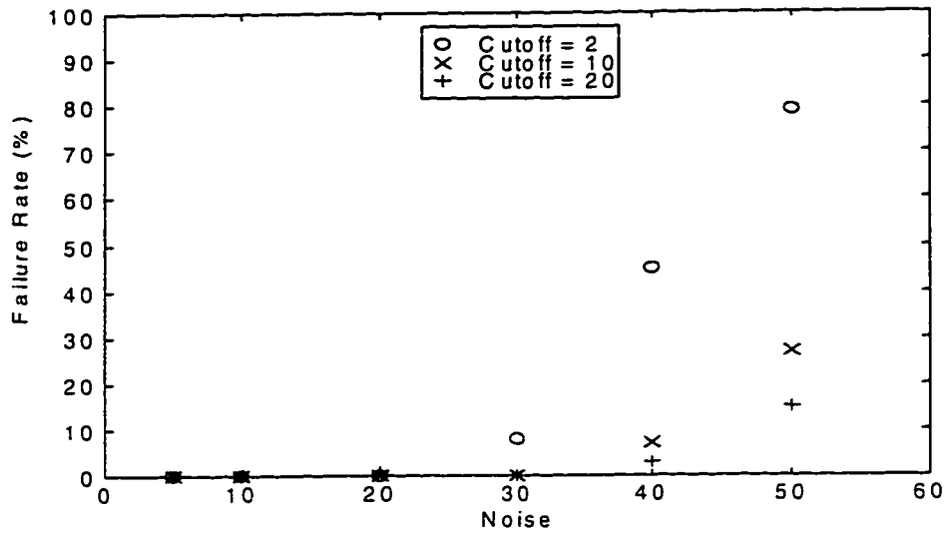

Figure 4.1.1e

The failure rate as a function of the cutoff and noise, analyzed using LPSVD. One-hundred data points were used and 100 simulations were analyzed for each cutoff and noise level.

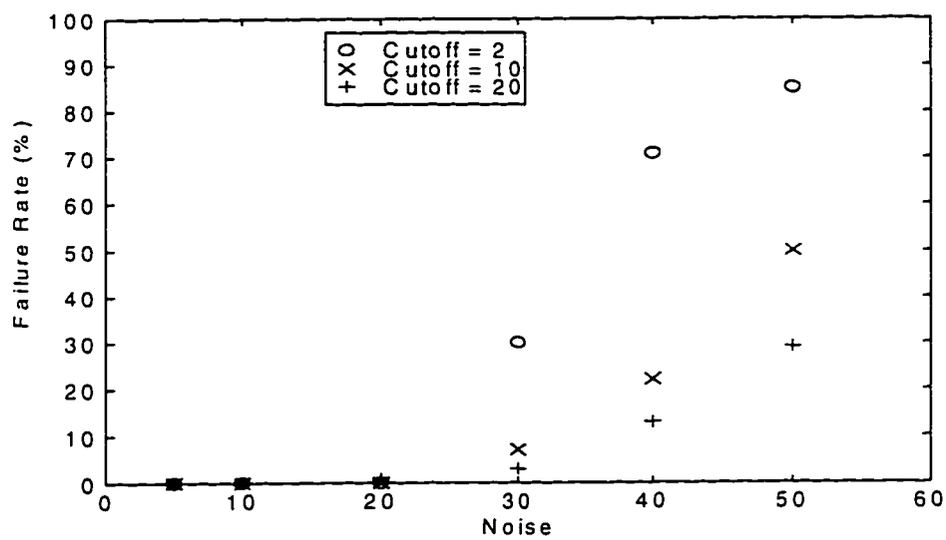

Figure 4.1.1f

The failure rate as a function of the cutoff and noise, analyzed using LPSVD. One-hundred fifty data points were used and 100 simulations were analyzed for each cutoff and noise level.

4.1.2 Failure Rate with Noise for Discrete Regularization

The results of the first of two automatic procedures for determining the cutoff is illustrated in figure 4.1.2. Failures for different values of N versus noise are shown. As seen in figure 4.1.4, the results for discrete regularization match those of manual regularization (Section 4.1.1) with a cutoff of 2, the difference being that the cutoff was not specified.

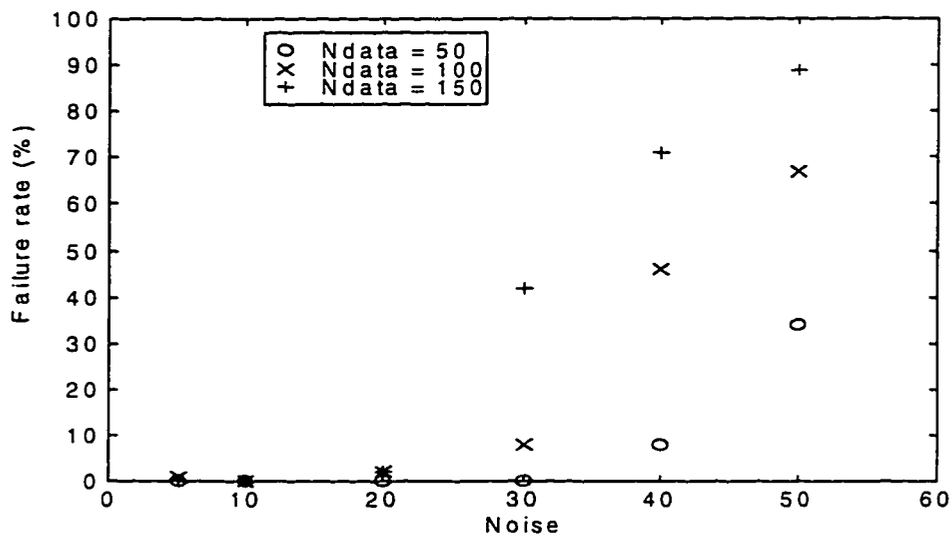

Figure 4.1.2
Failure rate as a function of the noise for discrete regularization for different dataset lengths (N). One-hundred simulations were run for each noise level and N.

4.1.3 Failure Rate with Noise for Continuous Regularization

Figure 4.1.3 shows the failure rate for the automatic regularization procedure of continuous regularization. Figure 4.1.4 shows that the results compare favourably with manual regularization with a cutoff of 10 for failure to identify the true lines. Figures 4.1.5a through 4.1.5e show the distribution of the number of lines returned from each

procedure for a noise level of $\sigma = 50$ and dataset length of $N = 50$. A manual regularization cutoff of 20 leads to an excessive number of noise lines being generated from the datasets whereas continuous regularization generates a much smaller number. Discrete regularization does not generate any noise lines for this case but missed a true line in 33% of the cases. For this reason continuous regularization will be the method of choice for determining the cutoff in the automatic procedure of section 4.5.

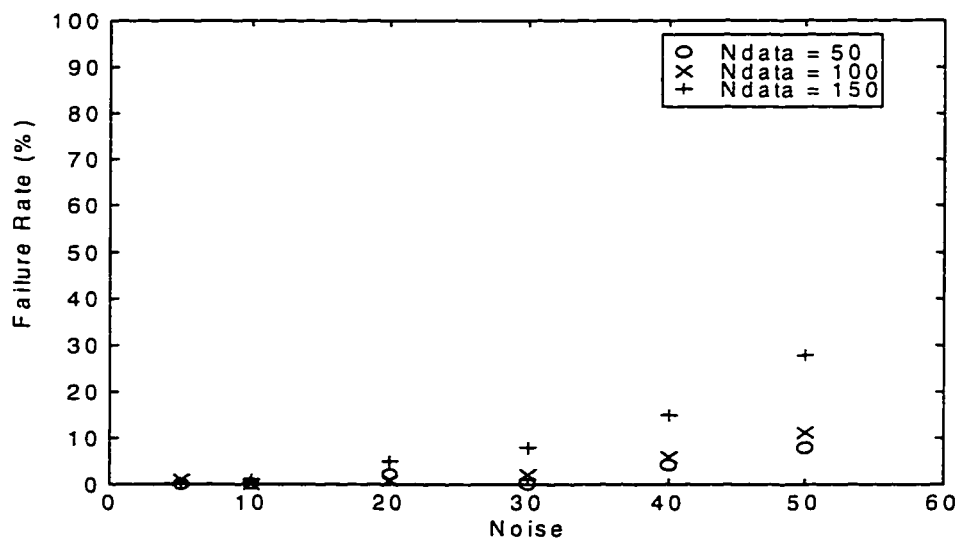

Figure 4.1.3
Failure rate as a function of the noise for continuous regularization for different dataset lengths (N). One-hundred simulations were run for each noise level and N.

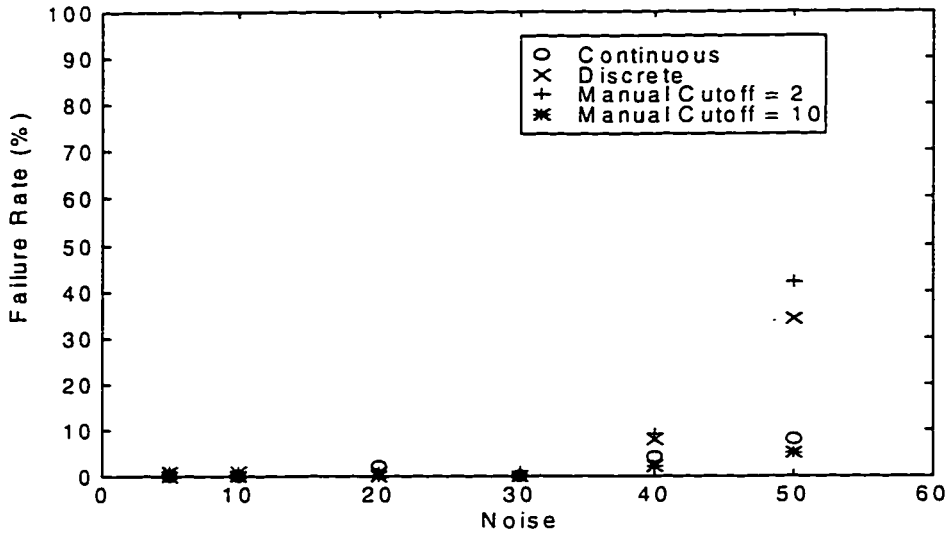

Figure 4.1.4

Failure rate as a function of the noise comparing manual, discrete, and continuous regularization for a dataset length (N) of 50. One-hundred simulations were run for each noise level and algorithm.

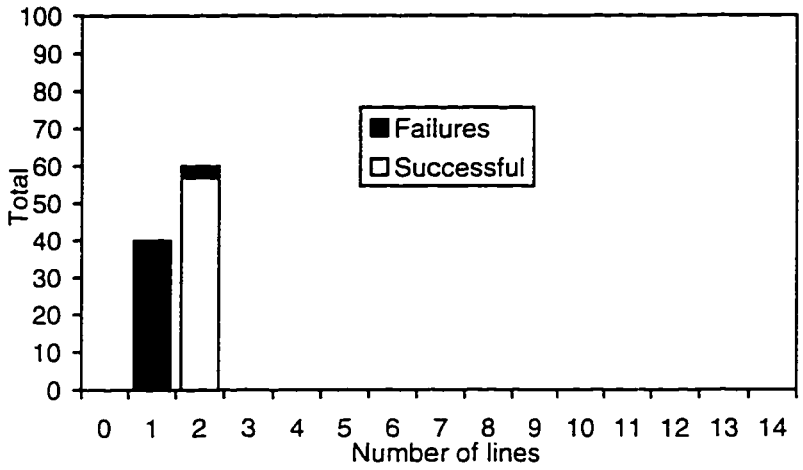

Figure 4.1.5a

A histogram showing the total number of results containing the specified number of lines for manual regularization with a cutoff of 2. The number of data points was N = 50, and the noise level was $\sigma = 50$.

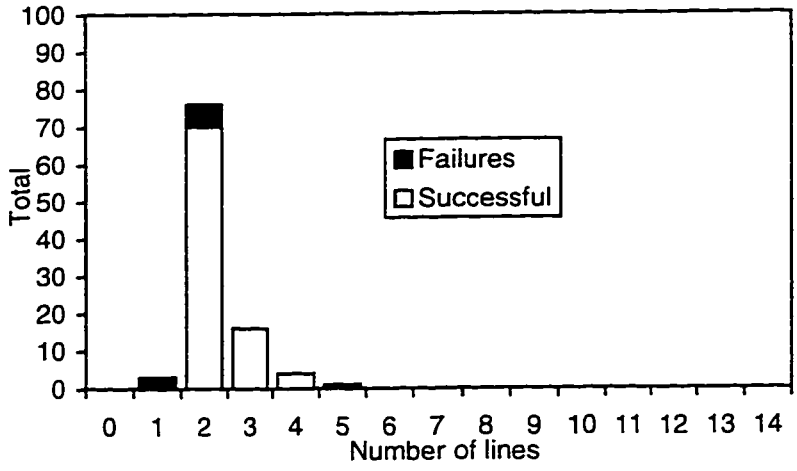

Figure 4.1.5b

A histogram showing the total number of results containing the specified number of lines for manual regularization with a cutoff of 10. The number of data points was N = 50, and the noise level was $\sigma = 50$.

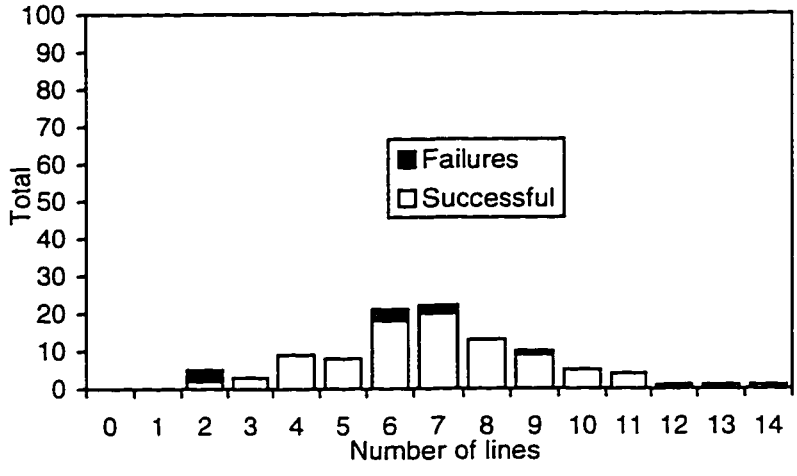

Figure 4.1.5c

A histogram showing the total number of results containing the specified number of lines for manual regularization with a cutoff of 20. The number of data points was N = 50, and the noise level was $\sigma = 50$.

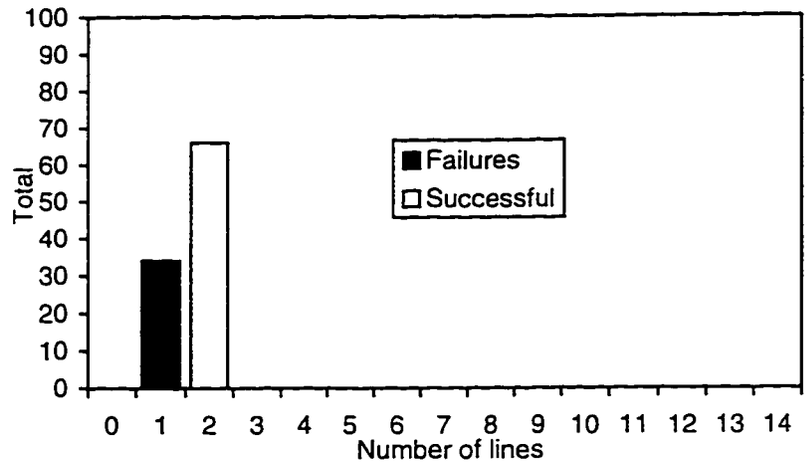

Figure 4.1.5d

A histogram showing the total number of results containing the specified number of lines for discrete regularization. The number of data points was N = 50, and the noise level was $\sigma = 50$.

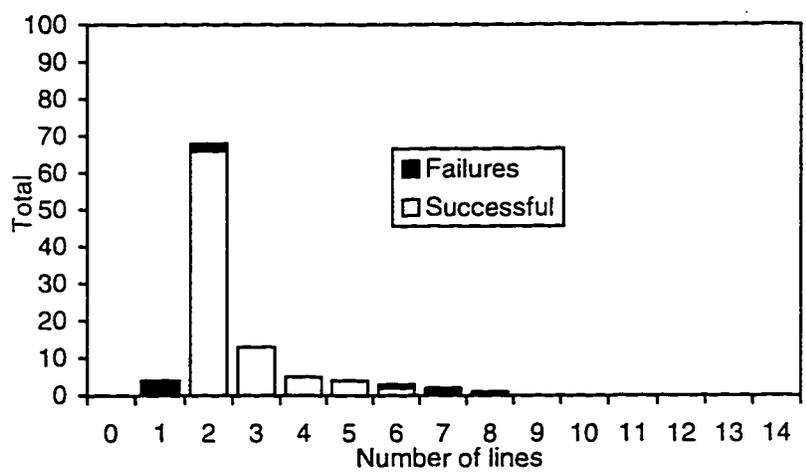

Figure 4.1.5e

A histogram showing the total number of results containing the specified number of lines for continuous regularization. The number of data points was N = 50, and the noise level was $\sigma = 50$.

4.2 Specification of Model Order (L)

Here we show the dependency of the failure rate and accuracy and precision of the results on the model order L. A two-line simulation varying the number of data points N and the model order as a function of N was generated using the parameters in table 4.1. N was varied from 20 to 200 and L from 1/8N to 7/8N. Five-hundred realizations for each

N and L were generated using a cutoff of 10 and noise level of $\sigma = 30$. A cutoff of 10 was used as this gave the lowest failure rate of the LPSVD analysis procedure (see figure 4.1.4). The noise level was chosen to give the most visible change in the measured parameters over the range of N and L used. Failure was as defined in section 4.1.1.

4.2.1 Accuracy and Precision with Model Order

Figures 4.2.1a through 4.2.1d show the effect of the model order (L) on the bias and variance of the amplitude and frequency parameters of the results. A model order of 0.5N seems to give the lowest bias across all the parameters at N = 50 and the bias response is fairly flat and higher for N = 200.

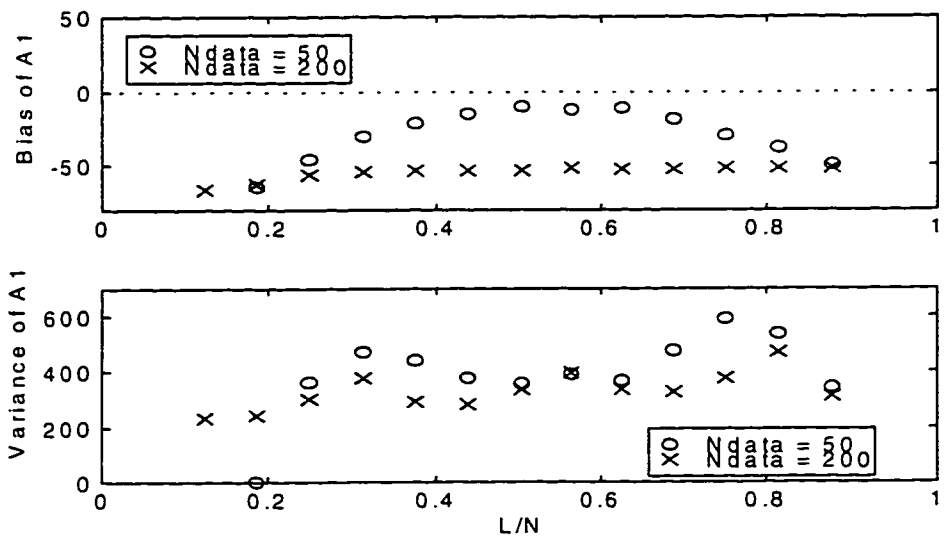

Figure 4.2.1a

The accuracy and precision of parameter A_1 as a function of the ratio L/N and the number of data points (N) analyzed using LPSVD only. A cutoff of 10 was used and 500 simulations were analyzed for each L/N and N with a noise level of $\sigma = 30$.

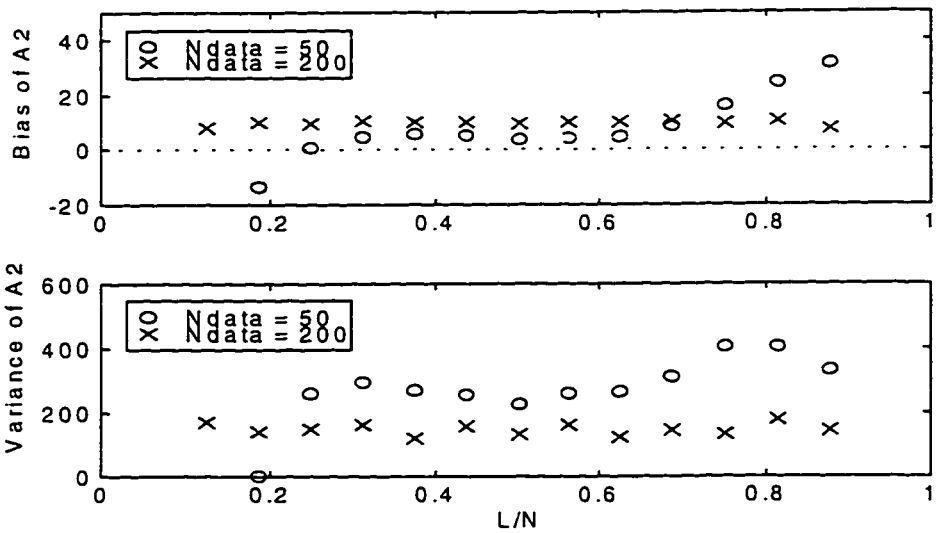

Figure 4.2.1b

The accuracy and precision of parameter A_2 as a function of the ratio L/N and the number of data points (N) analyzed using LPSVD only. A cutoff of 10 was used and 500 simulations were analyzed for each L/N and N with a noise level of $\sigma = 30$.

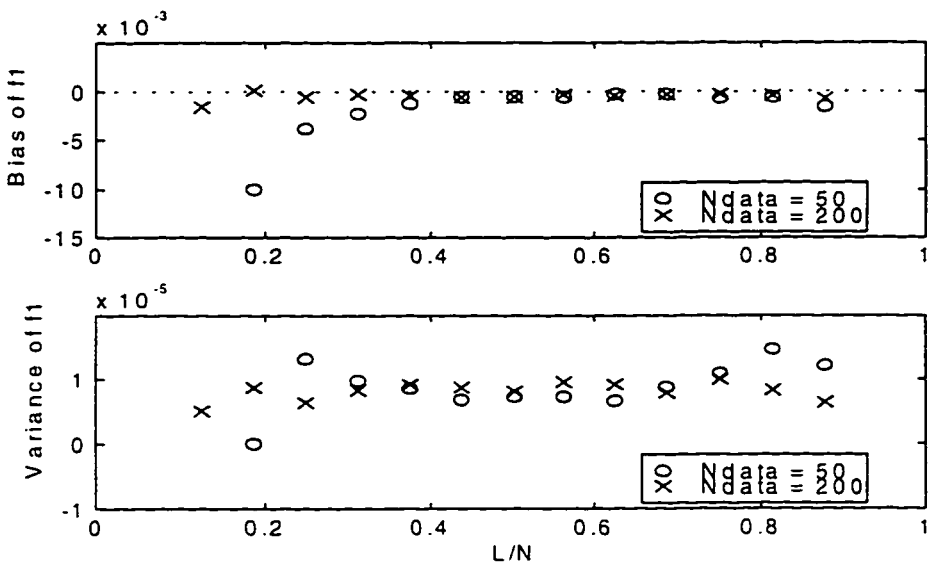

Figure 4.2.1c

The accuracy and precision of parameter f_1 as a function of the ratio L/N and the number of data points (N) analyzed using LPSVD only. A cutoff of 10 was used and 500 simulations were analyzed for each L/N and N with a noise level of $\sigma = 30$.

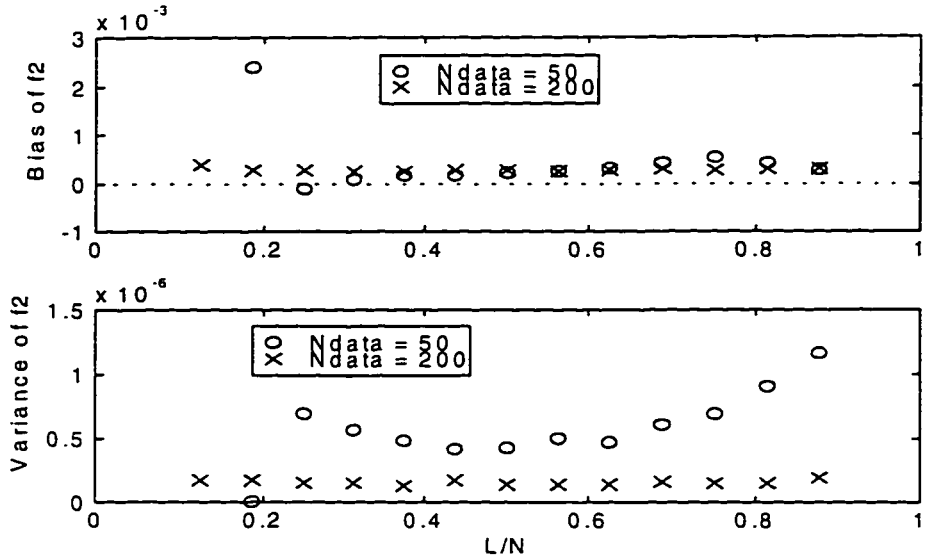

Figure 4.2.1d

The accuracy and precision of parameter f_2 as a function of the ratio L/N and the number of data points (N) analyzed using LPSVD only. A cutoff of 10 was used and 500 simulations were analyzed for each L/N and N with a noise level of $\sigma = 30$.

4.2.2 Failure Rate with L

Figure 4.2.2 shows the number of failures as a function of the relative model order (L/N) for two different N values. As can be seen there is a broad range of L/N which gives a relatively constant failure rate. One is justified in setting L to be anywhere from 0.4 to 0.7 N for all N shown with little variation in the failure rate. Because of the limited dependency of failure rate on L and the minimum bias found at 0.5N in figures 4.2.1a through 4.2.1h for N = 50, a model order of 0.5N has been used in all other sections in this thesis and is assumed to be the optimal value of L.

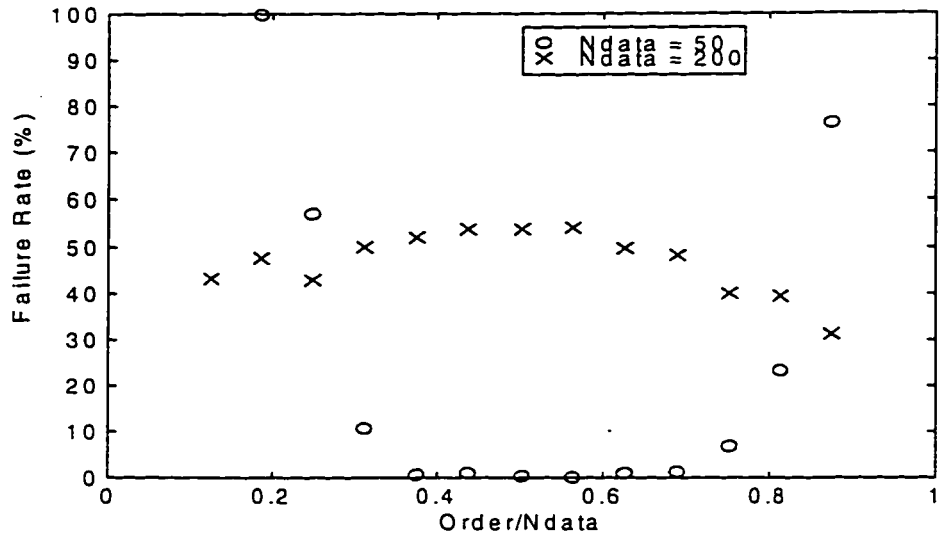

Figure 4.2.2
Failure rate as a function of the relative model order (L/N) analyzed for two different dataset lengths (N) using LPSVD. A cutoff of 10 was used and 500 simulations at each order and N were analyzed with a noise level of $\sigma = 30$.

4.3 Specification of Number of Data Points (N)

Here we show the dependency of analysis time, accuracy and precision, and failure rate on the number of data points used in the analysis. The two-line simulation of table 4.1 is used varying the noise level σ and parameters α and f to demonstrate the individual dependencies.

4.3.1 Dependency of the Analysis Time on N

The number of data points (N) was varied over the range 20 to 200 for noise levels of $\sigma = 5$, 20, and 50. Fifty different realizations for each noise level and N were analyzed using LPSVD with a manual cutoff, LPSVD using continuous regularization,

and NMLE, and the mean time for the realizations was calculated. The parameters used for each realization were those given in table 4.1. The model order was set to N/2.

Figure 4.3.1 shows the mean analysis time for each N and σ for all three algorithms using a 166 MHz Intel Pentium based computer and Matlab 4.2c.1. Of note in the graph is the $O(N^3)$ dependency of the analysis time and the independence of the time on signal noise. It is obvious that to minimize the amount of processing time needed and hence the time between the experiment and the generation of the results we need to minimize the number of data points used in the analysis and that arbitrary selection of this parameter is not desirable. Also of interest is the fact that NMLE is the most time consuming algorithm up to approximately N = 150 data points after which LPSVD with continuous regularization becomes the most time consuming. An important point to consider, though, is that the number of lines passed to the NMLE procedure will affect its processing time. This is indirectly illustrated by the increase in the processing time for the higher noise level of $\sigma = 50$. The processing time increases due to the increased number of noise lines passed to the procedure which were generated by LPSVD. The NMLE procedure processing time is linearly dependent on the number of lines passed to it. Thus, a six line spectrum will take three times as long to be processed by NMLE as a two line spectrum. From a processing time standpoint it is important to minimize the number of false lines passed to the procedure. In terms of an experiment which could take an hour to acquire hundreds of spectra, the savings of 10 to 20% of the processing time (at a few minutes per spectrum for example) needed is substantial. Section 4.4 will attempt to minimize this by subsectioning the data to identify these lines and remove them.

Figure 4.3.1b illustrates the effect of the model order on the time required to process using the LPSVD procedure. The cutoff has no effect on the time required for the LPSVD procedure.

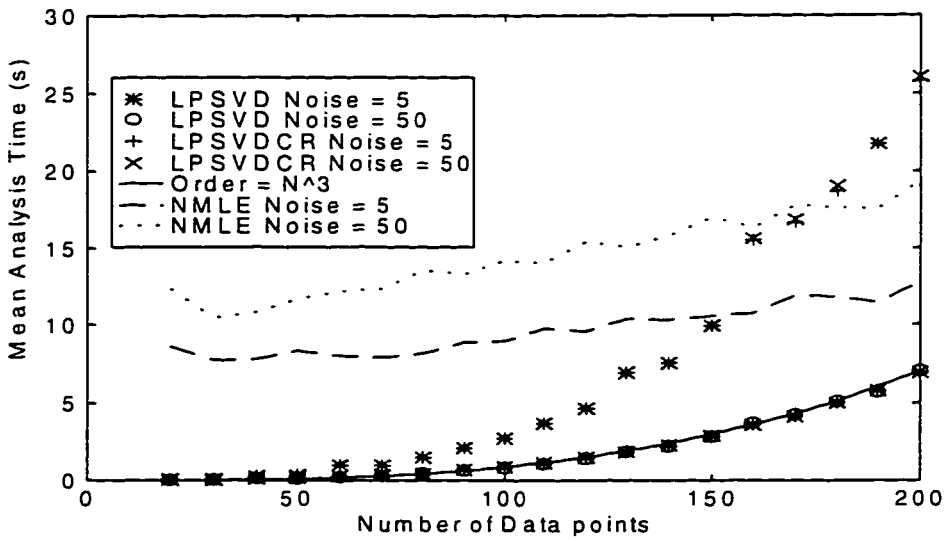

Figure 4.3.1a

The mean analysis time required to process a two line spectrum using LPSVD with a cutoff of 2, LPSVD with continuous regularization (LPSVDCR), and NMLE, for noise levels of $\sigma = 5$ and 50. The number of data points (N) used in the analysis was varied and the mean calculated from 50 realizations at each noise, N, and algorithm..

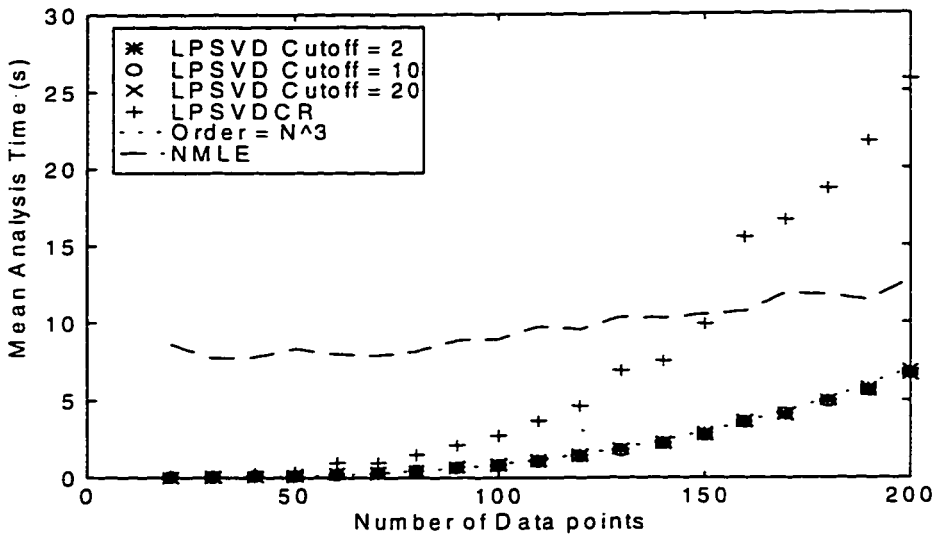

Figure 4.3.1b

The mean analysis time required to process a two line spectrum using LPSVD for different cutoffs, LPSVD with continuous regularization (LPSVDCR), and NMLE, for a noise level of $\sigma = 5$. The number of data points (N) used in the analysis was varied and the mean calculated from 50 realizations for each cutoff, N, and algorithm.

4.3.2 Accuracy and Precision with N

To demonstrate the effect N has on the accuracy and precision, figures 4.3.2a through 4.3.2d show the bias and variance of the amplitude and frequency parameters as a function of N for noise realizations of $\sigma = 5$, 30, and 50. Five-hundred realizations of noise for each N and σ were added to the signal generated from the parameters of table 4.1. The signals generated were analyzed using LPSVD only with a model order L = N/2 and a cutoff of 10.

Obvious from the graphs is the increase in the parameter bias of the second line as N is increased. Higher noise levels also led to a larger bias in all cases. Of note is the flat response of the frequency to variations in N. The optimal value of N in this case would

seem to be 30 as this is where the bias seems to be minimized for all parameters with the exception of ϕ_1 at all noise levels. As will be seen in 4.3.3, this is not the optimal value of N.

Since these parameters are the starting values that are passed to the NMLE fitting procedure to produce results with zero bias and a variance equal to the Cramer-Rao (CR) bound, it is important that the parameters generated by the LPSVD procedure are as close to the true values as possible. The NMLE fitting procedure relies on a minimizing algorithm which, given large enough biases in the starting values, can find false minima and will then return results with larger than necessary biases.

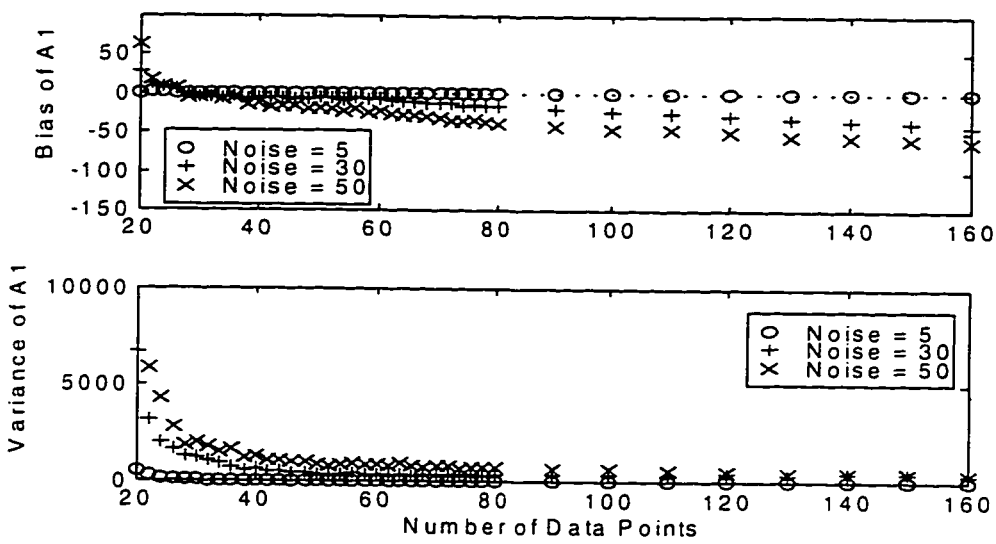

Figure 4.3.2a

The accuracy and precision of parameter A_1 as a function of the number of data points (N) analyzed using LPSVD only for various noise levels. A cutoff of 10 was used and 500 simulations at each noise level and N were analyzed.

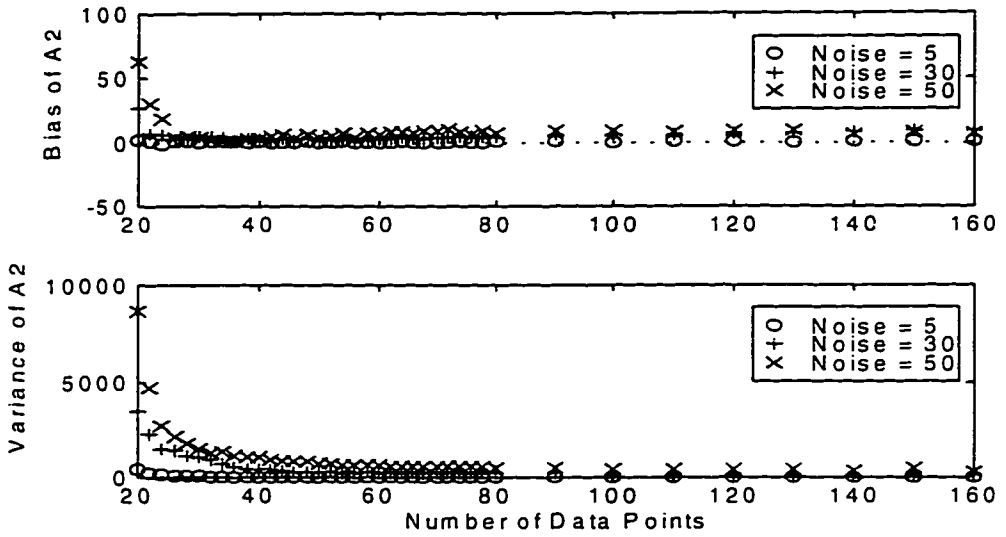

Figure 4.3.2b

The accuracy and precision of parameter A_2 as a function of the number of data points (N) analyzed using LPSVD only for various noise levels. A cutoff of 10 was used and 500 simulations at each noise level and N were analyzed.

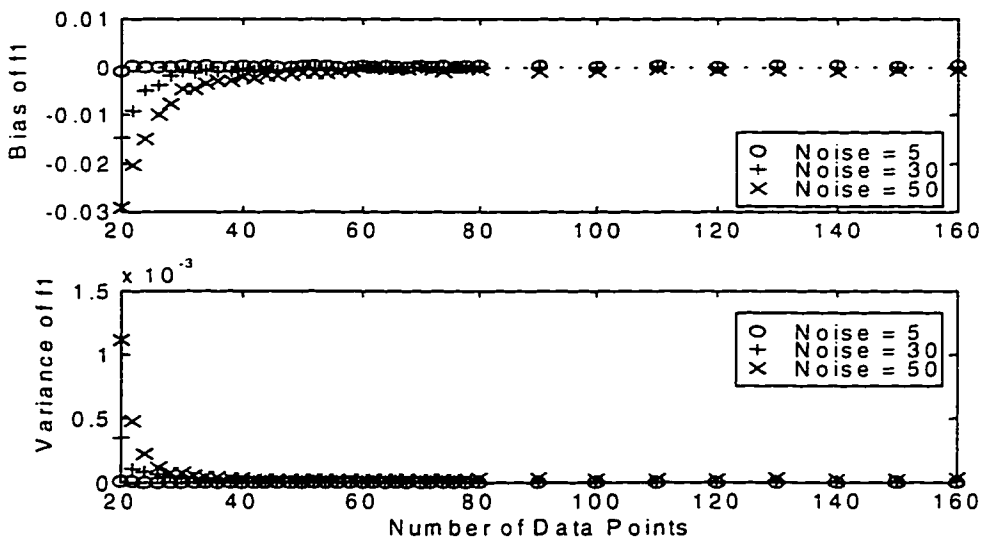

Figure 4.3.2c

The accuracy and precision of parameter f_1 as a function of the number of data points (N) analyzed using LPSVD only for various noise levels. A cutoff of 10 was used and 500 simulations at each noise level and N were analyzed.

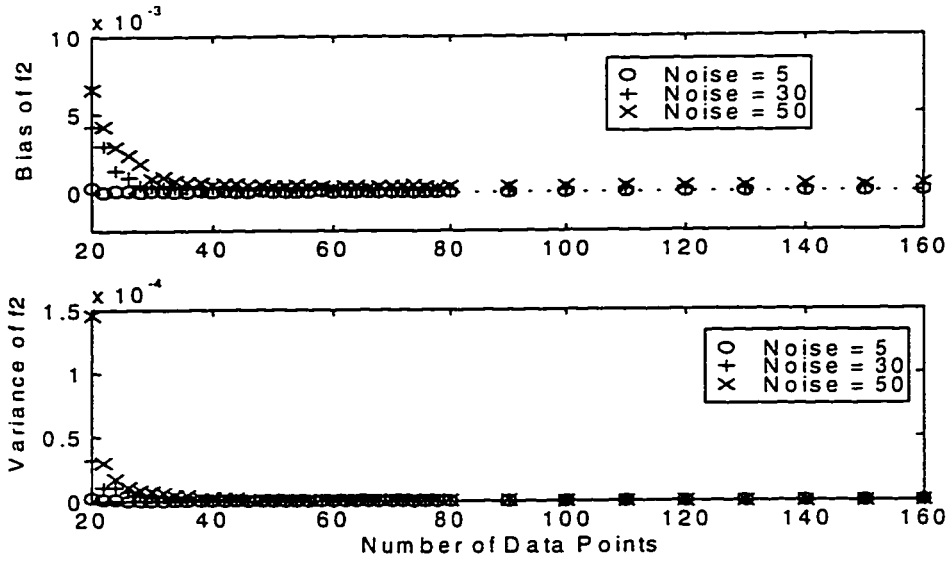

Figure 4.3.2d

The accuracy and precision of parameter f_2 as a function of the number of data points (N) analyzed using LPSVD only for various noise levels. A cutoff of 10 was used and 500 simulations at each noise level and N were analyzed.

4.3.3 Failure Rate with N

Figure 4.3.3 shows the total number of line identification failures as a function of N and noise. Five-hundred realizations at each noise level and N were analyzed using LPSVD only with a cutoff of 10 and a model order of N/2. LPSVD with a cutoff of 10 was chosen over continuous regularization (CR) in this instance as its performance for this two-line simulation in terms of failure is similar to that of CR and it executes several times faster. In general, for an unknown number of lines, CR should be used. The same parameters as in 4.3.2 were used to generate the simulations. Failure was as defined in section 4.1.

An interesting result can be seen in figure 4.3.3. There appears to be an optimal N where the failure rate is minimized. In this case it appears at approximately N = 50 for a

noise $\sigma = 50$. Increasing N past this has the effect of increasing the failure rate substantially, especially at higher noise levels. Section 4.3.2 showed that increasing N past a certain point did not improve the accuracy and precision generated by LPSVD. Here we have shown that we might actually degrade the performance of LPSVD by increasing N. As will be seen in section 4.3.4, this optimal N can be calculated from the characteristics of the signal.

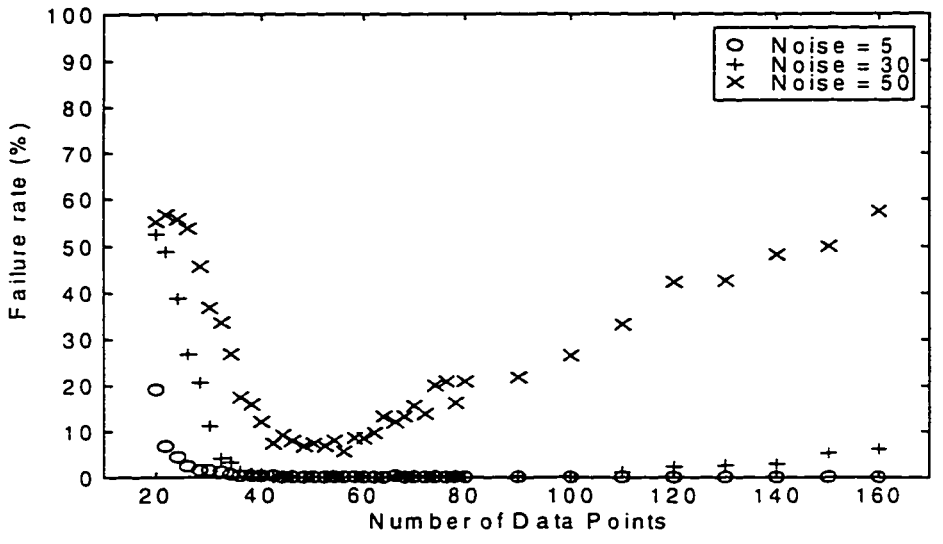

Figure 4.3.3
Failure rate as a function of the number of data points (N) analyzed for several different noise levels using LPSVD. A cutoff of 10 was used and 500 simulations at each noise level and N were analyzed.

4.3.4 Failure Rate with Maximum Line Frequency, Amplitude, and Phase

Figure 4.3.4a shows the failure rate as a function of the line frequency f_l and N at a noise of $\sigma = 30$. The line separation was kept constant at 0.035. Larger line separations did not exhibit clearly identifiable minima in the failure rate as they had large ranges

where the failure rate was zero. Five-hundred realizations for each N and spacing were run using LPSVD only and a cutoff of 10 and model order L = N/2. All other simulation parameters were as in table 4.1 and the same criteria for failure were used as in section 4.1. Figure 4.3.4b shows the failure rate as a function of the amplitude of line 2. The line-1 amplitude was kept constant at $A_1 = 200$ and the line-2 amplitude was varied with $A_2 =$ 50, 100, 150, 200. Figure 4.3.4c shows the total number of failures as a function of the phase of line-2. The line-1 phase was kept constant at $\phi_1 = 0$ and the line 2 phase was varied with $\phi_2 = 0, 90°, 180°, 270°$.

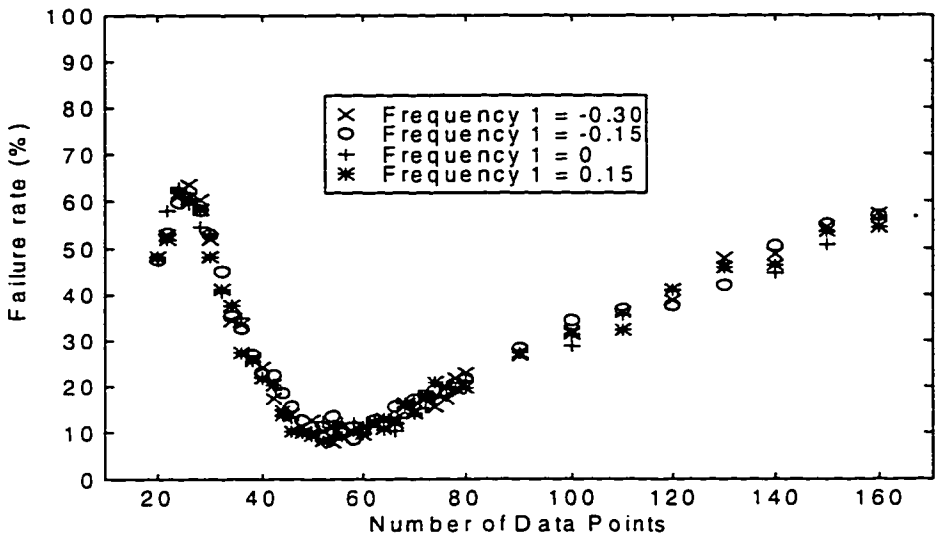

Figure 4.3.4a

Failure rate of the LPSVD analysis procedure as a function of the number of data points (N) used and the highest line frequency for a two line spectrum. A cutoff of 10 was used and 500 simulations at each N and frequency were analyzed with a noise of $\sigma = 50$.

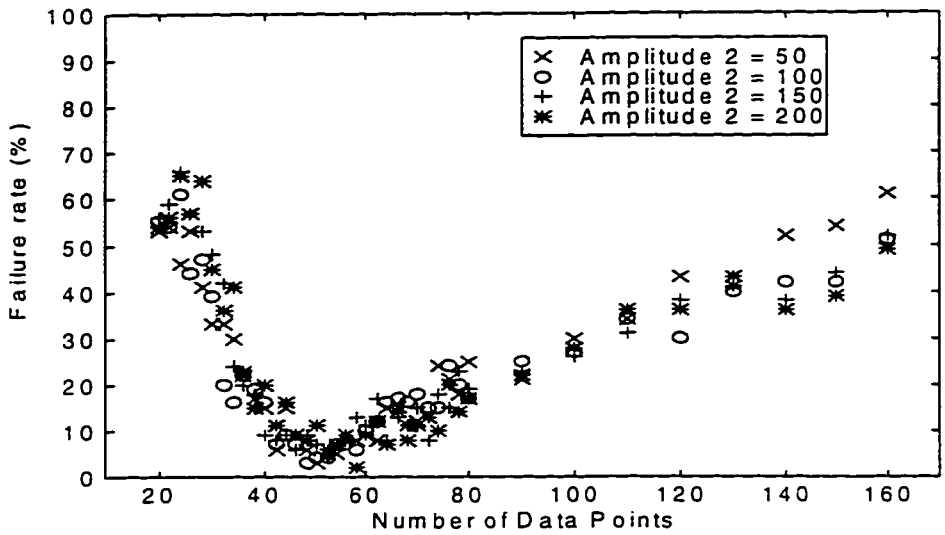

Figure 4.3.4b

Failure rate of the LPSVD analysis procedure as a function of the number of data points (N) used and the amplitude of the second line for a two line spectrum. A cutoff of 10 was used and 100 simulations at each N and line separation were analyzed with a noise level of $\sigma = 50$.

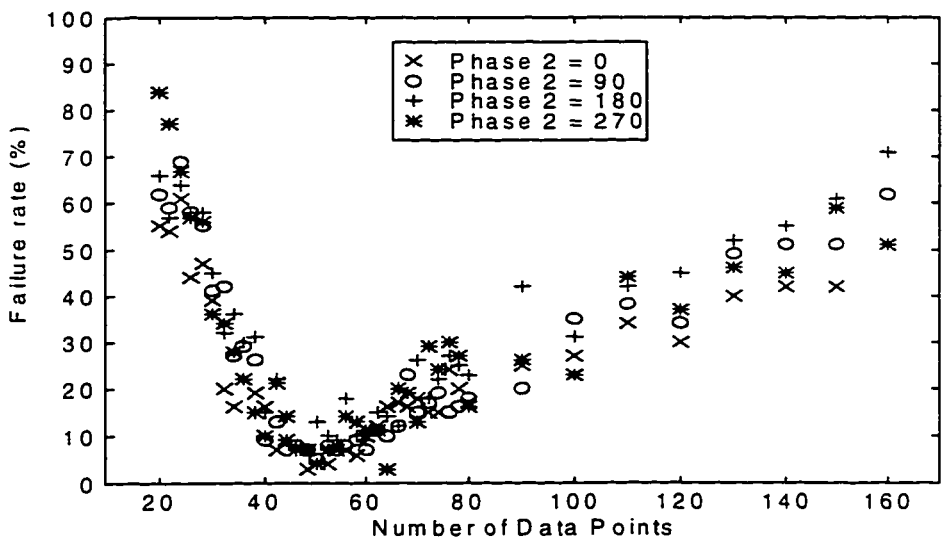

Figure 4.3.4c

Failure rate of the LPSVD analysis procedure as a function of the number of data points (N) used and the phase of the second line for a two line spectrum. A cutoff of 10 was used and 100 simulations at each N and line separation were analyzed with a noise level of $\sigma = 50$.

There appears to be no dependency on the maximum line frequency, the amplitude, or the phase as can be seen in figures 4.3.4a, 4.3.4b, or 4.3.4c. Of note is the first minimum of each plot before N = 40. This minimum is believed to be caused by the large CR bound calculated with a small N and high noise level matching many of the results with at least 2 lines found, i.e., almost any result appears within 4σ of the true parameters.

The importance of choosing an N which gives the lowest failure rate becomes apparent when trying to resolve closely spaced features in high noise. Missing lines will lead to biases in the results generated by the NMLE procedure as it attempts to fit two lines in the FID using a single line. The NMLE procedure is not capable of changing the number of parameters it will fit after the starting parameters are passed to it. Thus, it is essential that the LPSVD procedure has as low a probability of missing lines as possible.

4.3.5 Failure Rate with Decay and Line Separation

Figure 4.3.5a shows the dependence of failure rate on the line decay parameter α_l for a constant line separation of $\Delta f = 0.04$ and α_l equal to 0.1, 0.075, and 0.05. All other parameters were as in table 4.1. The noise level was set at $\sigma = 50$ such that a clear minimum would be visible. There appears to be a dependency of the optimal N for minimum failure rate on the decay parameter. Faster decays (larger α) cause the optimal N to be reduced.

Figure 4.3.5b shows the dependence of failure rate on Δf for a constant value of the decay parameter $\alpha_l = 0.075$ with Δf varied from 0.03 to 0.06 in 0.01 steps. The noise level was set at $\sigma = 50$ as in figure 4.3.5a. All other parameters were as in table 4.1. There appears to be a dependency of the optimal N for minimum failure rate on the line separation. The further apart the two lines, the lower the optimal N appears to be.

A comparison between the optimal N calculated from equation 3.1.1 and the optimal N estimated by smoothing the plots of figures 4.3.5a and 4.3.5b is shown in figure 4.3.5c. A continuous plot of the calculated optimal N from equation 3.1.1 is overlayed with the estimates generated. Equation 3.1.1 seems to give a reasonable estimate of the optimal N based on Δf and α_l for the ranges of these parameters simulated here for a two line case.

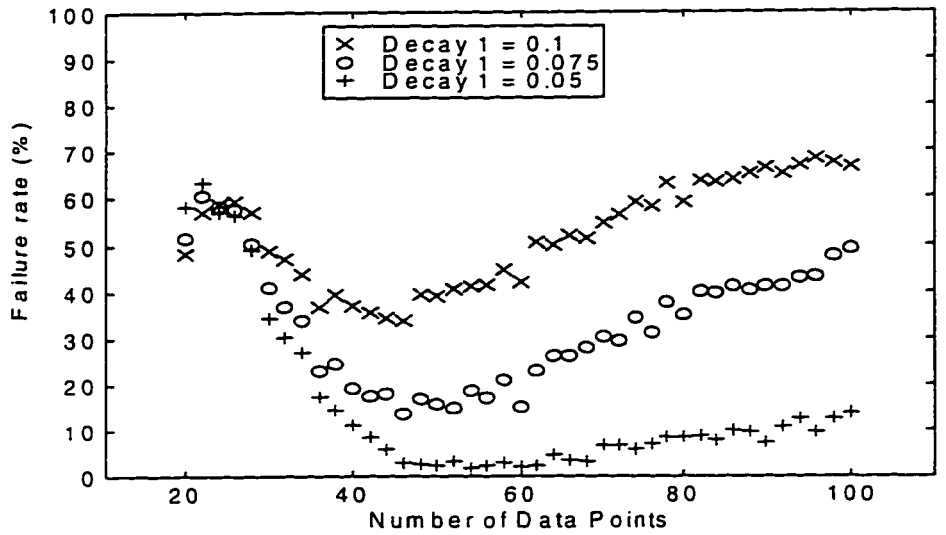

Figure 4.3.5a

Failure rate of the LPSVD procedure as a function of the number of data points (N) for three different decay rates and a constant line separation $\Delta f = 0.04$. A cutoff of 10 was used and 500 simulations were analyzed for each N and decay with a noise level of $\sigma = 50$.

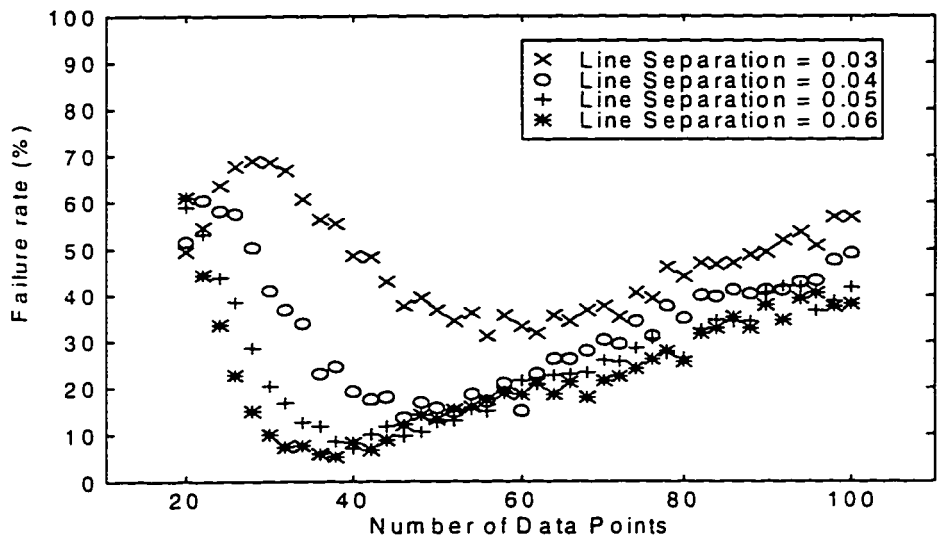

Figure 4.3.5b

Failure rate of the LPSVD procedure as a function of the number of data points (N) for four different line separations and a constant line decay rate of $\alpha_l = 0.075$. A cutoff of 10 was used and 500 simulations were analyzed for each N and Δf with a noise level of $\sigma = 50$.

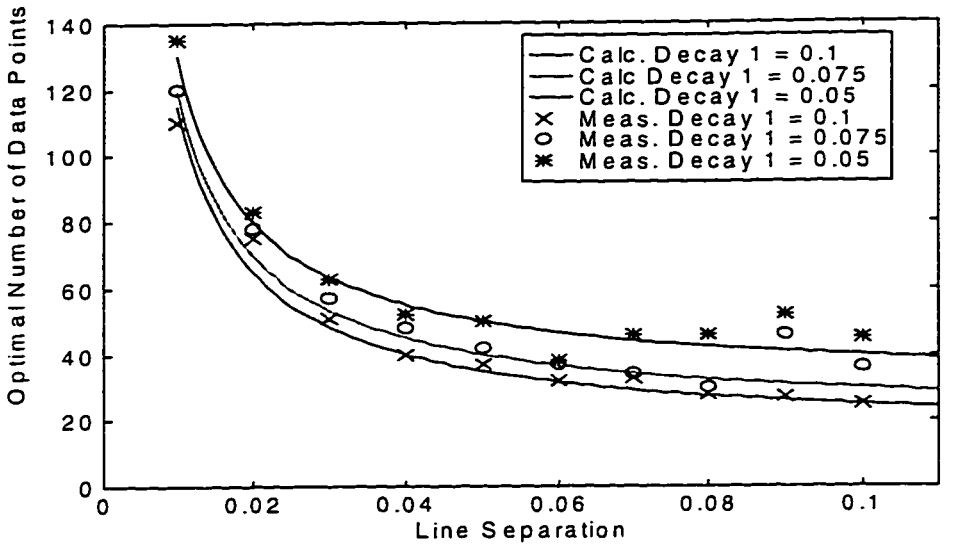

Figure 4.3.5c

A comparison of the optimal values of N approximated through equation [3.1.1] (calc.) and by determination of the minimum failure rate through simulation (meas.) for various decay rates and line separations.

4.3.6 Accuracy and Precision with Decay and Line Separation

Figures 4.3.6a through 4.3.6d demonstrate the bias and variance of the amplitude and frequency parameters of the two-line simulation as a function of the decay parameter α_1. Figures 4.3.6e through 4.3.6h demonstrate the bias and variance of all the amplitude and frequency parameters of the two line simulation as a function of the line separation Δf. It is clear that N should be greater than 30 data points for a reasonable bias in the parameters. As in section 4.3.2 it is desirable to keep the number of data points analyzed to a minimum such that the best estimates possible are passed to the NMLE algorithm while at the same time minimizing the probability of missing lines.

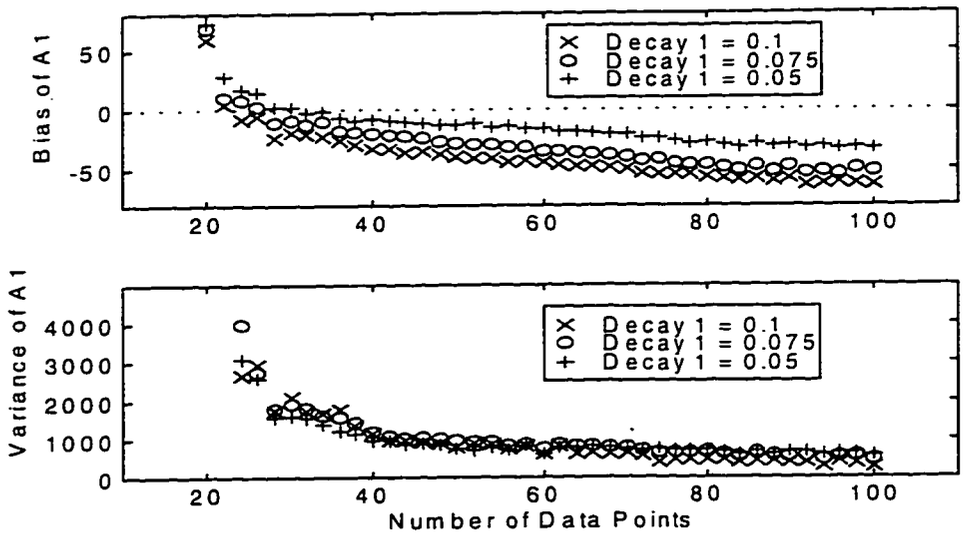

Figure 4.3.6a

The accuracy and precision of parameter A_1 as a function of the number of data points (N) and decay rate (α_1), analyzed using LPSVD only. A cutoff of 10 was used and 500 simulations were analyzed for each N and α_1 with a noise level of $\sigma = 50$.

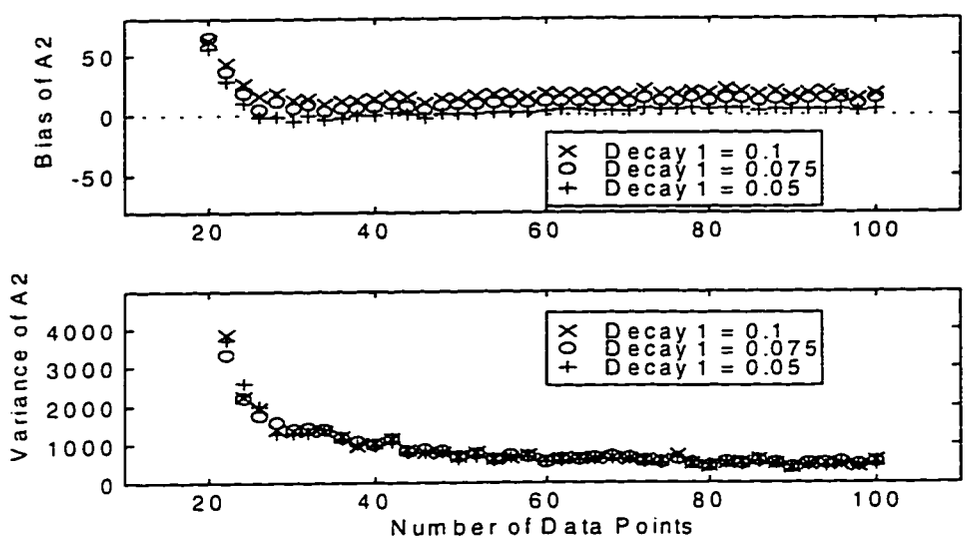

Figure 4.3.6b

The accuracy and precision of parameter A_2 as a function of the number of data points (N) and decay rate (α_1), analyzed using LPSVD only. A cutoff of 10 was used and 500 simulations were analyzed for each N and α_1 with a noise level of $\sigma = 50$.

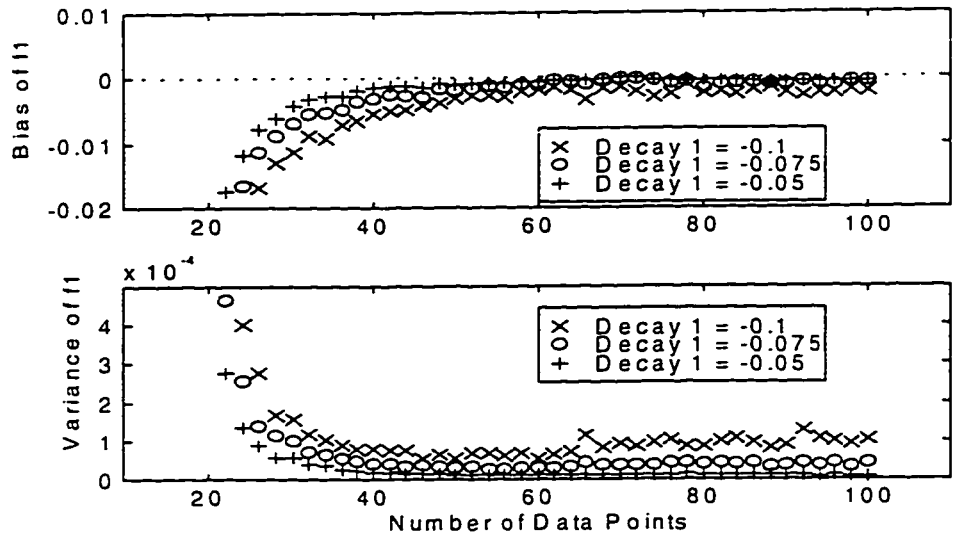

Figure 4.3.6c

The accuracy and precision of parameter f_1 as a function of the number of data points (N) and decay rate (α_1), analyzed using LPSVD only. A cutoff of 10 was used and 500 simulations were analyzed for each N and α_1 with a noise level of $\sigma = 50$.

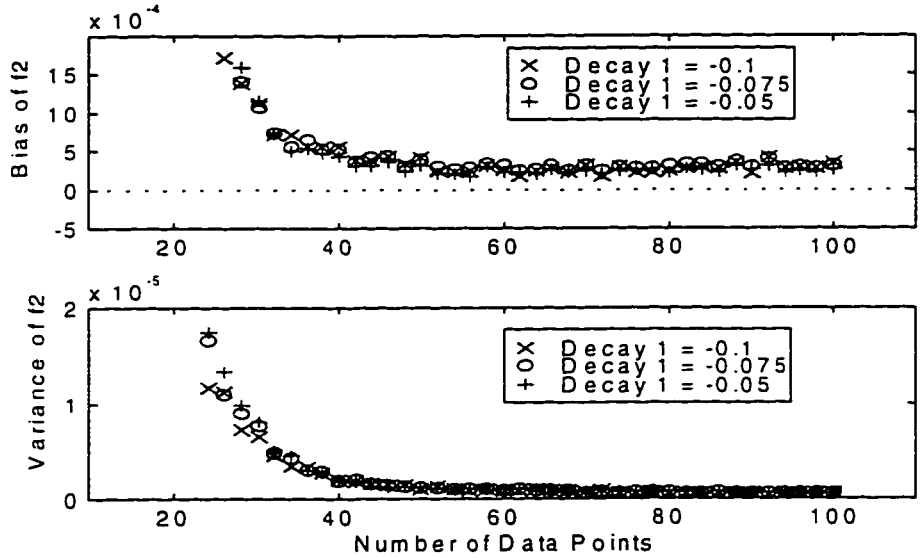

Figure 4.3.6d

The accuracy and precision of parameter f_2 as a function of the number of data points (N) and decay rate (α_1), analyzed using LPSVD only. A cutoff of 10 was used and 500 simulations were analyzed for each N and α_1 with a noise level of $\sigma = 50$.

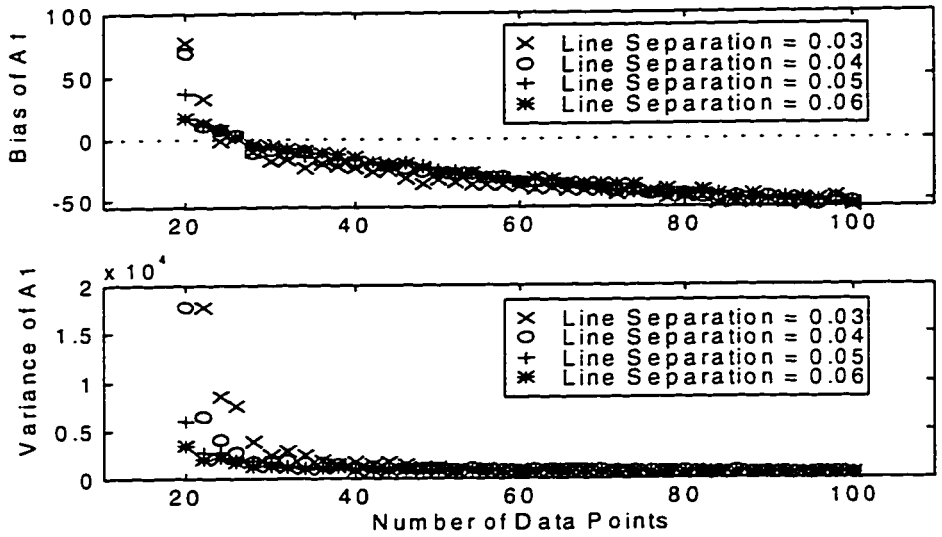

Figure 4.3.6e

The accuracy and precision of parameter A_1 as a function of the number of data points (N) and line separation (Δf), analyzed using LPSVD only. A cutoff of 10 was used and 500 simulations were analyzed for each N and Δf with a noise level of $\sigma = 50$.

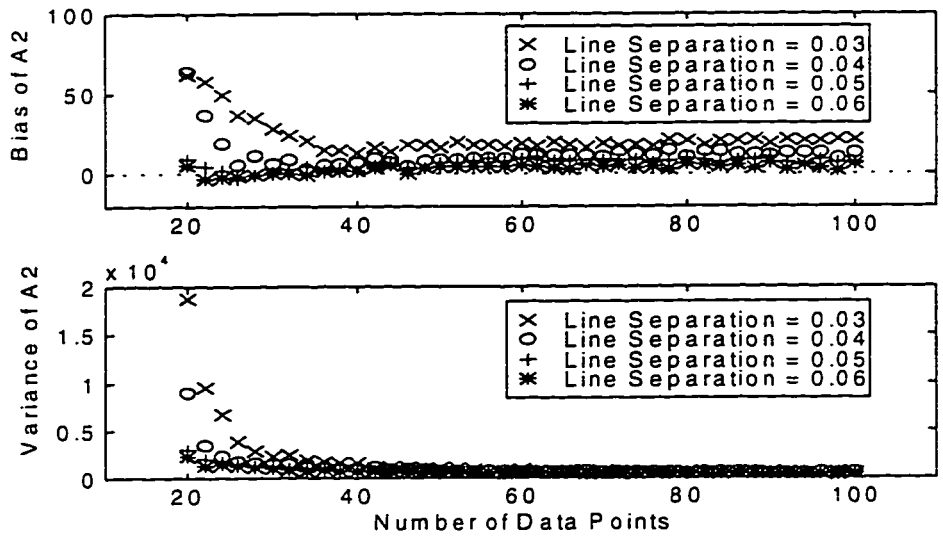

Figure 4.3.6f

The accuracy and precision of parameter A_2 as a function of the number of data points (N) and line separation (Δf), analyzed using LPSVD only. A cutoff of 10 was used and 500 simulations were analyzed for each N and Δf with a noise level of $\sigma = 50$.

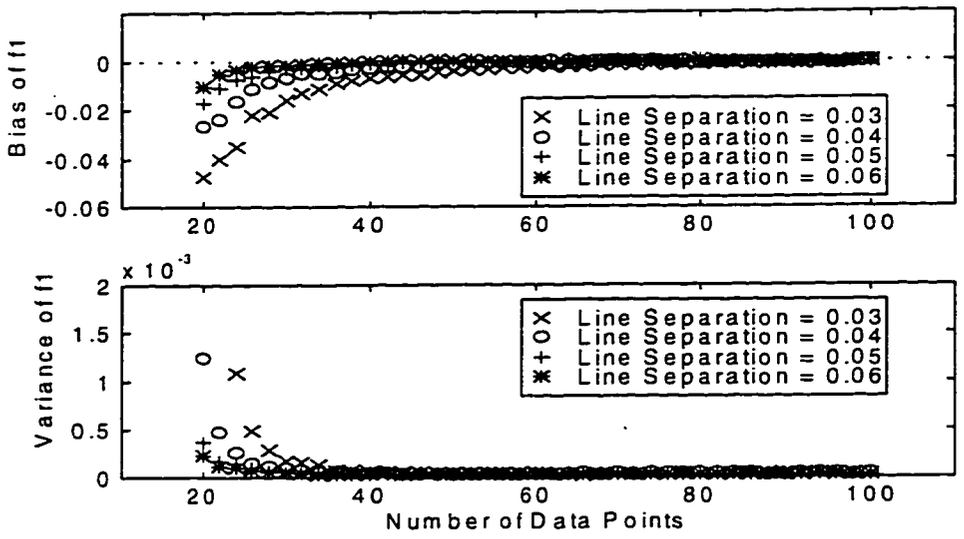

Figure 4.3.6g

The accuracy and precision of parameter f_1 as a function of the number of data points (N) and line separation (Δf), analyzed using LPSVD only. A cutoff of 10 was used and 500 simulations were analyzed for each N and Δf with a noise level of $\sigma = 50$.

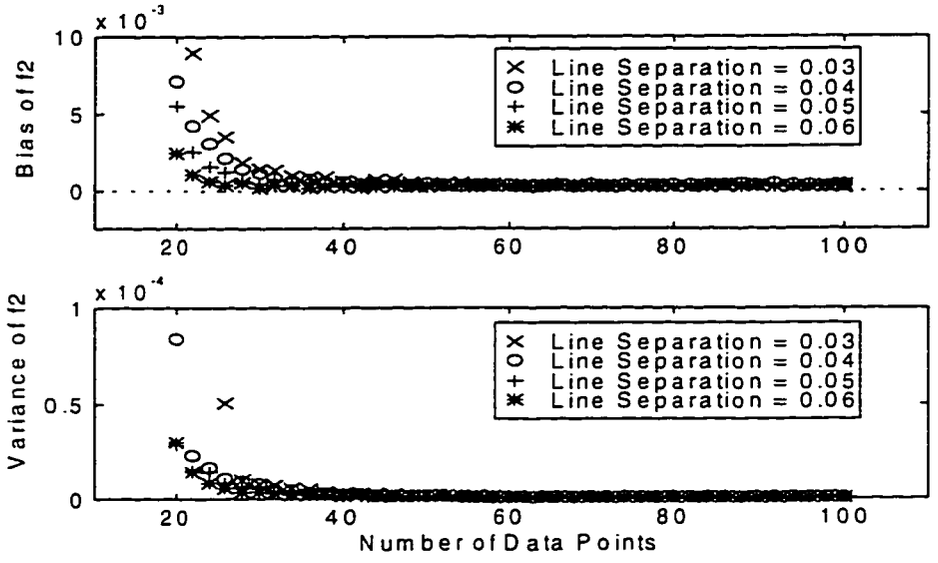

Figure 4.3.6h

The accuracy and precision of parameter f_2 as a function of the number of data points (N) and line separation (Δf), analyzed using LPSVD only. A cutoff of 10 was used and 500 simulations were analyzed for each N and Δf with a noise level of $\sigma = 50$.

4.4 Noise Line Identification

In this section the results of subsectioning to eliminate false lines is demonstrated. Here a true line is defined as one found with parameters within 4σ of their respective true values as calculated from the CR bounds of the analysis results. Unless otherwise noted 100 realizations at each noise level were generated from the simulation parameters defined in table 4.1, continuous regularization was used, N was set using equation 3.1.1 and the model order L was set to N/2. LPSVD failures are due to the initial LPSVD procedure missing true lines. Failures due to missing true lines after subsectioning are additional failures generated when the procedure eliminates a true line in the results. Failures where no noise lines eliminated are when the subsectioning procedure fails to remove any noise lines. Failures where some noise lines are eliminated are when the subsectioning procedure removes some but not all noise lines.

Figures 4.4.1a through 4.4.1c show the failure rate and the cause of the line fitting failure for each type of identification versus the noise level using the default parameters of table 4.1. Referencing figure 4.4.1a we see that real/imaginary subsectioning eliminates true lines in a very high percentage of cases especially at higher noise levels. Generally it was not able to differentiate between noise lines and true lines. In figure 4.4.1b we see that even/odd subsectioning has an increased failure rate at low noise levels mostly due to inclusion of noise lines in the final results. At higher noise levels its performance is comparable to that of the multiple acquisition algorithm and much superior to real/imaginary subsectioning. Refering to figure 4.4.1c we see that overall the

multiple acquisition subsectioning algorithm tends to perform best for the case used with even/odd giving similar results. Real/imaginary subsectioning has very poor performance relative to the other two and in most cases at higher noise levels will not recognize the true lines in the subsets. Therefore real/imaginary subsectioning will not be considered for further analysis. The main reason for all subsectioning procedures eliminating true lines is that the subsets generated from the full dataset will have reduced SNRs and will effectively have a failure rate equivalent to a much higher noise level.

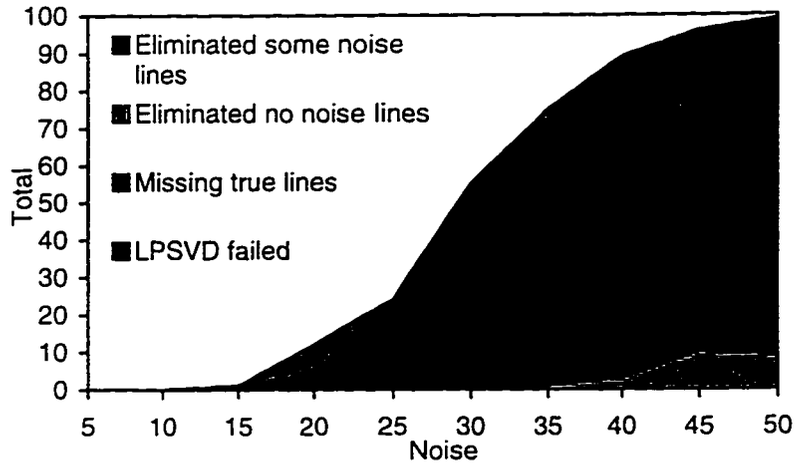

Figure 4.4.1a
The cause of failure as a function of the noise for real/imaginary subsectioning for a dataset length (N) of 50.

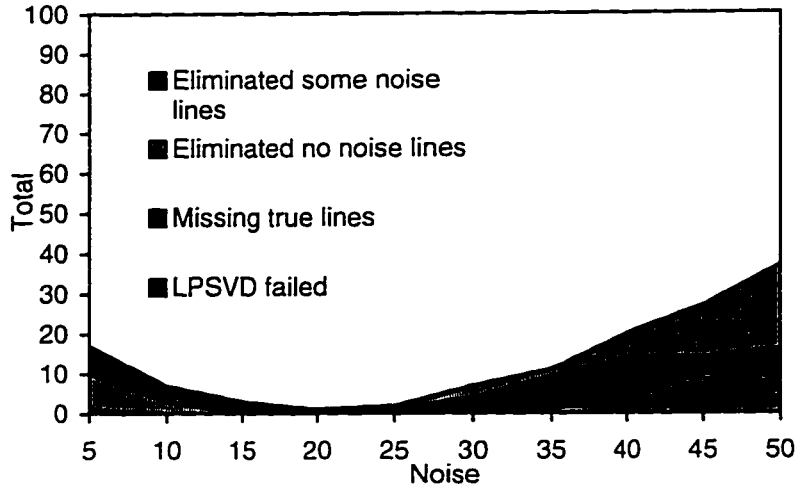

Figure 4.4.1b

The cause of failure as a function of the noise for even/odd subsectioning for a dataset length (N) of 50.

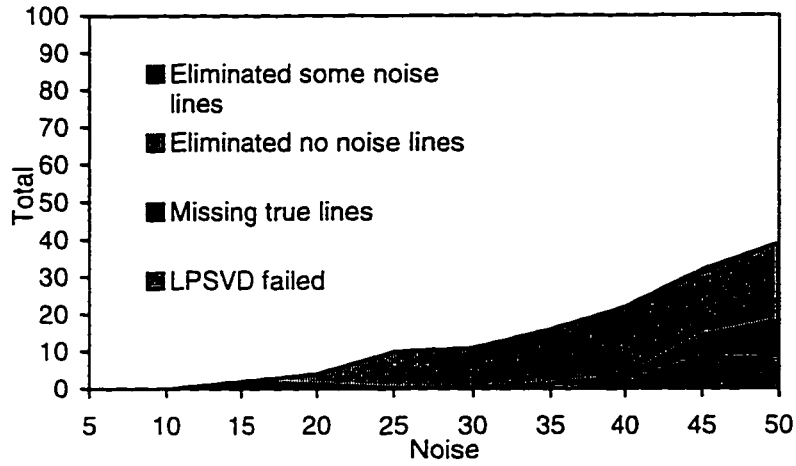

Figure 4.4.1c

The cause of failure as a function of the noise for multiple acquisition subsectioning for a dataset length (N) of 50.

Figures 4.4.2a through 4.4.2h show the failure rate and the cause of the line fitting failure for the multiple acquisition algorithm compared with the failure rate without a noise line identification algorithm for two decay rates and two line separations over a noise range of $\sigma = 5$ to 50. Comparing figures 4.4.2a and 4.4.2b we see that for the high

decay rate of α_2=0.10 and line separation Δf=0.06 multiple acquisition subsectioning is able to identify most noise lines at lower noise levels but generally does not identify them at higher nosie levels. Surprisingly, in figures 4.4.2c and 4.4.2d where the line separation is decreased to Δf=0.03 , we find that the multiple acquisition algorithm is able to identify most noise lines at all noise levels analyzed. Shifting our attention to figures 4.4.2e through 4.4.2h where the decay rate is reduced to α_2=0.05 we find that for both line separations analyzed the performance of the multiple acquisition algorithm is similar and performs best at lower noise levels. Overall there is significant improvement in the failure rate when using the multiple acquisition algorithm as opposed to not using a noise line identification algorithm, especially at the lower noise levels.

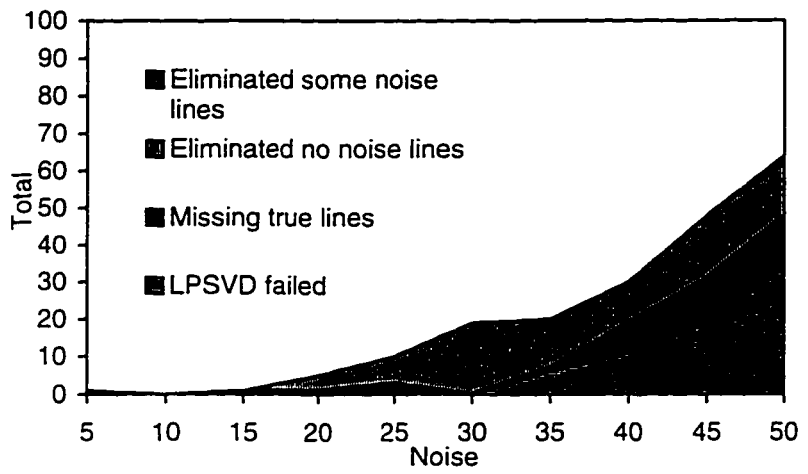

Figure 4.4.2a

The cause of failure as a function of the noise for multiple acquisition subsectioning for a decay rate of α_2 = 0.10 and a line separation of Δf = 0.06.

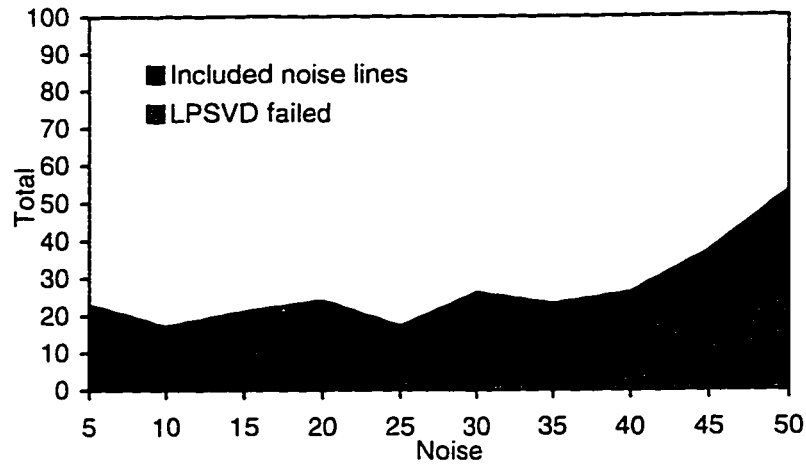

Figure 4.4.2b

The cause of failure as a function of the noise before subsectioning for a decay rate of $\alpha_2 = 0.10$ and a line separation of $\Delta f = 0.06$.

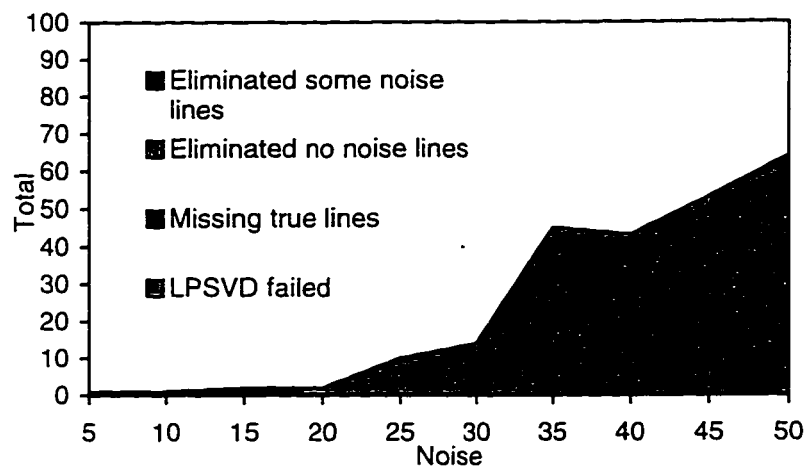

Figure 4.4.2c

The cause of failure as a function of the noise for multiple acquisition subsectioning for a decay rate of $\alpha_2 = 0.10$ and a line separation of $\Delta f = 0.03$.

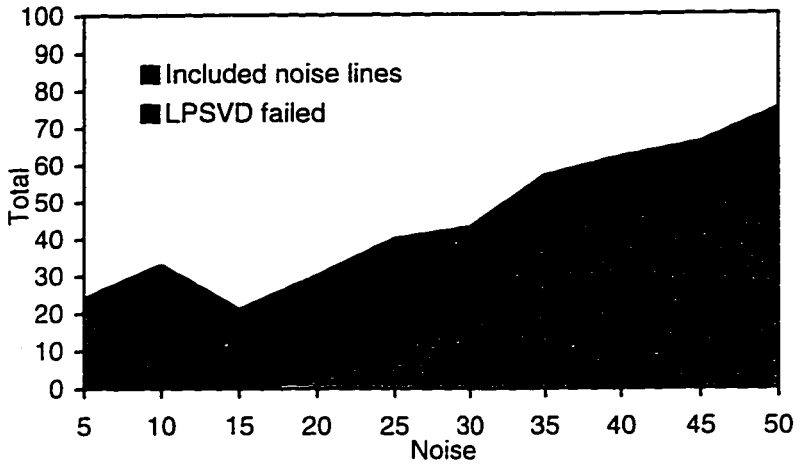

Figure 4.4.2d

The cause of failure as a function of the noise before subsectioning for a decay rate of $\alpha_2 = 0.10$ and a line separation of $\Delta f = 0.03$.

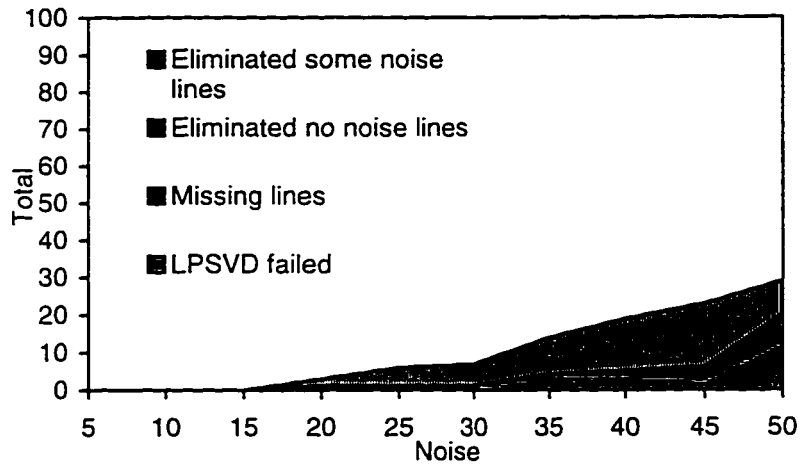

Figure 4.4.2e

The cause of failure as a function of the noise for multiple acquisition subsectioning for a decay rate of $\alpha_2 = 0.05$ and a line separation of $\Delta f = 0.06$.

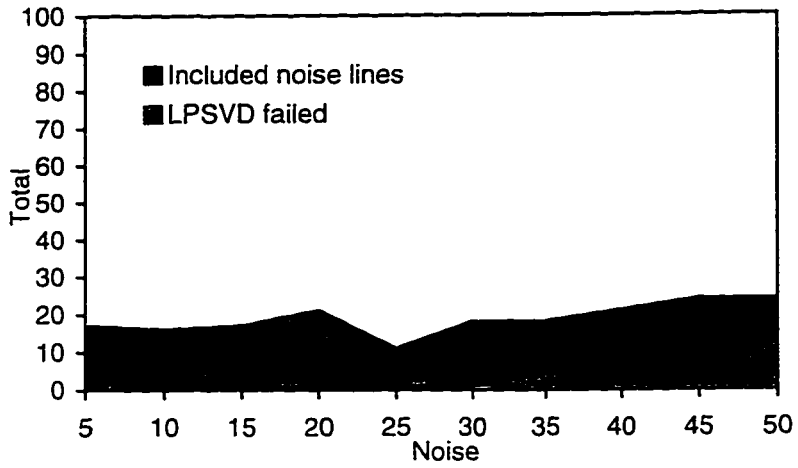

Figure 4.4.2f

The cause of failure as a function of the noise before subsectioning for a decay rate of $\alpha_2 = 0.05$ and a line separation of $\Delta f = 0.06$.

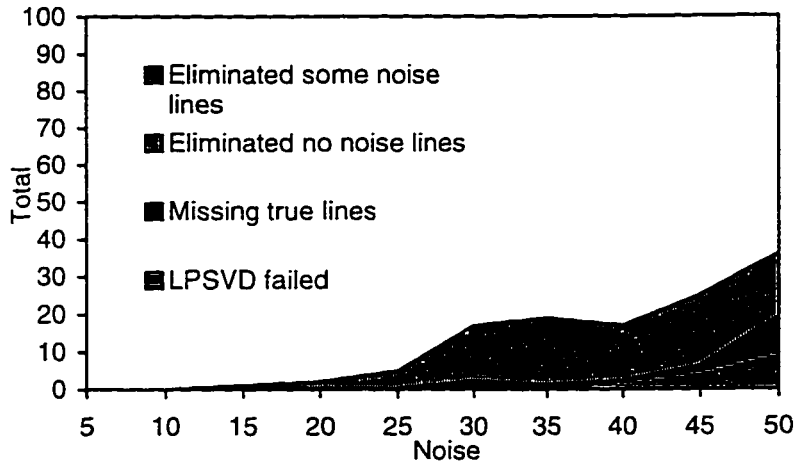

Figure 4.4.2g

The cause of failure as a function of the noise for multiple acquisition subsectioning for a decay rate of $\alpha_2 = 0.05$ and a line separation of $\Delta f = 0.03$.

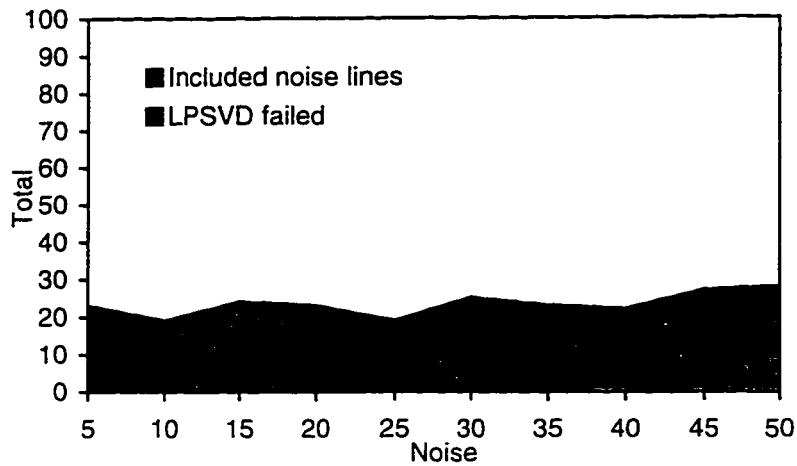

Figure 4.4.2h

The cause of failure as a function of the noise before subsectioning for a decay rate of $\alpha_2 = 0.05$ and a line separation of $\Delta f = 0.03$.

Figures 4.4.3a through 4.4.3h show the failure rate and the cause of the line fitting failure for the even/odd subsectioning algorithm compared with the failure rate without a noise line identification algorithm for two decay rates and two line separations over a noise range of $\sigma = 5$ to 50. Comparing figures 4.4.3a and 4.4.3b we see that for the high decay rate of α_2=0.10 and line separation Δf=0.06 even/odd subsectioning is able to identify most noise lines at lower noise levels but generally does not identify them at higher nosie levels. In figures 4.4.3c and 4.4.3d where the line separation is decreased to Δf=0.03 , we find that the even/odd subsectioning algorithm is also not able to identify most noise lines at high noise levels and its performance at lower levels is not quite as good as that of the multiple acquisition subsectioning procedure. Shifting our attention to figures 4.4.3e through 4.4.3h where the decay rate is reduced to α_2=0.05 we find that for both line separations analyzed the performance of the even/odd subsectionign algorithm is similar and performs best at lower noise levels. Of note is the increase in the failure

rate at very low noise levels as seen previously in figure 4.4.1b. Overall there is significant improvement in the failure rate when using the even/odd subsectioning algorithm as opposed to not using a noise line identification algorithm, especially at the lower noise levels. Unlike the multiple acquisition algorithm, even/odd subsectioning has a fairly high failure rate at low noise levels mostly due to extra lines in the results but does eliminate true lines in the results in some cases.

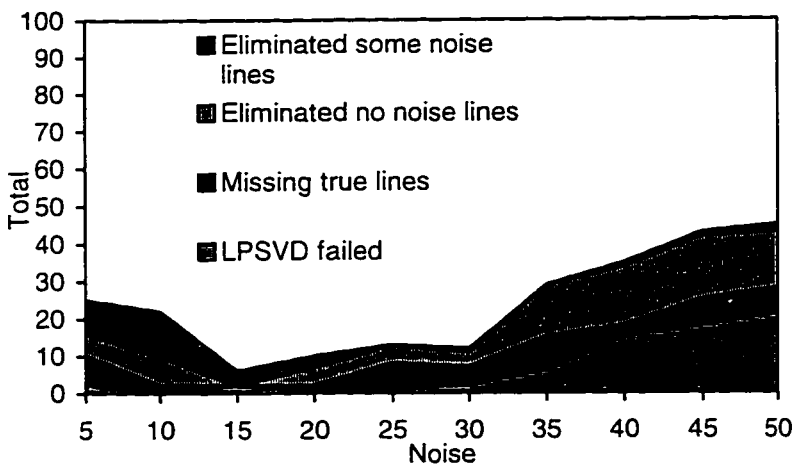

Figure 4.4.3a

The cause of failure as a function of the noise for even/odd subsectioning for a decay rate of $\alpha_2 = 0.10$ and a line separation of $\Delta f = 0.06$.

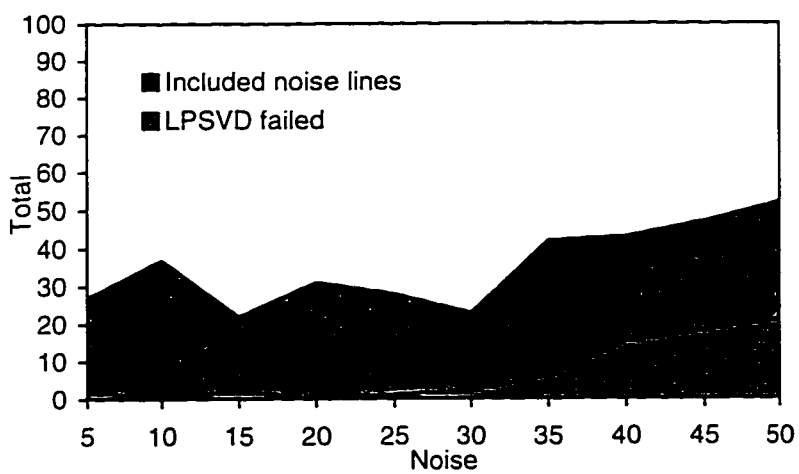

Figure 4.4.3b

The cause of failure as a function of the noise before subsectioning for a decay rate of $\alpha_2 = 0.10$ and a line separation of $\Delta f = 0.06$.

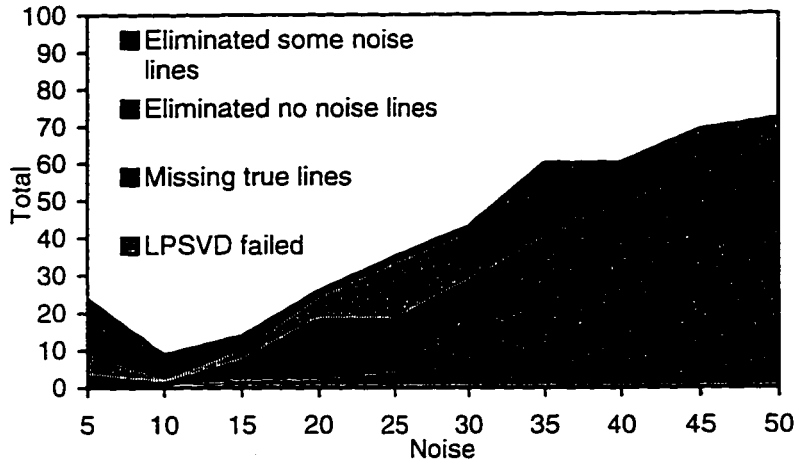

Figure 4.4.3c

The cause of failure as a function of the noise for even/odd subsectioning for a decay rate of $\alpha_2 = 0.10$ and a line separation of $\Delta f = 0.03$.

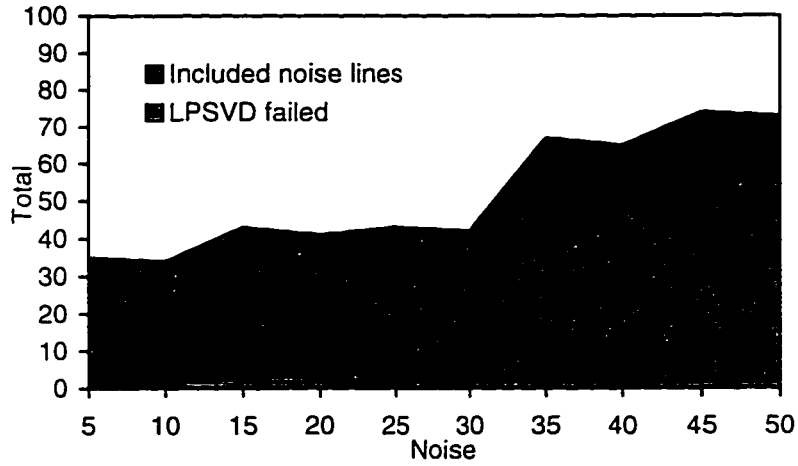

Figure 4.4.3d

The cause of failure as a function of the noise before subsectioning for a decay rate of $\alpha_2 = 0.10$ and a line separation of $\Delta f = 0.03$.

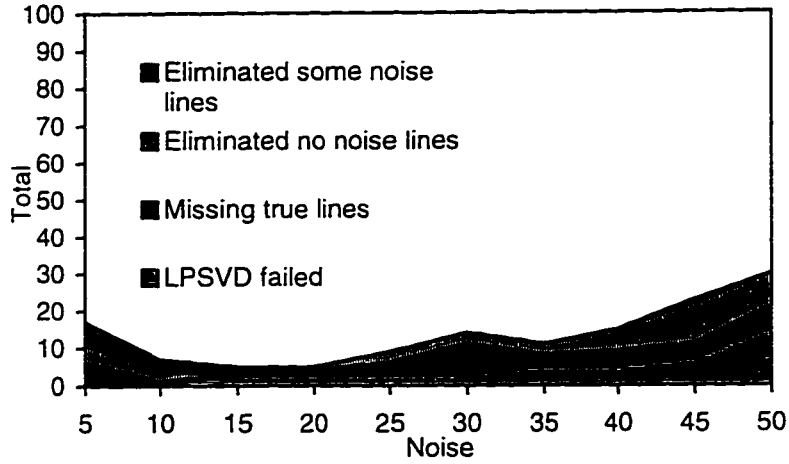

Figure 4.4.3e

The cause of failure as a function of the noise for even/odd subsectioning for a decay rate of $\alpha_2 = 0.05$ and a line separation of $\Delta f = 0.06$.

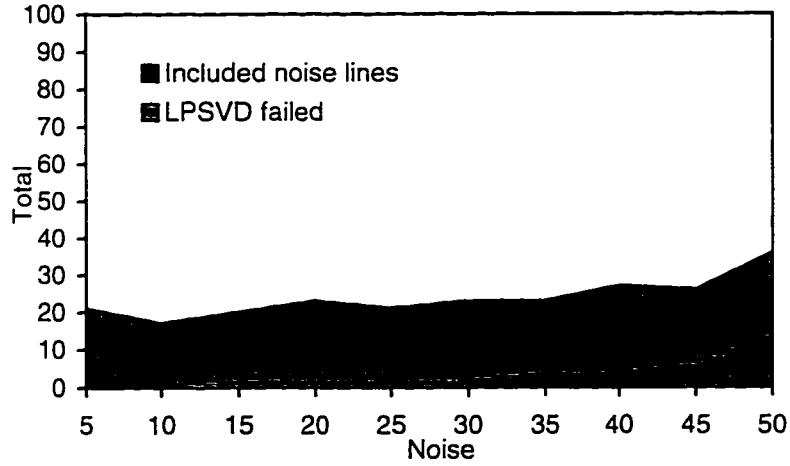

Figure 4.4.3f

The cause of failure as a function of the noise before subsectioning for a decay rate of $\alpha_2 = 0.05$ and a line separation of $\Delta f = 0.06$.

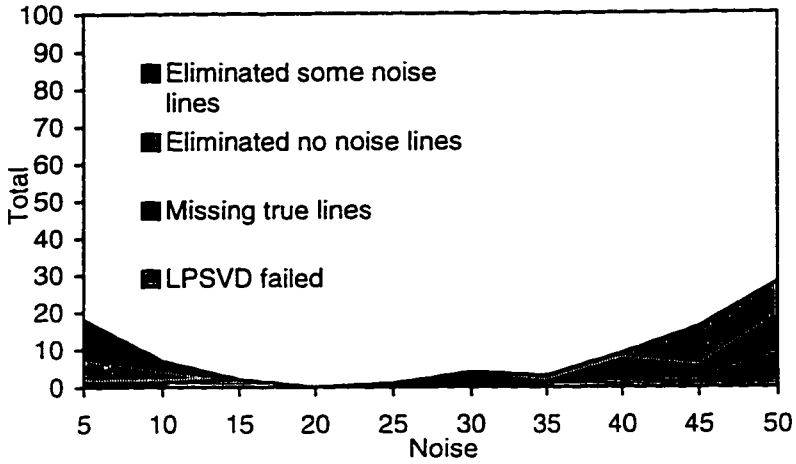

Figure 4.4.3g

The cause of failure as a function of the noise for even/odd subsectioning for a decay rate of $\alpha_2 = 0.05$ and a line separation of $\Delta f = 0.03$.

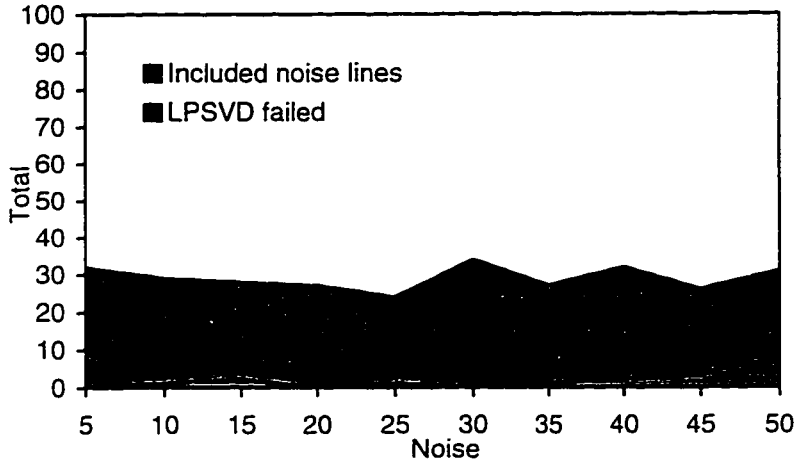

Figure 4.4.3h

The cause of failure as a function of the noise before subsectioning for a decay rate of $\alpha_2 = 0.05$ and a line separation of $\Delta f = 0.03$.

4.5 A Totally Automated Algorithm

Here we integrate the results from sections 4.1, 4.2, 4.3, and 4.4 to produce a single algorithm which will completely automate the selection of the parameters N, L, and cutoff, as well as reduce the number of false lines in the spectra.

To determine N we will first analyze the FID using its first 256 points and continuous regularization. The FID is regenerated from the resulting parameters and subtracted from the original FID leaving mostly noise. An estimate of the σ of the noise is calculated from the difference. The optimal value of N is then calculated iteratively. First, the FID is analyzed using N = 128. The resulting values of α and f are used to generate a new N using equation [3.1.1]. α_{min} and Δf_{min} are estimated using only the closest lines whose amplitudes are larger than the estimated noise σ to reduce the effect of noise lines on the calculated value of N. L is set to N/2. Continuous regularization is used for the noise reduction step. The above procedure is repeated a maximum of ten times to obtain the best N. Even/odd subsectioning was used for the noise line elimination step. It was chosen over multiple acquisition due to the fact that it requires no change in how data is acquired and therefore allows analysis of existing data such as that analyzed in section 4.7. In situations where it is known that the data is to be analyzed with the totally automated algorithm, the multiple acquisition subsectioning procedure would be the method of choice. Once the line parameter estimates are determined, the NMLE procedure is applied to give optimal bias and variance to the results.

Figures 4.5.1a through 4.5.1h show the performance of the totally automated algorithm against analysis using normal LPSVD with N = 150 and a cutoff = 2 for differing decay rates and line separations. In figures 4.5.1a through 4.5.1d we see that the automated algorithm outperforms simple LPSVD in terms of failure rate for the faster decay rate but does not perform as well for the slower decay rate of figures 4.5.1e through 4.5.1h. As well we see an increased error rate at lower noise levels. A possible explanation is that the number of data points chosen for the simple LPSVD procedure is closer to the optimal for $\alpha_2 = 0.05$ than $\alpha_2 = 0.10$. We also see that the automated algorithm is outperformed by simple LPSVD for noise levels above 30 for the smaller line separations. Again, it is likely that the number of data points chosen for LPSVD (N = 150) is closer to the optimal for $\Delta f = 0.03$ than 0.06 and, more importantly, the automatic procedure for determining N does not properly select N. An improperly selected N also explains why the results in this section do not match the results of section 4.4 for the even/odd subsectioning. Section 4.4 uses the ideal N determined from the known simulation parameters. The difficulty in selecting N automatically arises due to the fact that the line spacings and decay rates contained in the signal are unknown and can only be estimated by first analyzing the signal. Unfortunately, to properly analyze the signal we also need to know the line spacings and decay rates. The iterative procedure is an attempt to determine these parameters but is affected by noise lines and missed lines in the intermediate results perturbing the calculation of N for the next iteration. A more robust algorithm for determining the optimal N is necessary. Of note is the fact that the automatic algorithm rarely includes noise lines in the results. The cutoff of 2 for LPSVD

prevents noise lines from appearing in the results of the nonautomated algorithm for the two line case analyzed.

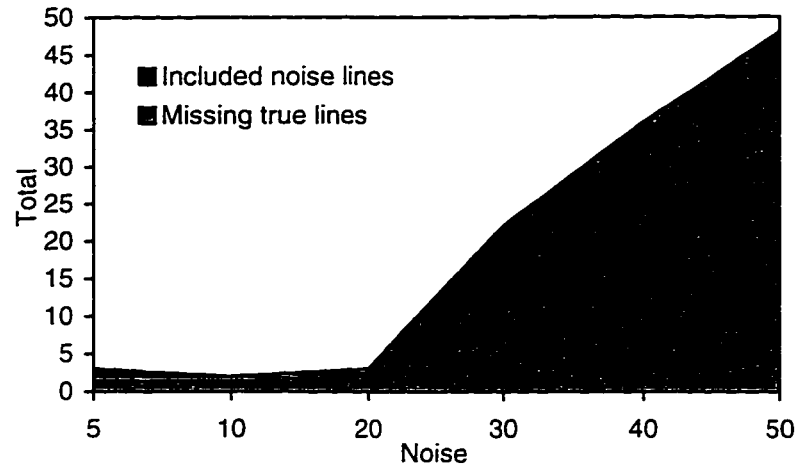

Figure 4.5.1a

The cause of failure as a function of the noise for the totally automated algorithm for a decay rate of α_2 = 0.10 and a line separation of Δf = 0.06. Fifty simulations were run for each noise level.

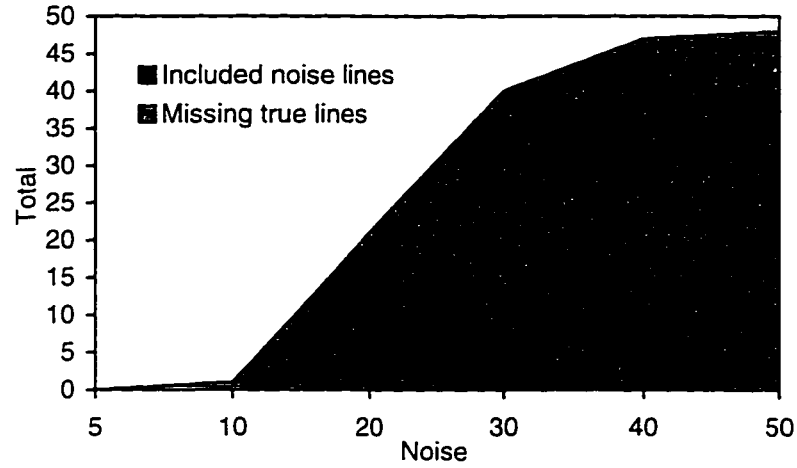

Figure 4.5.1b

The cause of failure as a function of the noise for normal LPSVD for a decay rate of α_2 = 0.10 and a line separation of Δf = 0.06. Fifty simulations were run for each noise level. with the dataset length set to N = 150.

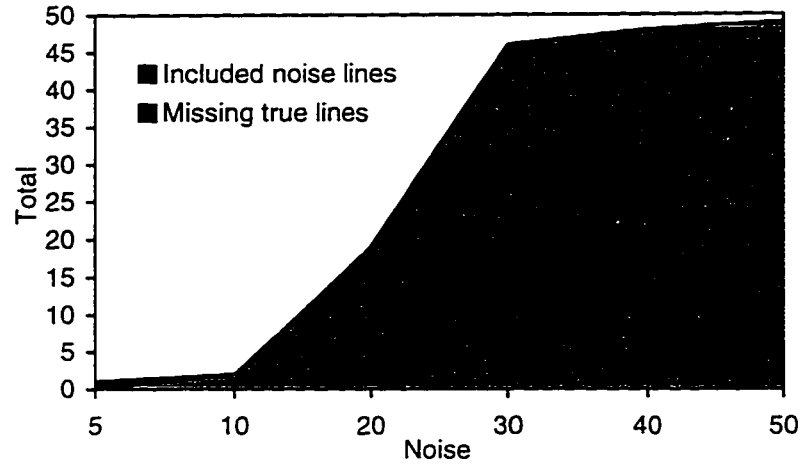

Figure 4.5.1c

The cause of failure as a function of the noise for the totally automated algorithm for a decay rate of α_2 = 0.10 and a line separation of $\Delta f = 0.03$. Fifty simulations were run for each noise level.

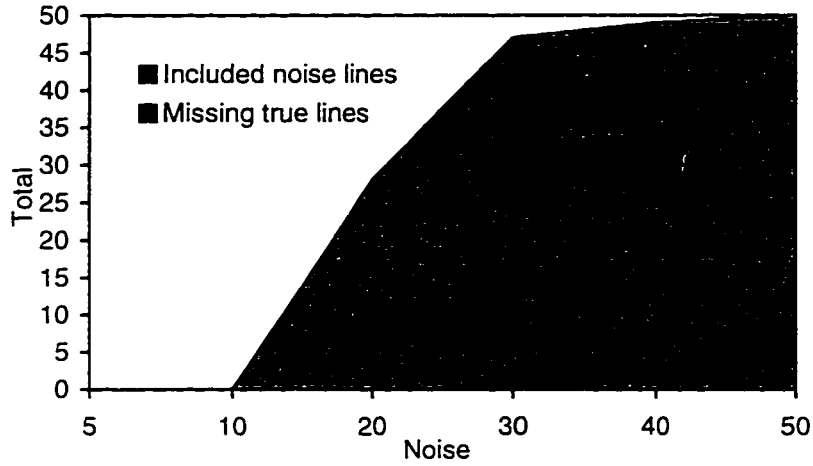

Figure 4.5.1d

The cause of failure as a function of the noise for normal LPSVD for a decay rate of $\alpha_2 = 0.10$ and a line separation of $\Delta f = 0.03$. Fifty simulations were run for each noise level, with the dataset length set to N = 150.

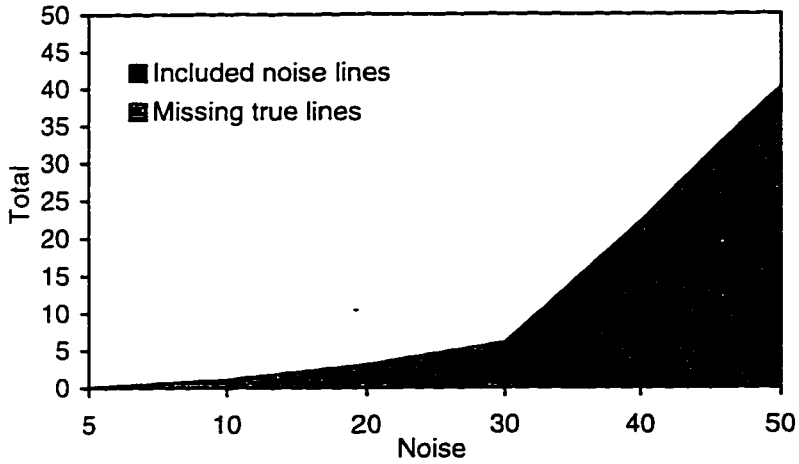

Figure 4.5.1e

The cause of failure as a function of the noise for the totally automated algorithm for a decay rate of α_2 = 0.05 and a line separation of $\Delta f = 0.06$. Fifty simulations were run for each noise level.

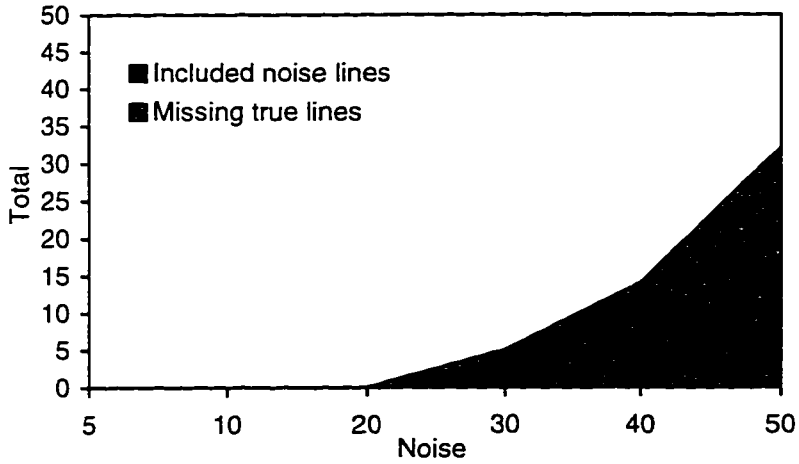

Figure 4.5.1f

The cause of failure as a function of the noise for normal LPSVD for a decay rate of $\alpha_2 = 0.05$ and a line separation of $\Delta f = 0.06$. Fifty simulations were run for each noise level, with the dataset length set to N = 150.

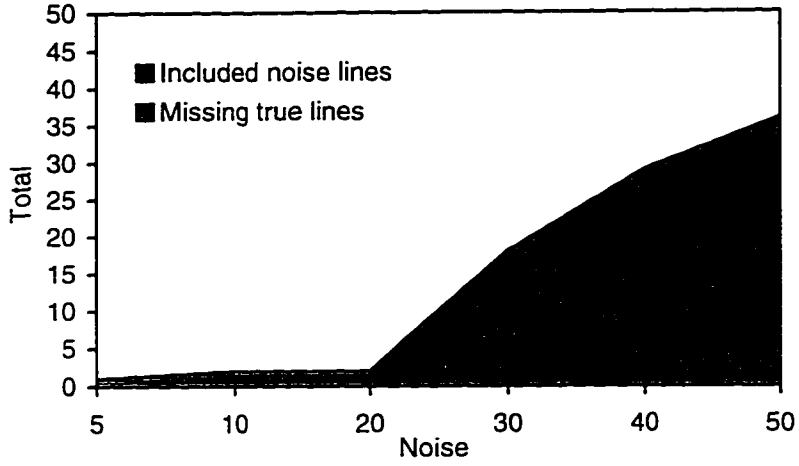

Figure 4.5.1g

The cause of failure as a function of the noise for the totally automated algorithm for a decay rate of α_2 = 0.05 and a line separation of $\Delta f = 0.03$. Fifty simulations were run for each noise level.

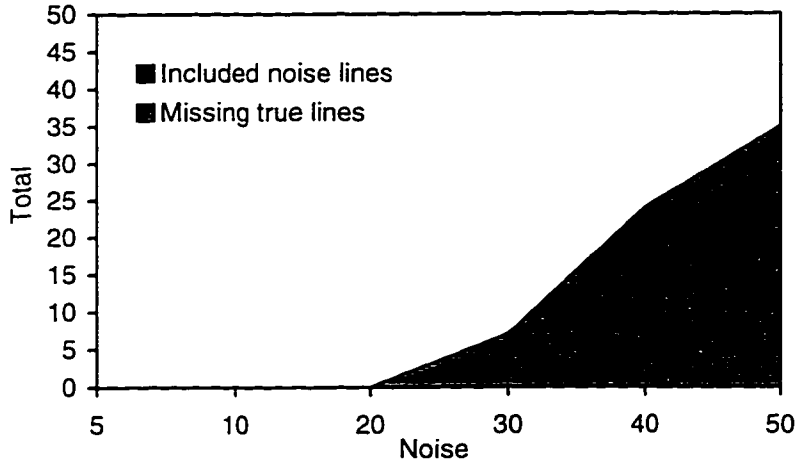

Figure 4.5.1h

The cause of failure as a function of the noise for normal LPSVD for a decay rate of $\alpha_2 = 0.05$ and a line separation of $\Delta f = 0.03$. Fifty simulations were run for each noise level, with the dataset length set to N = 150.

4.6 Simulated Muscle Phosphorus Spectra

Here an FID of a six component ^{31}P spectrum is simulated and analyzed using the automated algorithm. Since the main parameter of interest for this specific signal is the

Pi/PCr ratio, this is calculated for the successful fits and compared against the true value for different ratios and noise values. The simulation parameters were taken from the analysis of an FID acquired *in-vivo* from human calf muscle. Noise levels of $\sigma = 5$ and 10 were added to the simulations and were chosen by calculation of the actual noise levels present during a typical NMR measurement of human calf muscle. In terms of the amplitude of the ATP-β line, a noise level of $\sigma = 10$ correlates to a noise level of $\sigma = 70$ in the two line simulations using table 4.1. The ranges of P_i and PCr for the simulation were also chosen from the ranges that occurred in the same experiment on human calf muscle. The parameter values are summarized in table 4.2.

	Amplitude (A)	Phase Angle (ϕ)	Decay Rate (α)	Frequency (f)
Line 1 (ATP-β)	14.0645	0.9919	0.0419	-0.4111
Line 2 (ATP-α)	29.7062	-0.4286	0.0360	-0.2235
Line 3 (ATP-γ)	19.9034	-0.1793	0.0323	-0.1197
Line 4 (PCr)	72.0 to 55.0	-0.3521	0.0107	-0.0681
Line 5 (PDE)	12.5567	-0.6888	0.0309	-0.0045
Line 6 (P_i)	10.8 to 24.75	0.0274	0.0178	0.0320

Table 4.2

The parameters of the reference FID used to generate the simulations in section 4.6. Note that the P_i and PCr lines were simultaneously varied to produce a P_i/PCr ratio of 0.15 to 0.45.

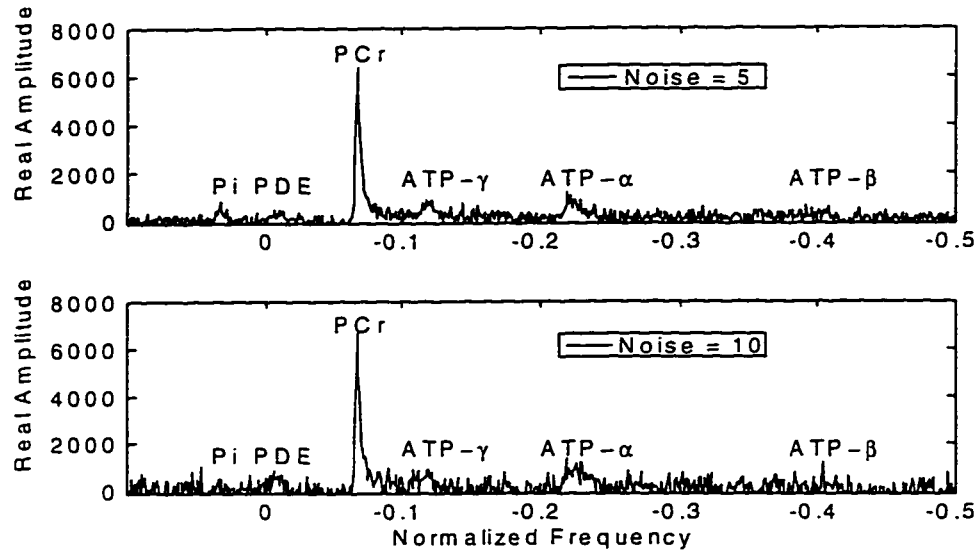

Figure 4.6.1

The frequency domain equivalent of the simulated FID generated from table 4.2 with noise levels of $\sigma = 5$ and 10 for a P_i/PCr ratio of 0.15.

Ten simulations were generated for each noise level and P_i/PCr ratio, and the automated algorithm of section 4.5 was applied. As the automated algorithm of section 4.5 uses even/odd subsectioning and the frequency range of the lines in table 4.2 is outside of the region $-0.25 < f < 0.25$, it was necessary to interpolate the simulated FID's to reduce each frequency by a factor of two before processing to keep the simulation as realistic as possible. At a noise level of $\sigma = 5$ all lines were found in all simulations. Table 4.3 lists the number of returned fits which failed to identify specific lines for the case of $\sigma = 10$. As expected, those lines with amplitudes close to the noise level such as P_i for small P_i/PCr ratios and the ATP-β peak were missed most frequently. Figures 4.6.2a through 4.6.2f show the resulting bias and variance of the amplitude of each line compared to the original simulation values after processing with the automated algorithm. For a noise level of $\sigma = 5$ the bias of the amplitude of each line is statistically equal to

zero. For a noise level of $\sigma = 10$, however, there is a negative bias for some of the line amplitudes measured. This may be due to the higher number of noise lines present in the results even after the subsectioning procedure. Figure 4.6.3 shows the resulting P_i/PCr ratio calculated from the individual P_i and PCr results. In general, the amplitude parameters of all six lines and the P_i/PCr ratio are reasonable estimates of the original parameters over the P_i/PCr ratio used. It is clear that the automated algorithm is useful for the analysis of multiple line spectra such as the ones simulated here.

P_i/PCr	0.15	0.20	0.25	0.30	0.35	0.40	0.45
ATP-β	1	2	4	1	3	4	3
ATP-α	0	0	0	0	0	0	0
ATP-γ	1	1	0	0	1	0	0
PCr	0	0	0	0	0	0	0
PDE	2	5	1	2	3	1	2
P_i	3	1	0	0	0	0	0

Table 4.3

Line identification failure for each of the six lines contained in the simulations generated from table 4.2 at a noise level of $\sigma = 10$. Ten simulations were generated at each Pi/PCr ratio and the automated algorithm of section 4.5 applied. At a noise level of $\sigma = 5$ all lines were found in all simulations.

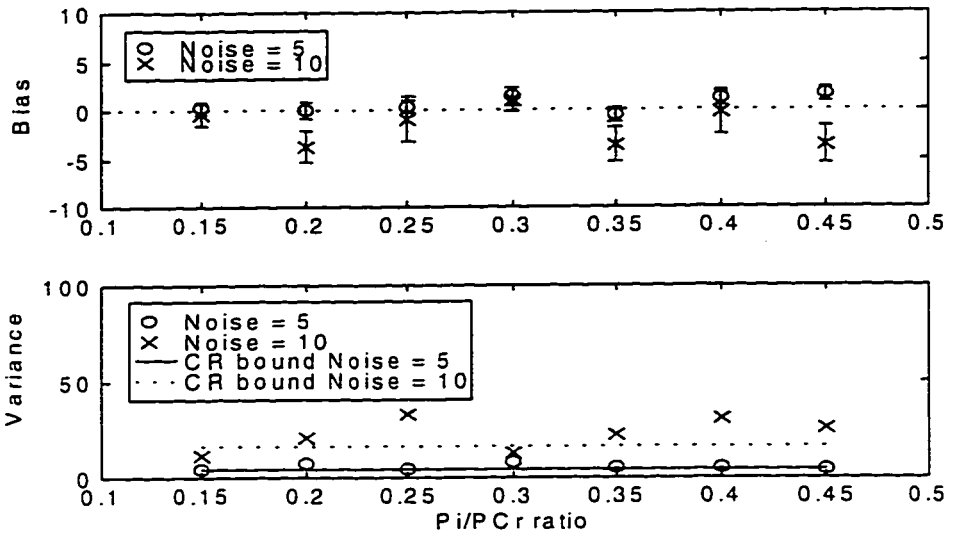

Figure 4.6.2a

The accuracy and precision of the amplitude of the ATP-β peak as a function of the P_i/PCr ratio analyzed using the totally automated algorithm of section 4.5. Ten simulations were analyzed for each P_i/PCr ratio and noise level.

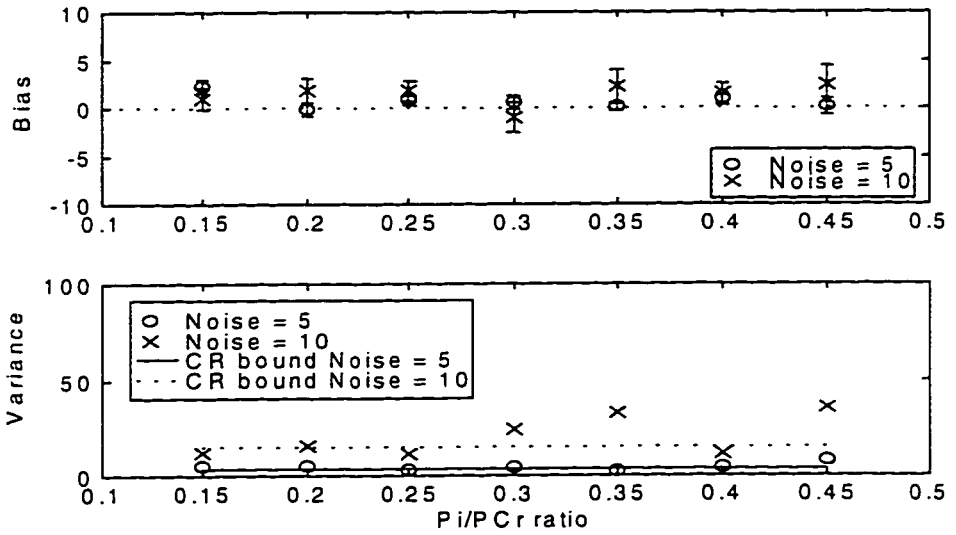

Figure 4.6.2b

The accuracy and precision of the amplitude of the ATP-α peak as a function of the P_i/PCr ratio analyzed using the totally automated algorithm of section 4.5. Ten simulations were analyzed for each P_i/PCr ratio and noise level.

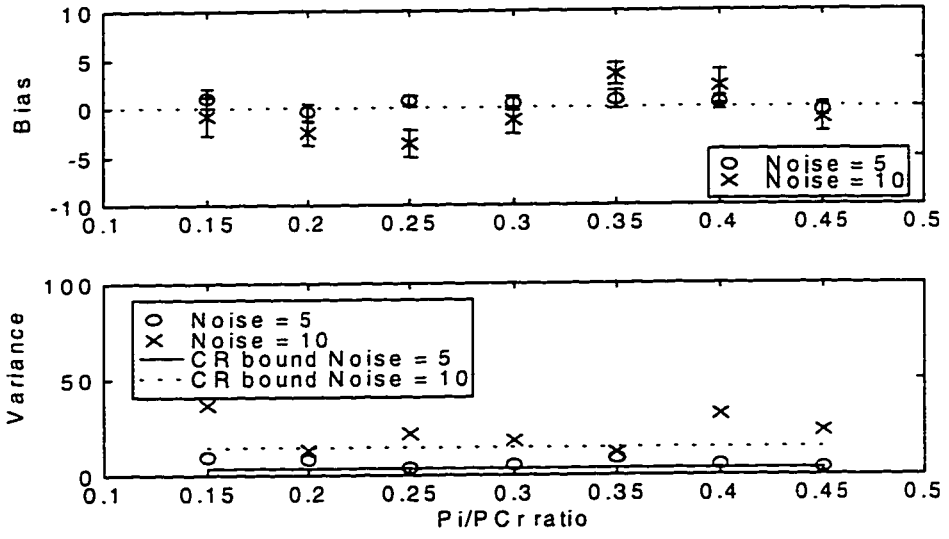

Figure 4.6.2c

The accuracy and precision of the amplitude of the ATP-γ peak as a function of the P_i/PCr ratio analyzed using the totally automated algorithm of section 4.5. Ten simulations were analyzed for each P_i/PCr ratio and noise level.

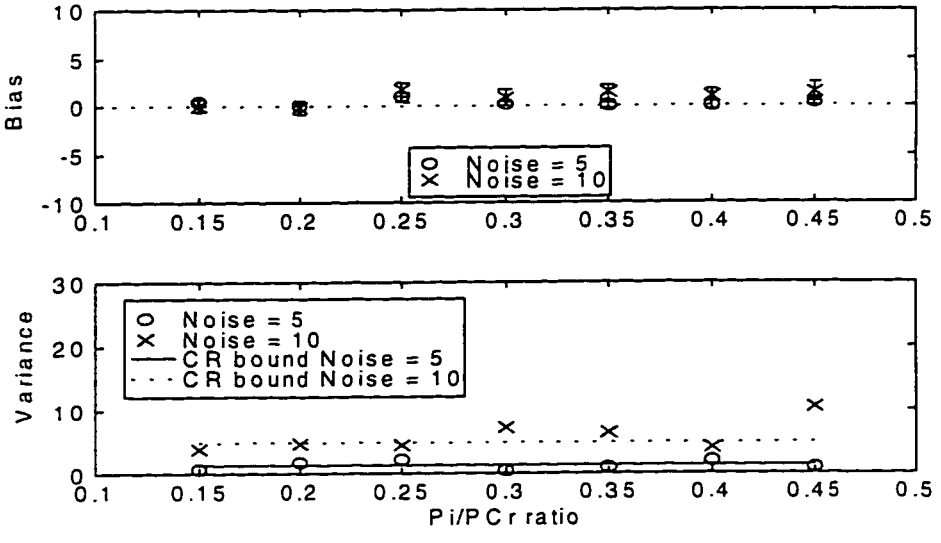

Figure 4.6.2d

The accuracy and precision of the amplitude of the PCr peak as a function of the P_i/PCr ratio analyzed using the totally automated algorithm of section 4.5. Ten simulations were analyzed for each P_i/PCr ratio and noise level.

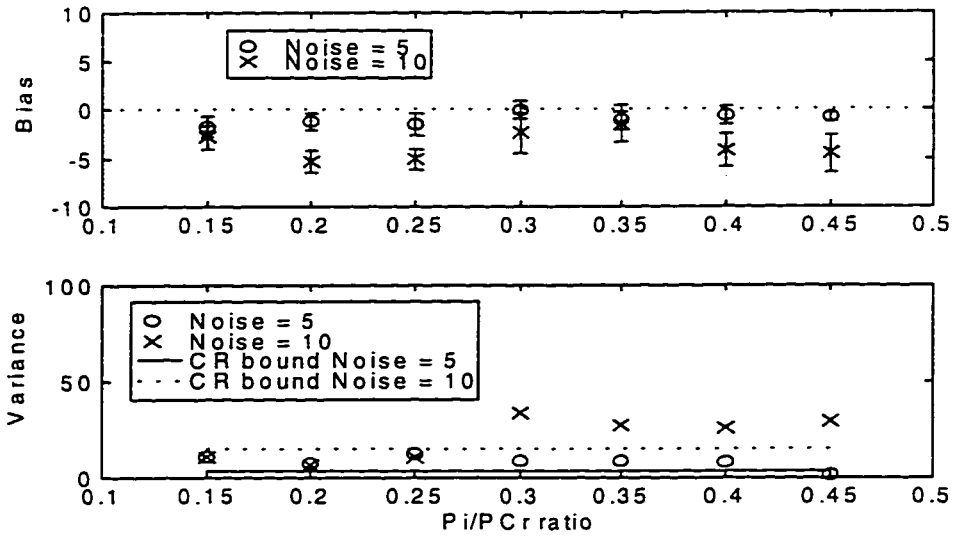

Figure 4.6.2e

The accuracy and precision of the amplitude of the PDE peak as a function of the P_i/PCr ratio analyzed using the totally automated algorithm of section 4.5. Ten simulations were analyzed for each P_i/PCr ratio and noise level.

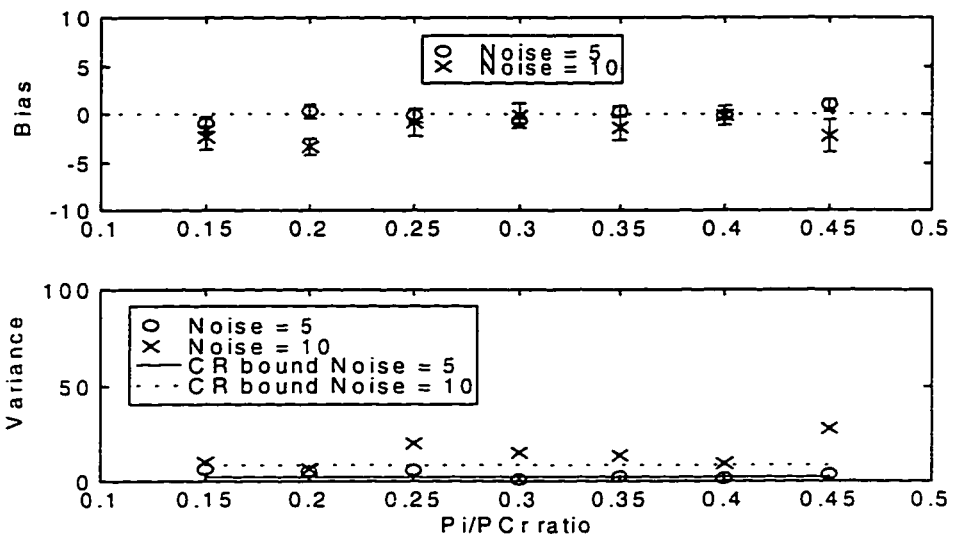

Figure 4.6.2f

The accuracy and precision of the amplitude of the P_i peak as a function of the P_i/PCr ratio analyzed using the totally automated algorithm of section 4.5. Ten simulations were analyzed for each P_i/PCr ratio and noise level.

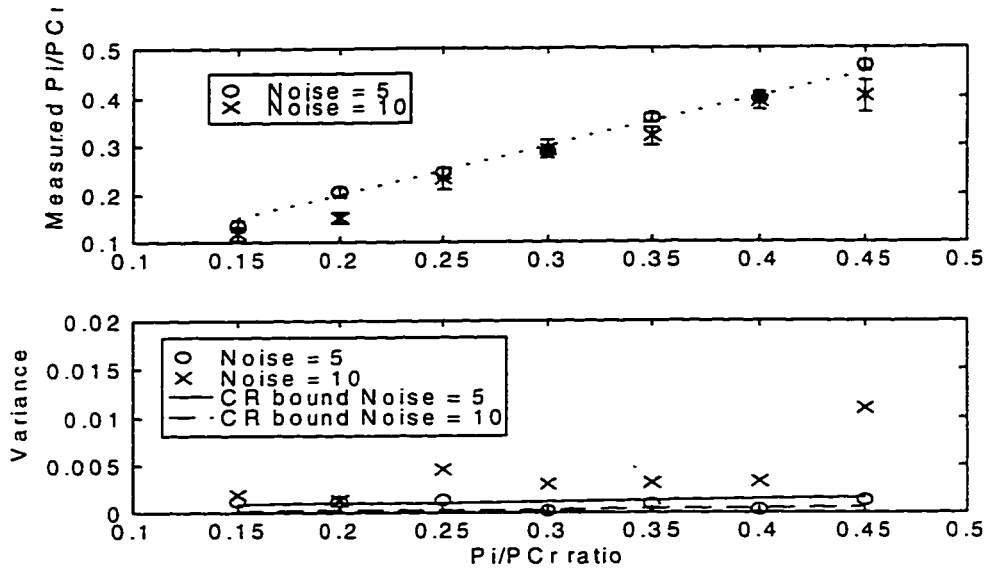

Figure 4.6.3

The accuracy and precision of the amplitude of the measured P_i/PCr ratio as a function of the true P_i/PCr ratio analyzed using the totally automated algorithm of section 4.5. Ten simulations were analyzed for each P_i/PCr ratio and noise level.

4.7 Actual Muscle Phosphorous Spectra

Here we apply the automated analysis algorithm of section 4.5 to actual data taken using a 3.0-Tesla NMR machine. The data were taken as part of an experimental protocol which measures the P_i/PCr ratio in human calf muscle during repeated rest, work, and recovery cycles. Ninety-three FID's were acquired during the course of the experiment which repeated the cycle 3 times and were analyzed in exactly the same manner as the simulated FID's in section 4.6.

Figure 4.7.1 shows a typical FID from the experimental data and its frequency domain equivalent showing the six main lines in the spectrum and the noise level present. Figures 4.7.2 and 4.7.3 show the P_i/PCr ratio and the pH calculated directly from the analysis results. The P_i and PCr peaks were identified in each of the resulting parameter

sets for all ninety-three acquisitions and the ratio calculated. The divisions of the protocol cycles are labeled with R0, R1, and R2 for a rest period, W1, W2, and W3 for a work period, and Z1, Z2, and Z3 for a recovery period; the resulting changes in the P_i/PCr ratio and pH in each region is clear. The automatic algorithm of section 4.5 can give useful results when used to analyze real data of this nature and does not require any input from the spectroscopist.

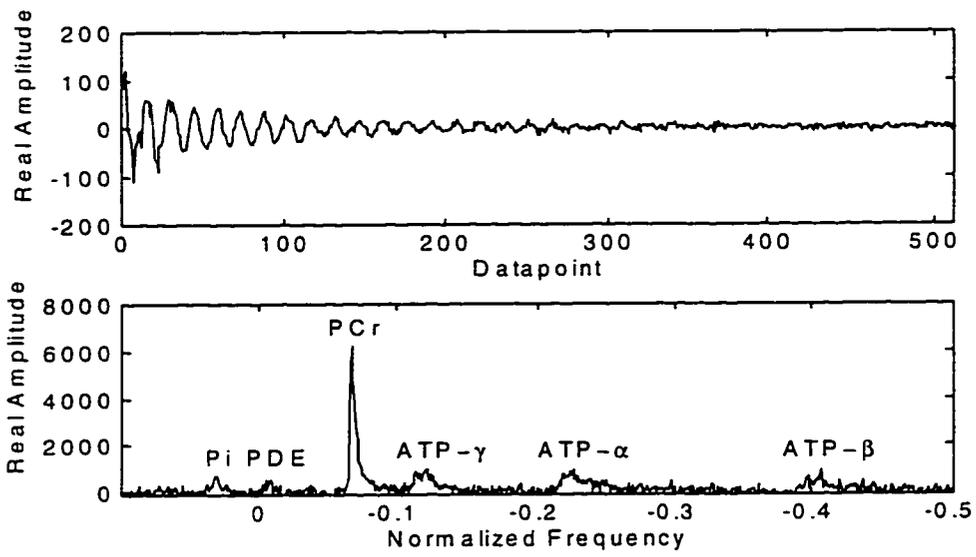

Figure 4.7.1

An example of a real ^{31}P FID acquired from human calf muscle in the NMR experiment FI052795 and its frequency domain equivalent showing the major phosphorous lines.

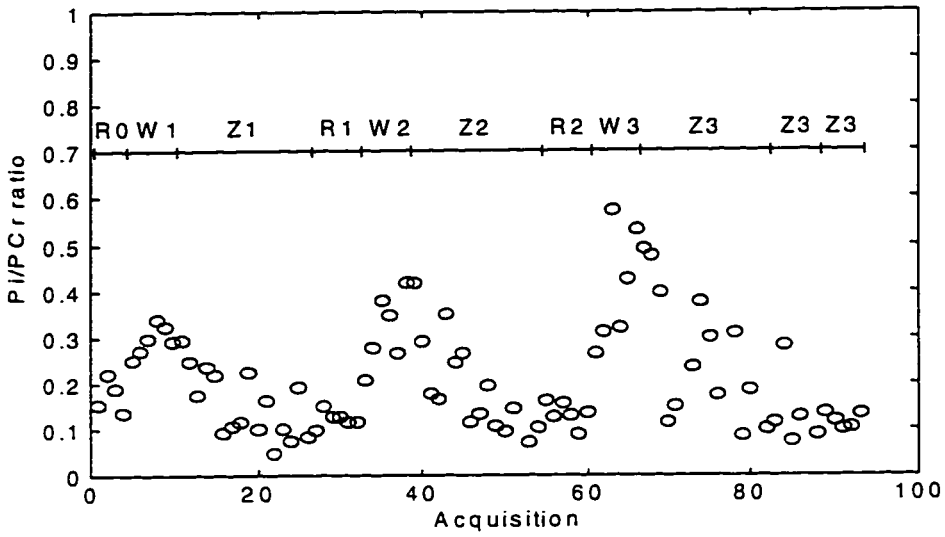

Figure 4.7.2

The P_i/PCr ratio calculated from the analysis of 93 acquisitions from the experiment FI052795 identifying the different regions of the experimental protocol, rest (RX), work (WX),and recovery (ZX) and the change over time of the ratio.

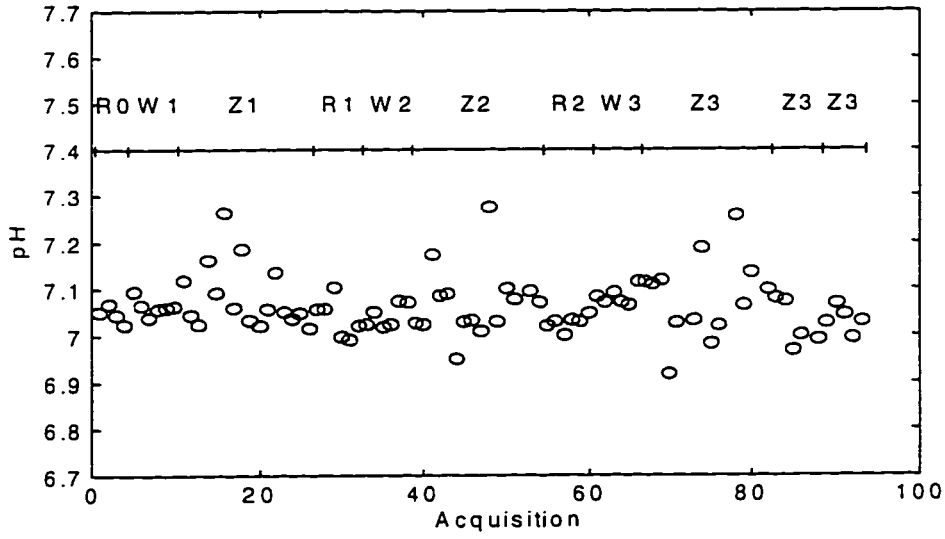

Figure 4.7.3

The pH calculated from the analysis of 93 acquisitions from the experiment FI052795 identifying the different regions of the experimental protocol, rest (RX), work (WX), and recovery (ZX) and the change over time of the pH.

5.0 Conclusions

Previously, Ho [12] proposed a technique that integrated LPSVD with NMLE to produce an algorithm which generated parameter estimates with zero bias and variances equal to their Cramer-Rao bounds while requiring no initial estimates to be supplied. The algorithm was an improvement over conventional frequency domain techniques which required experienced operator intervention. Although not requiring a priori knowledge of the acquired spectrum, Ho's method did require setup parameters for the LPSVD procedure such as the number of datapoints to use in the analysis, the model order, and a cutoff for the SVD singular value matrix. Ho showed that the setup parameters for the LPSVD procedure affected the accuracy and precision of the intermediate results which would be passed to the NMLE procedure. The accuracy and precision of the entire algorithm was generally dependent on the NMLE procedure. All that was necessary was that the LPSVD procedure generate reasonable intermediate results. As such, the setup parameters chosen for LPSVD did not seem to be extremely critical.

We found through simulation that even though the accuracy and precision of the LPSVD estimates was not extremely sensitive to the setup parameters, the probability of a fitting failure was. In the case of the setup parameter N needed by LPSVD, we found an extremely high sensitivity.

One of the main goals of this thesis was to develop a procedure which required absolutely no input from the user in terms of setup parameters or initial guesses. There

were three parameters which could change depending on the FID input to the algorithm: the SVD cutoff or regularization parameter, the model order, and the number of datapoints to use in the analysis.

In terms of the SVD cutoff or regularization parameter, two automatic procedures were evaluated against the original SVD cutoff of Kumaresan and Tufts [5, 6] which we called manual regularization in this thesis. The first automatic algorithm, discrete regularization, was developed here as an automatic method of selecting a discrete SVD cutoff value based on the noise. Its performance was equivalent to manual regularization with a cutoff value of two in terms of failure to fit a basic-two line simulation (see figure 4.1.4). Its biggest drawback was that it tended to miss lines when it failed. The second, continuous regularization, was a procedure proposed by Kolbel and Schafer [10] which relied on direct modification of the singular values. Its performance was equivalent to manual regularization with a cutoff of 10 in terms of failure to fit. Unlike discrete regularization, it tended to include noise related lines in the results. Continuous regularization was chosen as the method of choice for selection of the SVD cutoff or regularization parameter without user intervention.

Model order was the second setup parameter which was required to be optimized for the LPSVD procedure. Through extensive simulation looking at both the accuracy and precision and the failure rate for different model orders, number of datapoints, and noise levels for a two line-simulation, it was found that a broad range of model orders ($0.4N<L<0.7N$) existed where the bias and variance, and failure rate were minimized (see

figures 4.2.1 and 4.2.2). Hence, a value of L = N/2 was selected near the midpoint of the range as the optimal value for the LPSVD procedure.

The third setup parameter for LPSVD which affected the performance significantly was the number of datapoints used in the analysis. It was found through simulation that the failure rate was highly dependent on the value chosen for N and, when plotted against N, exhibited a clearly defined minima. Through extensive simulation it was found that this minima was dependent on only two parameters, the minimum decay rate of the lines in the spectrum and the smallest line separation in the signal. No dependence was found on line amplitude, phase, or absolute frequency. As an approximation of the optimal N for a two-line simulation equation 3.1.1 was developed empirically. In an attempt to work around the problem which existed in selecting the optimal N, section 4.5 included an iterative procedure for determining N without a prior knowledge of the results in the totally automated procedure. Unfortunately, the iterative procedure was not perfect which affected the performance of the totally automated algorithm.

As the LPSVD procedure developed generally included noise related lines in the results when using the optimal setup parameters, section 4.4 evaluated three procedures based on subsectioning of the FID which could be implemented to remove them; real/imaginary subsectioning, even/odd subsectioning, and multiple acquisition subsectioning. Real/imaginary subsectioning was found to have a very poor performance relative to the other two as it removed true lines in a high percentage of cases. Even/odd

and multiple acquisition subsectioning had similar performances with respect to failure rate (see figures 4.4.1a through 4.4.1c). Both were able to significantly reduce the number of noise lines in the results especially at low noise levels. They did, however, slightly increase the chances of failure due to missed lines in the final results. Ideally, for the analysis of new data, the multiple acquisition subsets would be generated during the NMR experiment. For the analysis of existing data, even/odd acquisition was found to be the most useful but required a sampling rate of 4x the highest frequency line in the signal to prevent aliasing while multiple acquisition subsectioning only required a sampling rate of 2x.

Although the optimal parameter settings were determined using a two line simulation, the totally automated algorithm was applied in sections 4.6 and 4.7 to simulated six line spectra and actual ^{31}P spectra to gauge its performance. It was found that the algorithm was able to properly analyze the six line spectra and return reasonable results from the actual data.

Possible future research would include developing a better procedure for selection of the optimal N from the dataset, a more robust analysis of the effect of three or more lines on the optimal values of N, the SVD cutoff or regularization parameter, and the model order. As well, a more extensive evaluation of the strengths and weaknesses of the algorithm when applied to actual data is necessary.

Appendix A The Cramer-Rao Lower Bound

The Cramer-Rao (CR) bound specifies the lowest bound on the variance of unbiased parameter estimates. In this thesis the CR bound is used in comparison with the variance of estimated parameters determined from the analysis algorithms and as an estimate of the magnitude of a parameter's error in a test of equivalence. For a more complete discussion of CR bounds the reader is referred to [24].

The CR bounds used in this thesis were calculated from the equations developed using the following method:

For the sampled sequence

$$x_n = \sum_i A_i e^{(-\alpha_i + j\omega_i)n + j\phi_i}, 0 \le n \le N-1, 1 \le i \le k, \qquad [A.1]$$

let ρ be the parameter vector $[A_1, \alpha_1, \omega_1, \phi_1, \ldots\ldots A_k, \alpha_k, \omega_k, \phi_k]$.

For the case of a sum of exponentially damped sinusoids as given in equation [A.1], the unbiased CR bounds are the diagonal elements of the inverse of the Fisher information matrix $\Im$ calculated from

$$\Im_{iq} = \frac{1}{\sigma^2}\sum_{n=0}^{N-1}\left[\frac{\partial \mathrm{Re}(x_n)}{\partial \rho_i}\frac{\partial \mathrm{Re}(x_n)}{\partial \rho_q} + \frac{\partial \mathrm{Im}(x_n)}{\partial \rho_i}\frac{\partial \mathrm{Im}(x_n)}{\partial \rho_q}\right], 1 \le i \le k, 1 \le q \le k. \quad [A.2]$$

The first order partial derivatives of Equation [A.1] are:

$$\frac{\partial x_n}{\partial A_i} = e^{-\alpha_i n + j(\omega_i n + \phi_i)}, \qquad [A.3]$$

$$\frac{\partial x_n}{\partial \phi_i} = jA_i e^{-\alpha_i n + j(\omega_i n + \phi_i)}, \qquad [A.4]$$

$$\frac{\partial x_n}{\partial \alpha_i} = -A_i n e^{-\alpha_i n + j(\omega_i n + \phi_i)}, \qquad [A.5]$$

$$\frac{\partial x_n}{\partial \omega_i} = jne^{-\alpha_i n + j(\omega_i n + \phi_i)}, \qquad [A.6]$$

and the corresponding minimum variances of each parameter are extracted from the inverse of the Fisher information matrix.

Thus,

$$\mathrm{var}(A_i) = \left[\Im^{-1}\right]_{(4i-3)(4i-3)}, \qquad [A.7]$$

$$\mathrm{var}(\phi_i) = \left[\Im^{-1}\right]_{(4i-2)(4i-2)}, \qquad [A.8]$$

$$\mathrm{var}(\alpha_i) = \left[\Im^{-1}\right]_{(4i-1)(4i-1)}, \qquad [A.9]$$

$$\mathrm{var}(\omega_i) = \left[\Im^{-1}\right]_{(4i)(4i)}. \qquad [A.10]$$

References

1. S. Parthasarathy and D.W. Tufts, "Maximum-Likelihood Estimation of Parameters of Exponentially Damped Sinusoids", *Proceedings of the IEEE* **73**, 1528-1530, 1985.

2. M. Joliot, B.M. Mazoyer, and R.H. Huesman, "*In Vivo* NMR Spectral Parameter Estimation: A Comparison between Time and Frequency Domain Methods", *Magn. Reson. Med.* **18**, 358-370, 1991.

3. E.K.-Y. Ho, R.E. Snyder, and P.S. Allen, "Accuracy and Precision of *In Vivo* Magnetic-Resonance Parameters", *J. Magn. Res.* **99**, 590-595, 1992.

4. C. Decanniere, P. van Hecke, F. Vanstapel, H. Chen, S. van Huffel, C. van der Voort, B. van Tongeren, and D. van Ormondt, "Evaluation of Signal Processing Methods for the Quantification of Strongly Overlapping Peaks in ^{31}P NMR Spectra, *J. Magn. Res.* **B 105**, 31-37, 1994.

5. D.W. Tufts and R. Kumaresan, "Singular Value Decomposition and Improved Frequency Estimation Using Linear Prediction", *IEEE Trans. ASSP* **30**, 671-675, 1982.

6. R. Kumaresan and D.W. Tufts, "Estimating the Parameters of Exponentially Damped Sinusoids and Pole-Zero Modeling in Noise", *IEEE Trans. ASSP* **30**, 833-840, 1982.

7. H. Barkhuijsen, R. de Beer, W.M.M.J. Bovée, and D. van Ormondt, "Retrieval of Frequencies, Amplitudes, Damping Factors, and Phases from Time-Domain Signals Using a Linear Least-Squares Procedure", *J. Magn. Res.* **61**, 465-481, 1985.

8. R. de Beer, D. van Ormondt, and W.W.F. Pijnappel, "SVD-Based Quantification of Magnetic Resonance Signals", *J. Magn. Res.* **97**, 122-134, 1992.

9. R. de Beer and D. van Ormondt, "Analysis of NMR Data Using Time Domain Fitting Procedures", *NMR Basic Principles and Progress* **26**, 201-248, 1992.

10. W. Kölbel and H. Schäfer, "Improvement and Automation of the LPSVD Algorithm by Continuous Regularization of the Singular Values", *J. Magn. Res.* **100**, 598-603, 1992.

11. A.-J. van der Veen, E.F. Deprettere, and A.L. Swindlehurst, "Subspace-Based Signal Analysis Using Singular Value Decomposition", *Proceedings of the IEEE* **81**, 1277-1308, 1993.

12. E.K.-Y. Ho, "Parameter Estimation in NMR Using LPSVD", *MSc. Thesis, Department of Applied Sciences in Medicine, University of Alberta*, 1991.

13. N. Ishii, A. Iwata, and N. Suzumura, "Evaluation of an Autoregressive Process by Information Measure", *Int. J. Systems Sci.* **9**, 743-751, 1978.

14. M. Astridge and R.E. Snyder, "Rejection of Noise Related Peaks in *In-Vivo* Magnetic Resonance Spectroscopy", *Proceedings of the SMR* **2**, 1189, 1994.

15. A. Diop, W. Kölbel, D. Michel, A. Briguet, and D. Graveron-Demilly, "Full Automation of Quantitation of *In-Vivo* NMR by LPSVD(CR) and EPLPSVD". *J. Magn. Res.* **B 103**, 217-221, 1994.

16. A. Diop, A. Briguet, and D. Graveron-Demilly, "Automatic *In-Vivo* NMR Data Processing Based on an Enhancement Procedure and Linear Prediction Method", *Magn. Reson. Med.* **27**, 318-328, 1992.

17. A. Diop, Y. Zaim-Wadghiri, A. Briguet, and D. Graveron-Demilly, "Improvements of Quantitation by Using the Cadzow Enhancement Procedure Prior to Any Linear-Prediction Methods", *J. Magn. Res.* **B 105**, 17-24, 1994.

18. Yung-Ya Lin, Nien-Hui Ge, and Lian-Pin Hwang, "Multiexponential Analysis of Relaxation Decays Based on Linear Prediction and Singular-Value Decomposition", *J. Magn. Res.* **A 105**, 65-71, 1993.

19. P.S. Allen and C. Hanstock, ASM 575 Course Notes, *Dept. of Applied Sciences in Medicine, University of Alberta*, 1994.

20. Y. Zaim-Wadghiri, A. Diop, D. Graveron-Demilly, and A. Briguet, "Improving data acquisition parameters of ^{31}P *in-vivo* spectra for signal analysis in the time domain", *Biochimie* **74**, 769-776, 1992.

21. W. H. Press, B. P. Flannery, S. A. Teukolsky, and W. T. Vetterling, *Numerical Recipes: The Art of Scientific Computing*, Cambridge University Press, 1989.

22. S.K. Mitra and J.F. Kaiser, *Handbook for Digital Signal Processing*, John Wiley and Sons, 1993.

23. R.A. DeCarlo, *Linear Systems*, Prentice-Hall, 1989.

24. R. Fante, *Signal Analysis and Estimation: An Introduction*, John Wiley and Sons, 1988.

25. A.V. Oppenheim and R.W. Schafer, *Discrete-Time Signal Processing*, Prentice Hall, 1989.

26. E.O. Brigham, *The Fast Fourier Transform and its Applications*, Prentice Hall, 1988.